Technical University of Denmark

DTU

Streamline Simulation with Capillary Effects Applied to Petroleum Engineering Problems

Berenblyum, Roman; Stenby, Erling Halfdan; Michelsen, Michael Locht; Shapiro, Alexander

[Link back to DTU Orbit](#)

DTU Library
Technical Information Center of Denmark

Streamline Simulation with Capillary Effects Applied to Petroleum Engineering Problems

Roman A. Berenblyum

2004

Ph.D. Thesis

DTU

Streamline Simulation with Capillary Effects Applied to Petroleum

Engineering Problems

by

Roman A. Berenblyum

August 2004

IVC-SEP

Department of Chemical Engineering

Technical University of Denmark

Building 229, DK-2800 Lyngby,

Denmark

Preface

This thesis is submitted as partial fulfillment of the requirements for obtaining the Ph.D. degree at the Technical University of Denmark. The work was carried out at IVC-SEP, Department of Chemical Engineering, from August 2001 to August 2004 under the supervision of Professor Erling H. Stenby, Associate Professor Michael L. Michelsen and Associate Professor Alexander A. Shapiro. The project was sponsored by the Danish Energy Authority, Maersk Oil and Gas, ChevronTexaco and Eni-Agip.

I would like to express my gratitude to Professor Erling H. Stenby, for providing me an opportunity to do my Ph.D. study in the wonderful environment of the IVC-SEP. I would also like to acknowledge Associate Professor Alexander A. Shapiro and Reader Michael Michelsen for the knowledge they have shared.

I feel very grateful to Professor Franklin M. Orr, Jr. for splendid 6 months in SUPRI-C group, Department of Petroleum Engineering, Stanford University. This time has been very important for many aspects of my life. It has been a pleasure to work with Acting Assistant Professor Kristian Jessen, Yildiray Cinar, Bradly Malisson and Assistant Professor Margo Gerintsen during my stay in Stanford. I am happy and honored that our collaboration continued since then.

I would like to appreciate my friends and collegues in Denmark and USA: Oleg Medvedev, Thomas Lindvig, Petr Zhelezny, Mohammad Karimi-Fard and many, many more. Moreover I am grateful to my friends in Moscow, for supporting me, keeping in touch, and being spiritually close no matter how many thousands kilometers lied between us.

And finally, I would like to appreciate my parents – for bringing me into this world, taking care for me, loving me and supporting me in all my enterprises.

Lyngby, Denmark. 2003

Roman Berenblyum

Summary

This thesis represents a three year research project, resulting in the development of the full-scale three dimensional two-phase immiscible incompressible streamline simulator accounting for capillary effects.

Streamline simulation is a relatively new technique, with a potential to become one of the key tools in reservoir simulation. The first streamline simulator appeared around 10 years ago. The advantages of the streamline methods are their exceptional simulation speed and less dispersed numerical solutions [7, 17, 19, 67]. Tracing the streamlines with respect to Darcy flow velocity [31] makes it possible to account for the non-linearities associated with fluid mobilities and the capillary pressure. The streamlines allow to decouple complex 3D saturation equation into set of simple 1D solutions by means of the time-of-flight (TOF) concept [17, 32]. However, up to the current moment, they provide limited abilities, compared to industrial standard finite-difference simulators. The main drawback of the two-phase immiscible incompressible streamline simulator is lack of capillary effects. In heterogeneous reservoirs with alternated wettability these forces may be extremely important, and, in some cases, dominating. The developments of the streamline methods are presented in Chapter 1.

This thesis presents a methodology to introduce capillary effects into streamline simulation. The first chapter gives an introduction into the fluid flow in the porous media and into capillary effects. The second chapter presents mathematical formulation of the governing equations with capillary effects. Both the pressure and the saturation equations are modified to include capillary effects. Introduction of capillary effects into the pressure equation is necessary to correctly predict the phase pressures. The pressure values are used to compute the Darcy flow velocity. As a result the streamlines are traced with respect to viscous, gravity and capillary forces. The modification of the saturation equation is necessary to correctly predict the capillary cross-flow

effects. Various aspects of the numerical solution of the governing equations are discussed. A Capillary-Viscous Potential (CVP) [14] is introduced as a modification to the pressure equation with capillary effects for a better handling of the heterogeneities of the porous media. The CVP method is shown to provide more stable solution, compared to the straightforward method (SFD) of accounting for capillary effects in the pressure equation. The saturation equation is solved using the operator splitting method. The viscous forces are accounted along the streamlines; afterwards the fluids are redistributed on the finite-difference grid with respect to the capillary and gravity forces.

The third chapter presents simulation results of a number of test cases and the discussion of the modifications. First, the CVP and the SFD methods of introduction of capillary effects into the pressure equation are compared. Afterwards the saturation equation modifications are discussed. The time step selection methods are evaluated. Finally the streamline simulator is applied to the reservoir-scale simulations.

The fourth chapter starts with illustrations of capillary effects in the heterogeneous and the alternated wet media. The investigation of the zone of application of the streamline simulator with capillary effects is presented. The CapSL is compared to the commercial finite-difference simulator Eclipse based on the laboratory experiments.

The last part of my thesis presents conclusions and briefly addresses possible research topics for the future.

Summary in Danish – Resumé på dansk.

Denne afhandling repræsenterer et 3-årigt forskningsforløb, som har resulteret i udviklingen af en fuld-skala 3-dimensionel, 2-fase blandbar, og inkompressibel strømlinje-simulator, der tager højde for de kapillære effekter.

En strømlinje-simulator er en relativ ny teknik, som om muligt kan spille en nøglerolle i reservoir-simuleringer. Den første strømlinje-simulator fremkom for cirka 10 år siden. Fordelene ved strømlinje-metoderne er deres utrolige simuleringshastighed og formindskede numeriske dispertion [7, 17, 19, 67]. Sporing af strømlinjerne med hensyn til Darcy-strømningshastigheder [31] gør det muligt at redegøre for de ikke-lineariteter, som er forbundet med fluid mobiliteter og kapillartrykket. Strømlinjene tillader en afkobling af den komplekse 3D mætningsligning til et sæt af enkle 1D løsninger vha. time-of-flight (TOF) konceptet [17, 32]. Men hidtil har strømlinje-simulatorerne kun haft en begrænset anvendelse, sammenlignet med den industrielle standard, finite-difference-simulatorer. Den største ulempe ved en 2-fase blandbar, inkompressibel strømlinje-simulator er dens manglende kapillar-effekt. I heterogene reservoirer med skiftende fugtpræference er disse krafter meget vigtige, og i visse tilfælde altafgørende. Udviklingen af strømlinje-metoder er præsenteret i Kapitel 1.

Denne afhandling præsenterer en metodik til at introducere kapillære effekter i strømlinje-simulatorer. Det første kapitel giver en introduktion til fluid strømning i porøse strukturer og til kapillære effekter. Det andet kapitel præsenterer den matematiske formulering af de bestemmende ligninger med kapillære effekter. Både tryk- og mætningsligningen er modificeret således, at de redegør for de kapillære effekter. Introduktionen af de kapillære effekter i trykligningen er nødvendig, når trykkene i de enkelte faser skal forudsiges korrekt. Trykkene bruges til at beregne Darcy-strømningshastigheden. Derfor spores strømlinjerne med hensyn til viskøse og kapillære krafter samt tyngdekraften. Modifikationen af mætningsligningen er nødvendig for at kunne forudsige de kapillære kryds-strømningseffekter korrekt. Et Capillary-Viscous-Potential (CVP) [14]

introduceres som en modifikation af trykligningen med kapillære effekter for at opnå en bedre håndtering af heterogeniteter i en porøs struktur. Det er vist, at CVP-metoden har en mere stabil løsning, sammenlignet med den ligefremme metode (SFD), når det gælder beskrivelsen af de kapillære effekter i trykligningen. Mætningsligningen er løst ved brug af operator-delingsmetoden. Der er redegjort for de viskøse krafter langs strømlinjerne; derefter er fluiderne på ny fordelt i finite-difference-gitteret med hensyn til de kapillære krafter og tyngdekraften.

Det tredje kapitel præsenterer simuleringsresultaterne fra et antal prøver og en diskussion af modifikationerne. Først sammenlignes CVP- og SFD-metodernes introduktion af de kapillære effekter i trykligningen. Derefter diskuteres modifika-tionerne i mætningsligningen. Metoder til bestemmelse af tidsskridt evalueres. Endelig er strømlinje-simulatoren anvendt til simuleringer på reservoir-skala.

Det fjerde kapitel begynder med illustrationer af de kapillære effekter i heterogene og skiftende vædende strukturer. En undersøgelse af an-vendelsesområde for strømlinje-simulatorer med kapillære effekter er præsen-teret. CapSL er sammenlignet med den kommercielle finite-difference- simulator Eclipse på baggrund af laboratorie-eksperimenter.

Den sidste del af min afhandling præsenterer konklusioner og berører kort nogle mulige fremtidige forskningsområder.

Contents

List of Tables

List of Figures

Chapter 1. Introduction

The main goal of any reservoir simulation project is to predict the performance of the displacement process. Streamline simulators offer less dispersed and faster solutions of displacement problems, compared to finite difference methods. However, currently available commercial streamline simulators lack the description of capillary effects.

This chapter offers a review of the basic concepts of the fluid flow in porous media. The Darcy velocity and the mass conservation law are discussed. The implicit pressure explicit saturation (IMPES) solution method, used in streamline simulators is introduced.

The physical concepts of capillary effects are presented. Importance of capillary forces for the reservoir simulation is discussed. Possible difficulties of the introduction of capillary effects into the streamline simulator are mentioned.

The chapter concludes with an overview of the streamline methodology. The history of the development of the streamline / streamtube methods is traced from the principal introduction of the streamfunction [54] to the development of the 3DSL0.25 streamline simulator [8]. The 3DSL 0.25 streamline simulator is kindly provided by SUPRI-C group, Department of Petroleum Engineering, Stanford University as the base code for the introduction of capillary effects. Some latest advances in the streamline development, including a three-phase compositional simulator, a double porosity streamline simulator, an application of the streamline simulator to the history matching and the field optimization tasks as well as prior attempts of accounting for capillary forces are introduced.

1.1. Fluid flow in porous media

Any reservoir rock is a porous medium. The *porous medium* is any material containing pores. Both a sponge and a chalk are porous media. The ideal porous medium may be most clearly comprehended by visualizing a body of ordinary unconsolidated sand. Such a porous medium contain innumerable voids of varying sizes and shapes comprising "pore spaces" and interstices between the individual solid particles of the sand, comprising "pore throats" [54].

Significant properties of a porous medium are *porosity*, which is a measure of the pore space and hence of the fluid capacity of the porous medium and *permeability*, which is a measure of the conductivity of the porous medium under the influence of a driving force [34, 54].

Fluid flow in porous media is described by the mass and the momentum conservation laws [5]. The momentum conservation law is represented by the *Darcy law*.

The history of the Darcy law starts at 1856, when Darcy [31] was working with the flow characteristics of the sand filters. Darcy performed an experimental study of the problem and founded the quantitative theory, which finally became known as the *Darcy law*:

$$Q = \frac{cA\Delta h}{L}.$$
(1.1)

Here Q is the flow rate, A is the cross-sectional area of the media, Δh is the difference between fluid heads at the inlet and the outlet faces of the media in the meters to water and L is the length of the media, see Figure 1-1. The coefficient c characterises the velocity of the flow through the unit of area, under the unit gradient of the flow head and is called the filtration coefficient.
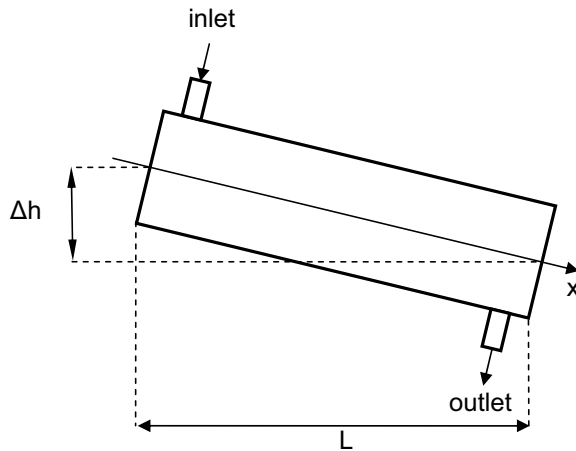
Figure 1-1. Scheme of Darcy experimental setup.

The Darcy law may be derived with several assumptions from the Navier-Stokes equation [6, 66]. For the petroleum engineering problems the Darcy's law is written as [9, 34, 54]:

$$\underline{u} = -k\frac{k_r}{\mu}\underline{\nabla}(P + \rho g D),$$ (1.2)

where u is the velocity of the flow, k is the permeability of the rock, k_r is the relative phase permeability, μ is the viscosity of the fluid, P is pressure, ρ is the density of the fluid, g is the gravity acceleration and D is the relative height to some reference point.

For a two-phase flow the Darcy velocity, equation (1.2), is applied to each phase:

$$\underline{u}_j = -k\lambda_j\left(\underline{\nabla}P_j + \rho_j g\underline{\nabla}D\right).$$ (1.3)

Here index j represents water or oil phases. The phase mobility λ_j is introduced as the ratio of the relative phase permeability to the phase viscosity:

$$\lambda_j = \frac{k_{rj}}{\mu_j},\ j = o,w \text{ for oil and water respectively}.$$ (1.4)

The total velocity is introduced as a sum of the velocities of water and oil phases:

$$\underline{u}_t = -k\lambda_w \left(\nabla P_w + \rho_w g \nabla D\right) - k\lambda_o \left(\nabla P_o + \rho_o g \nabla D\right).$$ (1.5)

Neglecting the capillary pressure, $P = P_w = P_o$:

$$\underline{u}_t = -k\left(\lambda_t \nabla P + \lambda_g \nabla D\right),$$ (1.6)

here

$$\lambda_t = \lambda_w + \lambda_o$$ (1.7)

is the total mobility, and

$$\lambda_g = \left(\lambda_w \rho_w + \lambda_o \rho_o\right)g$$ (1.8)

is the total gravity mobility.

For the incompressible fluids, flowing through the incompressible reservoir rock the gradient of the total velocity at any point in the reservoir away from sinks or sources must be equal to zero:

$$\nabla \cdot \underline{u}_t = 0.$$ (1.9)

Introducing the total velocity, equation (1.6):

$$\nabla \cdot \left[k\left(\lambda_t \nabla P + \lambda_g \nabla D\right)\right] = 0.$$ (1.10)

However, in the vicinity of the wells, equation (1.10) should be written as:

$$\nabla \cdot \left[k\left(\lambda_t \nabla \cdot P + \lambda_g \nabla D\right)\right] = q_s,$$ (1.11)

here q_s represents the well volumetric flow rate.

The mass conservation equation is represented by the so-called saturation equation. Phase saturation is the fraction of the pore volume taken by the given phase. For a two phase flow it is sufficient to resolve the mass conservation law for any of the two phases, since:

$$s_w + s_o = 1.$$ (1.12)

Here s is saturation, subscript o defines oil phase and subscript w defines water phase.

For the immiscible incompressible black oil simulation the mass conservation equation is typically solved for the water phase [9, 17, 68, 70]:

$$\phi \frac{\partial s_w}{\partial t} + \underline{\nabla} \cdot \underline{u}_w = 0 \ . \tag{1.13}$$

Here ϕ is porosity, s_w is the water saturation, t is time, u_w is the velocity of the water phase.

All methods of reservoir simulation are based on solving a system of equations, comprised of so-called pressure (1.11) and saturation (1.13) equations:

$$\begin{cases} \underline{\nabla} \cdot \left[k \left(\lambda_t \underline{\nabla} P + \lambda_g \underline{\nabla} D \right) \right] = q_s \\ \phi \dfrac{\partial s_w}{\partial t} + \underline{\nabla} \cdot \underline{u}_w = 0 \end{cases} \tag{1.14}$$

The system of equations (1.14) may be solved in the discretised form on a finite-difference (FD) grid, using various solution methods. One of the solution methods is the *Fully Implicit* [17, 52] method. Using the fully implicit procedure the governing system of equations (1.14) is simultaneously solved for all the unknowns in all the gridblocks. It can be shown that this solution consists entirely of pressures and functions evaluated at the new time step and therefore is stable for any given time step size. However, the time step of the numerical solver may be restricted in case of strongly non-linear fractional flow function [52, 55]. The fully implicit formulations generally have a tendency toward high numerical dispersion effects [25]. Another solution method is the *IMPES* (Implicit Pressure Explicit Saturation) method [5, 26]. In this method the solution procedure is divided into two steps. First the pressure is implicitly solved in space and the flow velocity is found; afterwards the saturation values are updated explicitly. During the implicit pressure solution the phase mobilities are treated explicitly. As a result the time step size of the IMPES method is restricted to handle the non-linearities of phase mobilities [5, 27, 28, 52, 76]. The time step size must be restricted so that the displacement front propagates not more than one grid block per single time step. The IMPES solutions may become extremely slow when applied to complex three-dimensional

displacement problems. However, the IMPES methods are less affected by the numerical dispersion compared to the Fully Implicit methods. An *Advanced Implicit (AIM)* method [36, 52, 61-63, 73, 74, 79] is introduced to combine the strong points of both the fully implicit and the IMPES methods. The AIM method uses an implicit solution procedure for the grid blocks in the "difficult" region, typically, around the displacement front and an IMPES solution procedure for the rest of the reservoir.

The streamline simulators are based on the IMPES solution procedure. The outline of the IMPES solution procedure is presented below:

1. A reservoir is divided into a number of grid blocks in x, y and z directions. Each grid block is assigned the porosity, the permeability and the initial water saturation values;

2. The equation (1.11) is solved implicitly for the pressure values in all grid blocks.

3. The water velocity is subsequently calculated in all grid blocks, using the Darcy velocity equation (1.6);

4. The equation (1.13) is solved for the water saturation in all grid blocks;

5. The solution procedure returns to step 2 for the next time step.

1.2. Physics of capillary effects

For the flow of two or more immiscible fluids in porous media it is necessary to consider the effect of the forces acting on the fluid contact interface.

A water molecule surrounded by other water molecules has a zero net attractive force. On another hand, a water molecule on the interface of the fluid contact has two different forces acting on it – one from the underlying water molecules,

another from the oil molecules lying directly above the interface. The resulting force is unbalanced, creating the interfacial tension. For the problems of the fluid flow in porous media it is important to consider not only the interface between two fluids, but the interface between the fluids and a solid surface [4, 34]. The equilibrium of the forces acting on a bubble of a fluid on a surface immersed into another fluid is presented below:
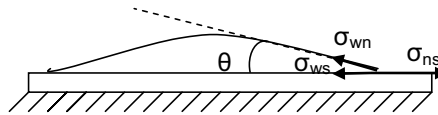
Figure 1-2. Drop of wetting fluid on the surface immersed into another fluid.

In Figure 1-2 σ is the *interfacial tension*; index *s* defines solid; index *w* defines wetting phase; index *n* defines non-wetting phase; θ is the *contact (wetting) angle*. By convention the contact angle is measured through the denser liquid phase. The cosine of the contact angle may be found as [4, 34, 75]:

$$\cos\theta = \frac{\sigma_{ws} - \sigma_{ns}}{\sigma_{wn}},$$ (1.15)

The above equation is a rough approximation and does not take into account many factors as, for example, roughness of the surface [1]. Moreover it may give values of the cosine of the wetting angle higher than unity, which corresponds to the formation of the wetting phase film on the surface.

The term *wetting* is used for the phase which tends to have a bigger contact with the surface. Wettability is related to the system of two fluids and the surface, see Figure 1-3.
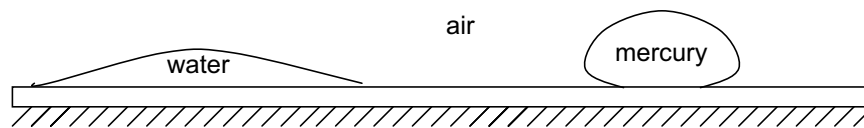
Figure 1-3. Drops of different fluids on the surface.

For example, in case of water / air system in contact with a wooden table the water is the wetting phase. For the mercury / air system and the same table the

air is the wetting phase. This explains the difference in the outlook of the liquid drops on the same surface.

The wettability alters the direction of the fluid flow under the capillary pressure gradient, as shown in Figure 1-4.
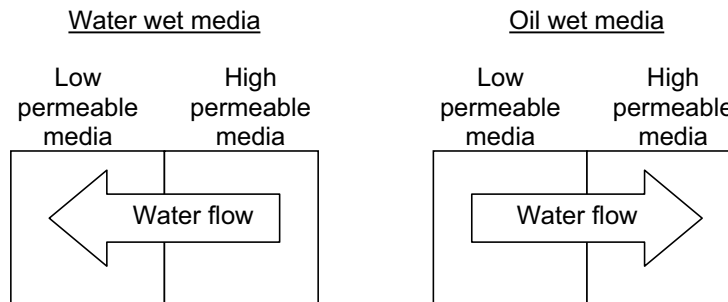
Figure 1-4. Direction of the fluid flow under capillary pressure gradient in differently wet media.

Further in the text the capillary effects are explained on the example of the water wet media.

The *capillary pressure* may be derived from observing two different phases in a beaker with capillary immersed in it [4]. The characteristic capillary pressure is introduced as:

$$P_c = P_o - P_w = \frac{2\sigma \cos\theta}{r}.$$

(1.16)

Here r is the radius of the capillary.

An important observation is that the pressure of the wetting phase is lower than the pressure of the non-wetting phase. This experimental observation is nearly always implicitly assumed in the literature sources. The general proof has not been presented and poses a very complicated task [75].

Furthermore, the model of parallel capillary bundles [34] is often used to represent the structure of the porous media. This model is based on the simplification of porous media to the set of the tortuous cylindrical capillary with the constant radii of each capillary. Permeability of the ideal cylinder is evaluated as:

$$k = n\frac{\pi r^4}{8},$$ (1.17)

porosity as:

$$\phi = n\pi r^2.$$ (1.18)

Here n is the concentration of the capillaries per unit of the area.

Dividing equation (1.17) by equation (1.18) the radius of a pore can be obtained in terms of porosity and permeability:

$$r = 2\sqrt{2\frac{k}{\phi}}$$ (1.19)

Equation (1.19) is derived using the Carman-Kozeny model. In reality the shapes of the capillaries diverse from the ideal cylinders. Using equations (1.16) and (1.19) a characteristic value of the capillary pressure, within an order of magnitude, may be obtained:

$$P_c \sim \frac{\sigma\cos\theta}{\sqrt{k/\phi}}.$$ (1.20)

Leverett [47] proposed a modification to the capillary pressure equation to convert all capillary-pressure data to a single universal curve. So-called Leverett or J-function is introduced as a function of the saturation of any of the two phases. Capillary pressure equation is obtained as:

$$P_c = \frac{\sigma\cos\theta}{\sqrt{k/\phi}}J(s_w).$$ (1.21)

In fact there is a significant difference in the correlation of the J-function to the saturation from formation to formation, so that no universal curve is found.

Figure 1-5 sketches the displacement processes typical for an oil reservoir. Initially the reservoir is fully saturated with water. During oil migration water is displaced by oil in the process called the *primary drainage*. During the oil recovery oil is displaced by the injected water in the process called the

imbibition. If water is to be displaced by oil again, for example in the laboratory experiments, the displacement process is called the *secondary drainage.*
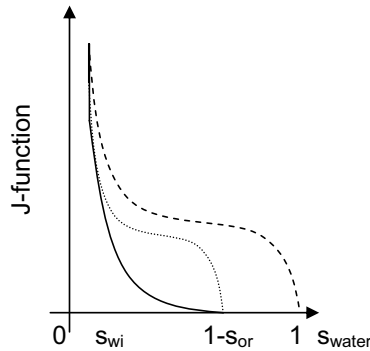
Figure 1-5. Typical shapes of the J-function for primary drainage (dashed line), imbibition (solid line) and secondary drainage (dotted line).

During the imbibition or the secondary drainage the saturation of the displaced fluid decreases to a non-zero value. At this non-zero saturation the displaced fluid becomes immobile. The minimum mobile oil concentration is called *irreducible oil saturation*. The minimum mobile water saturation is called *initial water saturation.* The term initial water saturation is used in relation to the imbibition process. Non-zero initial water and irreducible oil saturations are due to the fact that each phase can be mobile only while it is continuous. Parts of water or oil may be trapped inside another phase and therefore become immobile [11, 34]. The mechanisms of formation of the trapped oil or water ganglia are presented and discussed in [11, 19].

The main capillary pressure effect is the redistribution of the phases inside heterogeneous porous media. The wetting phase prefers to travel through the low permeable porous medium since it provides larger contact area with the surface [34]. Neglecting capillary effects may result in incorrect prediction of the displacement profiles.

The capillary pressure also leads to the end-effects between the zones with different permeability and in the vicinity of a production well. Due to the end-effects the wetting phase is accumulated on the border in the low permeable zone before breaking through into the high permeable medium [9, 34, 54]. The increase of the water saturation in the low permeable boundary layer leads to decrease of the capillary pressure (see Figure1-2) and therefore allows water to penetrate into the high permeable zone. This effect may be observed in the vicinity of a producer, where the capillary effects lead to the well-known fact of drowning the well. The well, being a tube of several inches in diameter can be considered as extremely high permeable medium, see the equation (1.17). Therefore, as soon as water in the reservoir breaks through to the production well, it is accumulated around the well due to the end-effects before penetrating into the well. Laboratory tests [49] have also shown that water may flow in the low permeable (water-wet sample) medium without penetrating into the high permeable one until the low permeable medium is completely swept.

The importance of the capillary forces may be estimated by means of several groups of dimensionless parameters [9, 80]. These dimensionless groups allow estimating a relation of the average viscous to the average capillary forces. However, even when the dimensionless parameters show that the displacement is viscous dominated, the capillary forces may be locally dominating, for example in the vicinity of the displacement front or on the borders of the zones with different permeability.

Capillary effects are rather complicated. One of the difficulties both for the finite-difference and the streamline methods is the capillary limitation of the stable time step size.

The capillary pressure poses an additional problem for the streamline methods. Capillary as well as gravitational forces often act across the streamlines therefore the operator splitting solution is required. The operator splitting solution is described in detail in Section 2.2. Moreover, unlike gravity no uniform direction of the capillary forces can be found. Tracing the "capillary lines" seems

to be a very complicated task therefore the operator splitting step is performed on the finite difference grid.

1.3. Introduction to Streamline Simulation

The introduction starts with an outline of the 3DSL 0.25 streamline simulator (by R.P. Batycky, SUPRI-C, Department of Petroleum Engineering, Stanford).

Later an overview of the streamline methods development history is presented. The overview is divided into three parts: Introduction of streamlines and early stage of the development; Development of the streamline methods; Modern advances in the streamline methods.

The overview mentions only the most relevant works for the current project. Many other researchers and scientists contributed to the development of the streamline methods.

1.3.1 Outline of the 3DSL 0.25

Figure 1-6 outlines the structure of the 3DSL 0.25 streamline simulator. More information on the individual steps of the 3DSL 0.25 scheme may be found further in the text.

Initialize model

Solve pressure equation
$$\underline{\nabla} \cdot \left[k \left(\lambda_t \underline{\nabla} P + \lambda_g \underline{\nabla} D \right) \right] = q_s$$
implicitly on the finite-difference grid

Calculate total Darcy flow velocity in all grid blocks:
$$\underline{u_t} = -k \left(\lambda_t \underline{\nabla} P + \lambda_g \underline{\nabla} D \right)$$

Trace 3D streamlines using Pollocks method, based on the total velocity values

Map saturation values from finite-difference grid onto streamlines

Calculate true time

Solve saturation equation along the streamlines:
$$\frac{\partial s_w}{\partial t} + \frac{\partial f_w}{\partial \tau} = 0$$

Map saturation values from streamlines back to FD-grid

Account for gravitational forces on the FD grid
$$\phi \frac{\partial s_w}{\partial t_2} + \left(\rho_w - \rho_o \right) \underline{g} \cdot \underline{\nabla} G = 0$$

End simulation

Figure 1-6. Outline of the 3DSL 0.25 streamline simulator.

1.3.2. Introduction of streamlines and early stage of development

The term *streamfunction* was first used by Muskat in 1937 [54] in petroleum engineering studies for analysis of the two-dimensional steady state flows from the finite line sources into an infinite sand. Muskat used the analytical function of the complex variable *z=x+iy* to introduce the Darcy velocity and the streamfunction potentials. *Streamlines* were introduced as lines of constant streamfunction, tangent to the fluid velocity vector in any given point. In the static case a streamline illustrates one of the paths, which the particles of the flow may take inside the porous media.

The next key moment in the streamline methodology is represented by three papers by Higgins and Leighton in the early sixties [37-39]. Higgins and Leighton simulated a quarter of a five-spot pattern in a homogenous reservoir, containing one injector and one producer, as sketched in Figure 1-7.
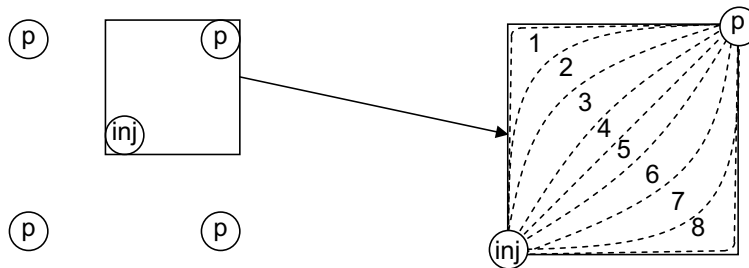
Figure 1-7. Five-spot pattern. A quarter of a five-spot pattern with streamlines.

The simulation space was divided into the flow channels, or streamtubes (indicated with numbers 1 to 8 in Figure 1-7), bounded by nine analytically calculated streamlines (dashed lines in Figure 1-7). The streamtubes remained constant throughout the whole simulation time. To account for the changes of the fluid mobilities, Higgins and Leighton introduced the flow resistance parameter for every channel [37]. The authors presented a method to forecast three-phase flow [38] in complex geometry. The method was implemented to simulate the specific five-spot waterflood of a partially depleted stratified oil

reservoir. The reservoir was divided into set of layers without any cross-flow between them. Field performance was determined as a sum of performances of individual layers. The papers also described Higgins – Leighton method, which did not require calculations of the individual pressures, as the resistance to flow in each channel in the flow pattern was readily determined without using the iterations.

Martin and Wegner [50] reported that the method suggested by Higgins and Leighton failed for water-to-oil mobility ratios smaller than one ($\lambda_w/\lambda_o < 1$). The source of an error was found to be the assumption of the streamlines being independent upon the mobility ratio. Martin et al. suggested to periodically update the streamtubes. Periodic updates of the streamtubes created non-uniform initial conditions and required numerical solution along them. The suggested method dramatically increased the quality of the predictions for the simulations with mobility ratios less than one. The streamlines were updated using numerical or analytical methods involving the pressure and the streamfunction solution.

1.3.3. Development of the streamline method

Pollock [57] presented a semi-analytical flow path tracing method for finite-difference models. This semi-analytical method allowed tracing the streamlines in complex displacement cases. To trace the streamlines from the block inlet face to the block outlet face (see Figure 1-8) the following routine was suggested:

- Evaluate average velocity on a grid block face by dividing the volumetric flow rate through the face by the cross-sectional area of the face and the porosity in the cell;

- Compute the velocity at any point in the grid block by means of the linear interpolation of the grid block face velocities;

- Calculate the time necessary to reach all but the inlet faces of the block using the rate of change of the velocity components in each direction;

- Compute the block outlet coordinates for the face with the minimum reach time, see Figure 1-8.
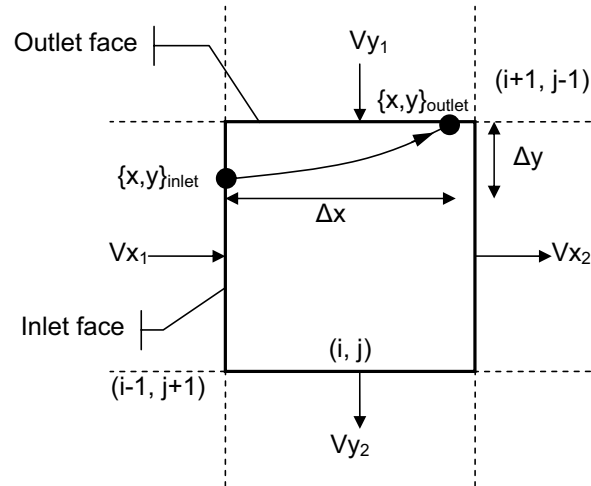
Figure 1-8. Tracing the streamline through the gridblock using Pollock's method.

Renard [59] presented a two-dimensional streamtube simulator. The simulator was developed based on a streamline tracing technique similar to the one suggested by Pollock, however, there was no reference to Pollock's work, discussed above. Precise determination of the fluid distribution was required to remap the fluid properties from the old set of streamtubes onto the new one. This task was performed by introduction of the dividing lines. The dividing lines splitted the reservoir into drainage areas for each pair of injection-production wells.

Thiele [68] used one-dimensional streamtubes to model the multicomponent multiphase displacements in homogeneous 2D cross-sectional domains. The streamtubes used by Thiele were similar to the ones introduced by Higgins and Leighton [37]. The cross-sectional domains were restricted by the no-flow boundary on the top and bottom of the domain and by the constant flow rate or

pressure on either end of a domain. Non-linearity of the underlying flow field was taken into account by periodically updating the streamtubes. The streamtubes were updated based on the values of the streamfunction. Thiele reported that unlike the streamlines, the streamtubes offered the visual interpretation of the local flow velocity - thick sections of a streamtube corresponded to the slow flow regions, thin sections to the fast flow regions.

The streamfunction for a three-dimensional case was presented by Matanga [51]. The streamtubes in three-dimensions were formed by the streamsurfaces, not the streamlines as in two-dimensional case. The interception of two streamsurfaces gave a streamline. However, the 3D streamfunction was shown to be rather complicated.

Tracing streamlines in three dimensions does not pose any additional complications comparing to a two-dimensional case. A possibility to combine the strong points of both methods: ease of streamline tracing and flow velocity information from streamtubes was presented in the work by Datta-Gupta and King [32]. The "time-of-flight" concept was introduced along the streamlines. This concept allowed representing the flow velocity without using the streamtubes. The time of flight represented the travel time of a particle to the certain point along the streamline, see Figure 1-9.
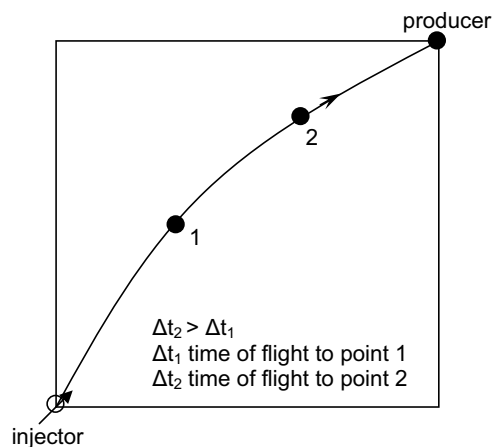
Figure 1-9. Time of flight from the injector along the streamline to the producer.

The time-of-flight in the differential form was introduced as [18, 32]:

$$\frac{\partial \tau}{\partial s} = \frac{\phi}{\left\| \underline{u}_t \right\|} \, .$$

(1.22)

Moreover time of flight allowed to transform the three-dimensional saturation equation (1.13), to the one-dimensional equation in the time of flight coordinates along the streamlines:

$$\frac{\partial s_w}{\partial t} + \frac{\partial f_w}{\partial \tau} = 0 \, ,$$

(1.23)

where

$$f_w = \frac{\lambda_w}{\lambda_w + \lambda_o} \, .$$

(1.24)

It is important to point out, that the streamlines were traced taking into account the effects of porosity, permeability and the pressure gradient. The time of flight variable accounted for the total velocity and the reservoir porosity. This allowed one dimensional equation (1.23) to be independent upon any reservoir properties.

The streamline method was extended to true 3D systems, including longitudinal and transverse diffusion and gravitational effects in FCM displacements by Blunt et al. [18]. The gravitational effects were included in the step of tracing the streamlines by solving the pressure equation with gravitational effects. The saturation equation accounted for the gravitational effects as well:

$$\phi \frac{\partial s_w}{\partial t} + \underline{u}_t \cdot \nabla f_w + \left(\rho_w - \rho_o \right) \underline{g} \cdot \nabla G = 0 \, .$$

(1.25)

Here $G = \dfrac{\lambda_w \lambda_o}{\lambda_w + \lambda_o}$,

(1.26)

and $\underline{g} = g \nabla D$.

(1.27)

The equation was transformed to the form of:

$$\phi \frac{\partial s_w}{\partial t} + \underline{v} \cdot \nabla f_w = 0 \, .$$

(1.28)

Here $\underline{v} = \underline{u}_t + \left(\rho_w - \rho_o \right) \underline{g} \dfrac{\partial G}{\partial f_w}$

(1.29)

The time-of-flight was introduced in terms of v rather than u_t:

$$\frac{\partial \tau}{\partial s} = \frac{\phi}{\|\underline{v}\|} \, . \tag{1.30}$$

As a result the equation (1.23) was obtained, minimizing the necessary modifications of the streamline simulator to account for the gravitational forces.

Thiele et al. [69] presented a three-dimensional two-phase streamline results and extended the method to multi-well simulations with changing mobility fields. Reported modifications were essentially a continuation of the Thiele's PhD work [68]. The 3D displacements were modeled using the streamlines with time of flight concept, rather than the streamtubes.

The simulator was further extended to the compositional version neglecting the gravitational effects [70]. The compressibility of the fluids was accounted only along the streamlines. The pressure was considered incompressible.

Gravity very often acts across the main direction of the flow and, therefore, across the streamlines. Accounting for the gravitational effects only along the streamlines may lead to underestimation of the gravity cross flow. To account for the gravity cross flow, Bratvedt et al. suggested using an operator splitting method [21]. The equation (1.25) was solved in two consecutive steps. First the saturation was solved along the streamlines with respect to the viscous forces only, equation (1.23). The gravitational effect was accounted for in the second step on the finite difference grid:

$$\phi \frac{\partial s_w}{\partial t_2} + \left(\rho_w - \rho_o\right)\underline{g} \cdot \underline{\nabla} G = 0 \, , \tag{1.31}$$

Here index 2 indicates the second step of the operator splitting method.

Another significant difference of the streamline simulator developed by Bratvedt was utilization of the front-tracking method for resolving the saturation equation (1.23). The key principle of the front-tracking method is to represent the saturation front as a step function with a set of discontinuous fronts. The step function converges towards the physical continuous solution with increase of number of fronts. The reported advantages of the front tracking methods were: 1) less smearing of the front; and 2) independence of the numerical solution of a

grid, leading to a method not limited by the CFL (Courant-Freidrichs-Levi [76]) stability condition [20, 21].

Batycky's PhD thesis [8] resulted in the three-dimensional two-phase field-scale streamline simulator (3DSL 0.25). The gravitational effects were accounted for using the operator splitting method. The gravity step was performed by tracing the so-called gravity lines for each vertical column of the grid blocks. Batycky has assigned the volumetric flow rate to each streamline. This allowed treating each streamline as a centerline of an imaginary streamtube. The volume of such a streamtube was found by multiplying the volumetric flow rate along the streamline by the time of flight.

The 3DSL 0.25 also utilized the "True time" concept. This concept required calculating the "true" time step size using the cumulative water balance during the current time step:

$$\Delta t_{true} = \frac{V_{water,initial} - V_{water,in\ place}^{n+1} + \sum_{i=1}^{n} V_{water,injected} - \sum_{i=1}^{n} V_{water,produced}}{Q^{n+1}\left(f_w^{n+1/2} - 1\right)}.$$

(1.32)

Here t is time, V is volume, Q is flow rate, superscript n denotes time step, and $f^{n+1/2} = \left(f^n + f^{n+1}\right)\big/2$ is the average field production fractional flow function.

1.3.4. Recent advances in streamline simulation

The latest advances in streamline simulation were performed in the several directions.

Bedrikovetsky et al. [9] suggested an analytical three-dimensional two-phase streamline simulator using curvilinear coordinates. The paper presented the transformation from the Cartesian to the curvilinear coordinates, resulting in the dispersion free, fast analytical solution neglecting capillary and gravitational effects.

Di Donato et al. [33] recently presented a dual-porosity streamline simulator, based on the 3DSL two-phase black-oil version. The dual-porosity simulation system was composed of a flowing fraction, representing the fracture network and the matrix, representing the relatively stagnant regions. In this model the streamlines capture the movement through the fracture system while the transfer of fluids from the fracture into the matrix was accounted for using a transfer function:

$$\begin{cases} \dfrac{\partial s_{wf}}{\partial t} + \dfrac{\partial f_{wf}}{\partial \tau} = -\dfrac{T}{\phi_f}; \\[2mm] \dfrac{\partial s_{wm}}{\partial t} = \dfrac{T}{\phi_m}. \end{cases} \qquad (1.33)$$

Here index f denotes the properties of the fracture region and index m of the matrix, T stands for the transfer function.

The authors concluded that when the appropriate transfer function and the shape factors are applied, the simulation results were in a good agreement with the commercial finite-difference simulator Eclipse [62, 63]. For the million grid block models the dual porosity streamline simulator was orders of magnitude faster, compared to the finite difference simulators.

Al-Hutheli and Datta-Gupta [3] presented a dual-porosity dual-permeability streamline simulator, accounting for the flow both through the fractures and through the matrix. The transfer between the fracture and the matrix was accounted for using the transfer function. The transfer function was resolved by the operator splitting method on the finite-difference grid. The authors reported a close match with Eclipse simulator and significant speed-ups comparing to Eclipse especially for the simulation on the large grids.

Crane et al. [30, 64] presented a fully compositional streamline simulator accounting for gravitational effects by usage of the gravity lines, but neglecting capillary effects. The method combined the streamline tracing method with 1D finite difference solver from Eclipse 300 [63] used along the streamlines and the gravity lines. This method required two pressure field evaluations. The first time

the pressure field was evaluated on the finite difference grid. The pressure values obtained were used to trace the streamlines. The second time the pressure field was evaluated during the 1D finite-difference solution along the streamlines. The pressure solution, received along the streamlines, was mapped back to the finite difference grid along with the saturation solution. The authors reported a significant speed advantage over Eclipse on the large grids. However introduction of the gravitational effects resulted in the slow down of the streamline simulator and some additional stability problems compared to the streamline method neglecting the gravitational effects.

A lot of effort has been done in the area of the compositional streamline simulation. Seto et al. [65] presented a field scale compositional streamline simulator and Jessen and Orr [43] presented the detailed analysis of the gas cycling and the development of the miscibility in condensate reservoirs. Jessen and Orr concluded that using the one-dimensional analytical solver along the streamlines resulted in fast, dispersion free solutions, comparable to the finite-difference simulations on much finer grids. For the 3D simulations [65] the streamline simulator was two or three orders of magnitude faster than Eclipse 300. The outcome of the dispersion free analytical solution was a lower recovery prediction, because the dispersion associated with finite-difference solutions resulted in optimistic sweep efficiency. Seto et al. [65] also concluded that the introduction of the gravitational and capillary effects as well as streamline updating for the 3D compositional cases are important research areas. The description of the 3D compositional streamline reservoir simulator was given by Jessen and Orr [42]. A detailed description of the analytical 1D multicomponent solution along the streamlines may be found in Jessen et al. [41].

Jessen and Orr [44] have further developed compositional streamline simulation to include the gravitational effects. The method of accounting for the gravity segregation using the pseudo-immiscible gravity step marginally added to the overall CPU requirement. The pseudo-immiscible approach requires a phase flash only before the gravity step. After the phase flash each individual phase

defined a segment within the grid block with fixed composition, molar density and fluid properties. During the gravity steps these segments were redistributed in accordance to the density contrast. The final overall block properties after the gravity step were found using the combination of the segments, see Figure 1-10. The method proposed provides a consistent and efficient solution, allowing excellent agreement of the predictions with the Eclipse. The streamline simulator was shown to be up to 22 times faster than equivalent IMPES finite-difference simulation runs.
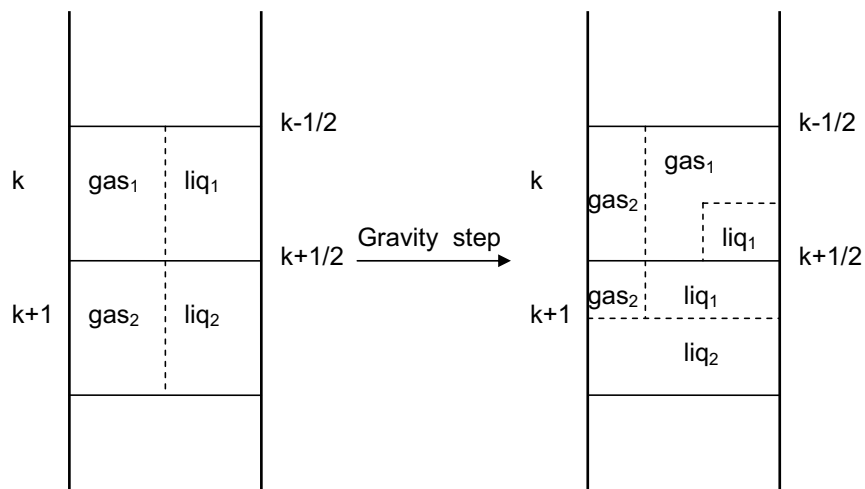
Figure 1-10. Pseudo-immiscible gravity step.

Yan et al. [78] presented a 3D three-phase compositional streamline simulator. The authors compared two different numerical solvers along the streamlines. The gravitational effects were introduced by the operator splitting method using the gravity lines. The developed simulator was applied to water-alternate-gas processes. The authors reported a good agreement with the Eclipse 300. The exceptional speed of the streamline simulator was confirmed as well. As expected the speed-up factors of the streamline simulator increased with increase of the simulation grid size.

The 3DSL streamline simulator has been successfully applied to several history matching and flow optimization problems. Emanuel and Milliken [35] presented

a method to match the individual well performance with assistance of the streamline method. The streamlines helped to visualize the blocks, which were affecting the well performance. This new method was named AHM (Assisted History Matching). The same method was further applied to $10^5 - 10^6$ grid block simulations [53]. Authors concluded a successive history match with very modest changes of the parameters in the model. The changes in the model data were generally within uncertainty of the initial data.

Agarwal and Blunt [2] presented history matching results based on the 3DSL code. The 3DSL was modified to handle the three phases flow as well as compressibility and gravitational effects. Four modification were made: 1) compressibility was introduced into the pressure equation; 2) the possibility of tracing the streamlines which do not start in the injector and / or do not end up in the producer due to the compressibility effects was introduced; 3) compositions were mapped from the grid to streamlines and back, rather than saturations; 4) a mass conservation equation was solved along each streamline accounting for changes in pressure and the total velocity, similar to Craine et al.[30] and Thiele et al. [70]. The history matching was based on changing the permeability field. The relation of the permeability change to the change in time of flight was used to compute the next permeability field. A reasonable history match and predictions has been achieved.

The recent publication by Thiele and Batycky [72] showed an application of the 3DSL to the water injection optimization. The reported advantages of the streamline method for this task were the simulation speed and the fact that the streamlines readily provided a snapshot of how the reservoir was connected. The efficiency of each injector was determined as a ratio of the water injected into it to the oil produced from the offset wells. The water was than redistributed from the low efficiency wells into the high efficiency wells, allowing the higher total field oil production for the same total amount of water injected.

Several attempts to introduce the capillary forces have been performed as well. Berre et al. [16] presented a two-dimensional two- and three-phase front-

tracking streamline simulator with capillary effects. However, the capillary effects are accounted by specifying the simplified capillary pressure / diffusion term rather than capillary pressures between phases.

Rodriguez et al. [60] presented a three-dimensional streamline simulator with capillary effects, neglecting the gravity. The simulator was based on the streamline ideas presented by Batycky in his PhD thesis [8]. The developed simulator was applied only to a simple synthetic simulation case.

The capillary effects did not received proper attention in the streamline development. Therefore it is very important to provide a way to account for capillary effects in streamline simulation.

Detailed overviews of the streamline simulation are also given by King and Datta-Gupta [46], Batycky [8] and Thiele [71].

Chapter 2. Mathematical models

This chapter presents the modifications to the governing IMPES equations to account for capillary effects. The modifications of the governing pressure equation are presented first, followed by the saturation equation modification.

The modified streamline simulation scheme is presented. The numerical solution of the modified systems of equations is given. The possibilities for the material balance errors are discussed. Automatic time step selection algorithms are presented.

The chapter concludes with a simple simulation case illustrating the effects of the modification of the governing system of equation.

2.1. Modification of the governing system of equations

The governing system of equations is introduced in the Section 1.1, equation (1.14). The necessary modifications to the governing system of equations to account for capillary effects are presented below.

2.1.1. Pressure equation with capillary effects

The pressure equation is a momentum conservation law. Derivation of the pressure equation with respect to capillary effects is presented below. As it is stated in Section 1.1, the divergence of the total velocity for the incompressible case must remain zero at any point in a reservoir far from the wells, equation (1.9). The total velocity with respect to capillary pressure is described by the equation (1.5). Using the capillary pressure equation (1.21), the oil pressure is

substituted by the capillary pressure and the water pressure. Regrouping the phase mobilities:

$$\underline{u}_t = -k\left(\lambda_t \underline{\nabla} P_w + \lambda_o \underline{\nabla} P_c + \lambda_g \underline{\nabla} D\right). \tag{2.1}$$

The divergence of the total velocity is than obtained as:

$$\underline{\nabla} \cdot \left[k\left(\lambda_t \underline{\nabla} P_w + \lambda_o \underline{\nabla} P_c + \lambda_g \underline{\nabla} D\right)\right] = 0. \tag{2.2}$$

Here k is permeability; λ represent the mobilities, as introduced in Chapter 1; P_c is the capillary pressure, D is the depth.

2.1.2. Capillary-viscous potential

It is possible to reformulate the pressure equation (2.2) to improve the stability of the numerical solution method and the handling of the sharp variation of the reservoir properties.

Basing on the capillary pressure equation (1.21), the new variable is introduced:

$$\Phi = \frac{\sigma \cos \theta}{\sqrt{k/\phi}}. \tag{2.3}$$

This new variable Φ is dependent only upon the properties of the porous media and independent of the saturation. Therefore the capillary pressure may be represented by the product of Φ and the saturation dependent Leverett function $J(s)$. The gradient of the capillary pressure is then obtained as:

$$\underline{\nabla} P_c = J(s)\underline{\nabla}\Phi + \Phi \underline{\nabla} J(s). \tag{2.4}$$

The gradient $\underline{\nabla}\Phi$ depends only upon the reservoir properties. The gradient is responsible for the transfer of the fluids between the zones with different permeability and / or wettability. The gradient of the Leverett function $\underline{\nabla} J$ acts mostly in vicinity of the saturation fronts.

Introduction of the equation (2.4) into the pressure equation (2.2) gives:

$$\underline{\nabla} \cdot \left[k\left(\lambda_t \underline{\nabla} P_w + \lambda_o \Phi \underline{\nabla} J(s) + \lambda_o J(s)\underline{\nabla}\Phi + \lambda_g \underline{\nabla} D\right)\right] = 0. \tag{2.5}$$

It is convenient to reformulate the multipliers in front of the ∇J and $\nabla \Phi$ in terms of total mobility:

$$\lambda_o = \lambda_t - \lambda_w = \lambda_t \left(\frac{\lambda_t - \lambda_w}{\lambda_t} \right) = \lambda_t \left(1 - \frac{\lambda_w}{\lambda_t} \right) = \lambda_t \left(1 - f_w \right). \tag{2.6}$$

Here f_w is the water fractional flow function, equation (1.24).

Substituting the oil phase mobility from equation (2.6) into equation (2.5):

$$\underline{\nabla} \cdot \left[k\lambda_t \left(\underline{\nabla} P_w + (1 - f_w) \Phi \underline{\nabla} J(s) \right) \right]$$
$$+ \underline{\nabla} \cdot \left[k \left(\lambda_t (1 - f_w) J(s) \underline{\nabla} \Phi + \lambda_g \underline{\nabla} D \right) \right] = 0. \tag{2.7}$$

The capillary-viscous potential (CVP) [15] is introduced as:

$$\Upsilon = P_w + \Phi \left(J(s) - \Upsilon_0(s) \right), \tag{2.8}$$

where

$$\Upsilon_0(s) = \int_{s_{wi}}^{s} f \, dJ(s). \tag{2.9}$$

The gradient of the Υ_0 is obtained as:

$$\underline{\nabla} \Upsilon_0(s) = \underline{\nabla} \left(\int_{s_{wi}}^{s} f \, dJ(s) \right) = f \underline{\nabla} J(s). \tag{2.10}$$

Gradient of the potential may be found as:

$$\underline{\nabla} \Upsilon = \underline{\nabla} P_w + \left(J(s) - \Upsilon_0(s) \right) \underline{\nabla} \Phi + \Phi (1 - f_w) \underline{\nabla} J(s). \tag{2.11}$$

Introducing the CVP gradient, equation (2.11) into the pressure equation (2.7) and collecting terms it may be obtained, that:

$$\underline{\nabla} \cdot \left[k\lambda_t \left(\underline{\nabla} \Upsilon \right) + k\lambda_t \left(\Upsilon_0(s) - fJ(s) \right) \underline{\nabla} \Phi \right] + \underline{\nabla} \cdot \left(k\lambda_g \nabla D \right) = 0. \tag{2.12}$$

For convenience,

$$\Omega(s) = \Upsilon_0(s) - fJ(s) \tag{2.13}$$

and, therefore:

$$\underline{\nabla} \cdot \left[k\lambda_t \left(\underline{\nabla} \Upsilon \right) + k\lambda_t \Omega(s) \underline{\nabla} \Phi + k\lambda_g \underline{\nabla} D \right] = 0. \tag{2.14}$$

Solution of equation (2.14) is very similar to the solution of the straightforward pressure equation (2.2) (SFD method) and requires modest changes to the streamline code.

The total velocity in terms of the CVP is formulated as:

$$\underline{u}_t = -k \left(\lambda_t \left(\underline{\nabla} \Upsilon \right) + \lambda_t \Omega(s) \underline{\nabla} \Phi + \lambda_g \underline{\nabla} D \right). \tag{2.15}$$

Introduction of the potential makes it possible to reformulate the pressure equation in such a way that the spatial variation of saturation is taken into account inside the capillary-viscous flow potential. This facilitates easier handling of zones with strong saturation and / or permeability variation.

If the porous medium were homogeneous, the proposed modification leads to the pressure equation, which is identical to the equation without capillary forces.

2.1.3. Saturation equation with capillary and gravity effects

The mass balance equation is represented by the saturation equation. The saturation equation is derived from equation (1.13) with respect to capillary pressure [9]. The water pressure gradient may be expressed from equation (2.1) in terms of capillary pressure and the total velocity:

$$-\underline{\nabla}P_w = \frac{1}{k\lambda_t}\underline{u_t} + \left(1-f_w\right)\underline{\nabla}P_c + \frac{\lambda_g}{\lambda_t}\underline{\nabla}D. \tag{2.16}$$

Introducing the pressure gradient into the Darcy velocity for the water phase, equation (1.2)

$$\underline{u_w} = k\lambda_w\left[\frac{1}{k\lambda_t}\underline{u_t} + \left(1-f_w\right)\underline{\nabla}P_c + \frac{\lambda_g}{\lambda_t}\underline{\nabla}D - \rho_w g\underline{\nabla}D\right]. \tag{2.17}$$

Regrouping the variables:

$$\underline{u_w} = \frac{\lambda_w}{\lambda_t}\underline{u_t} + k\lambda_w\left(1-f_w\right)\underline{\nabla}P_c + k\left(\lambda_w\frac{\lambda_g}{\lambda_t} - \lambda_w\rho_w g\right)\underline{\nabla}D. \tag{2.18}$$

Considering equation (1.24) and using equation (1.7):

$$\left(1-f_w\right) = \lambda_w\left(1-\frac{\lambda_w}{\lambda_t}\right) = \frac{\lambda_w\lambda_o}{\lambda_t}. \tag{2.19}$$

The gravity term may be simplified as well using equation (1.7) and (1.8):

$$\lambda_w\frac{\lambda_g}{\lambda_t} - \lambda_w\rho_w g = \frac{\lambda_w\left(\lambda_w\rho_w + \lambda_o\rho_o\right)g}{\lambda_t} - \frac{\left(\lambda_w+\lambda_o\right)\lambda_w\rho_w g}{\lambda_t}. \tag{2.20}$$

Regrouping the terms in equation (2.20):

$$\lambda_w\frac{\lambda_g}{\lambda_t} - \lambda_w\rho_w g = \frac{\lambda_o\lambda_w}{\lambda_t}\left(\rho_o - \rho_w\right)g. \tag{2.21}$$

Introducing equations (2.19) and (2.21) into (2.18):

$$\underline{u}_w = f_w\,\underline{u}_t + k\frac{\lambda_w\lambda_o}{\lambda_t}\underline{\nabla}P_c + k\frac{\lambda_o\lambda_w}{\lambda_t}\left(\rho_o - \rho_w\right)g\underline{\nabla}D\,.\qquad(2.22)$$

Introducing the water velocity from the equation (2.22) into the saturation equation (1.13):

$$\phi\frac{\partial s_w}{\partial t} + \underline{\nabla}\cdot\left[f_w\,\underline{u}_t + k\frac{\lambda_w\lambda_o}{\lambda_t}\underline{\nabla}P_c + k\frac{\lambda_o\lambda_w}{\lambda_t}\left(\rho_o - \rho_w\right)g\underline{\nabla}D\right] = 0\,.\qquad(2.23)$$

Regrouping and using the incompressibility assumption, equation (1.9):

$$\phi\frac{\partial s_w}{\partial t} + \underline{u}_t\cdot\underline{\nabla}f_w + \underline{\nabla}\cdot\left(k\frac{\lambda_w\lambda_o}{\lambda_t}\underline{\nabla}P_c\right) + \underline{\nabla}\cdot\left(k\frac{\lambda_o\lambda_w}{\lambda_t}\left(\rho_o - \rho_w\right)g\underline{\nabla}D\right) = 0\,.$$

$$(2.24)$$

The equation (2.24) simplifies to the Rapoport – Leas equation [58] if the gravity is neglected. Neglecting the capillary effects as well results in the Buckley – Leverett equation [22].

2.1.4. Final systems of equations

The SFD method and the CVP formulation result in different governing system of equations. For the SFD method the governing system of equations is comprised of the pressure equation with capillary effects (2.2) and the saturation equation with capillary effects (2.24).

$$\begin{cases}\underline{\nabla}\cdot\left[k\left(\lambda_t\underline{\nabla}P_w + \lambda_o\underline{\nabla}P_c + \lambda_g\underline{\nabla}D\right)\right] = 0 \\[2mm] \phi\dfrac{\partial s_w}{\partial t} + \underline{u}_t\cdot\underline{\nabla}f_w + \underline{\nabla}\cdot\left(k\dfrac{\lambda_w\lambda_o}{\lambda_t}\underline{\nabla}P_c\right) + \underline{\nabla}\cdot\left(k\dfrac{\lambda_o\lambda_w}{\lambda_t}\left(\rho_o - \rho_w\right)g\underline{\nabla}D\right) = 0\end{cases}$$

$$(2.25)$$

The governing system of equations for the CVP formulation is constructed from the CVP equation (2.14) and the saturation equation with capillary effects (2.24).

$$\begin{cases}\underline{\nabla}\cdot\left[k\lambda_t\left(\underline{\nabla}\Upsilon\right) + k\lambda_t\Omega(s)\underline{\nabla}\Phi + k\lambda_g\underline{\nabla}D\right] = 0 \\[2mm] \phi\dfrac{\partial s_w}{\partial t} + \underline{u}_t\cdot\underline{\nabla}f_w + \underline{\nabla}\cdot\left(k\dfrac{\lambda_w\lambda_o}{\lambda_t}\underline{\nabla}P_c\right) + \underline{\nabla}\cdot\left(k\dfrac{\lambda_o\lambda_w}{\lambda_t}\left(\rho_o - \rho_w\right)g\underline{\nabla}D\right) = 0\end{cases}$$

$$(2.26)$$

Further in this chapter the discretization and the solution methods of the governing equations are discussed.

2.2 Solution of the governing systems of equations with capillary and gravity forces

The outline of the streamline simulator with capillary effects (CapSL) is presented below. Further in the text the details of the numerical solution are discussed.

2.2.1. Outline of the modified streamline simulator

The following scheme outlines the structure of the CapSL 2.0 streamline simulator. The blocks which are unchanged, compared to the 3DSL 0.25 scheme (Figure 1-3) have dark gray background; the modified blocks have light gray background; the new blocks have white background.

The discussion of the various numerical solution methods follows the solution scheme in Figure 2-1. The numerical representation of the pressure equation is discussed first then followed by the saturation equation. The time step selection and the mass balance error evaluation are discussed later on in this chapter.
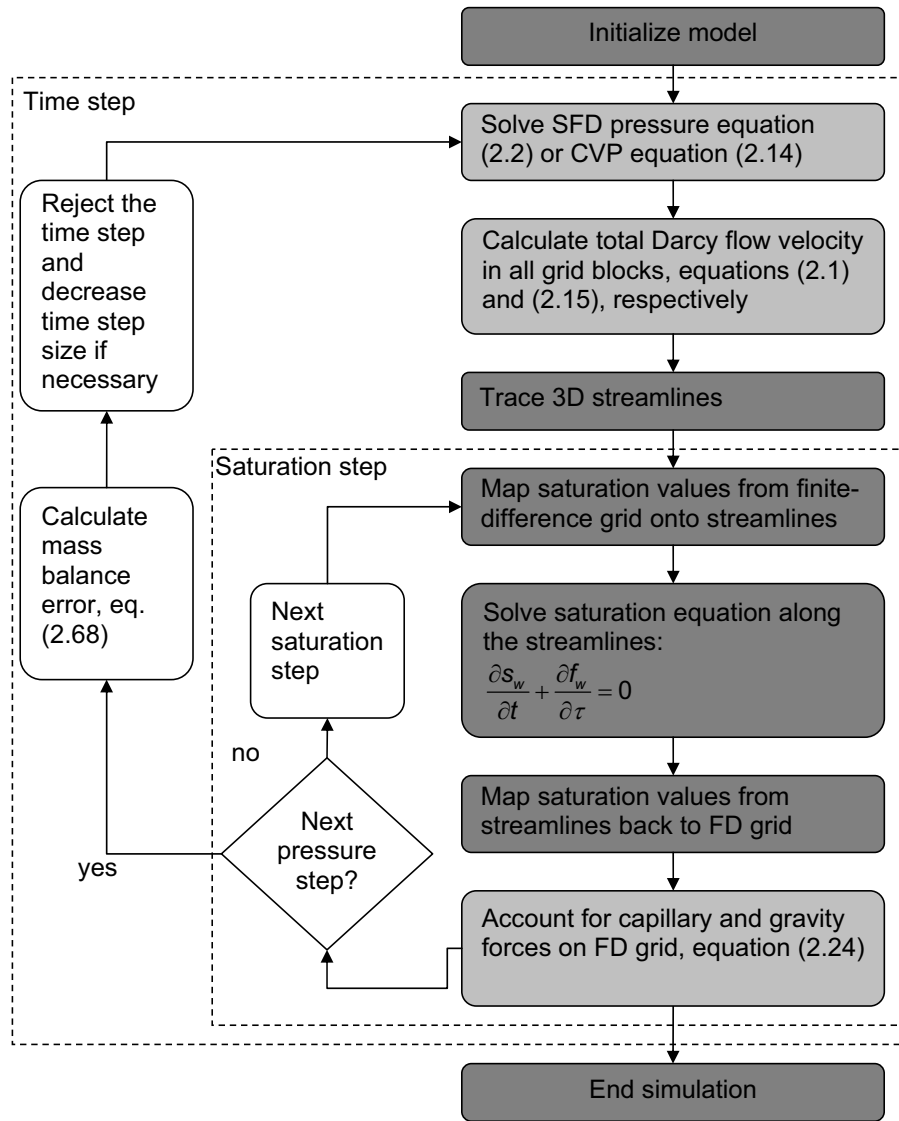
Figure 2-1. Outline of the CapSL streamline simulator.

2.2.2 Numerical representation of the pressure equation

The pressure equation is solved implicitly using 7-point stencil (three dimensions) on the Cartesian grid. The pressure is treated implicitly; the phase mobilities, gravity and capillary forces are treated explicitly. Complete description of the pressure equation discretization may be found in Aziz and Settari [5], Mattax [52] and Batycky [8]. Here only the discretization of the capillary pressure gradient is presented:

$$\nabla \cdot \left[k\lambda_o \cdot \nabla P_c \right] = \frac{\partial}{\partial x}\left[k\lambda_o \frac{\partial P_c}{\partial x} \right] + \frac{\partial}{\partial y}\left[k\lambda_o \frac{\partial P_c}{\partial y} \right] + \frac{\partial}{\partial z}\left[k\lambda_o \frac{\partial P_c}{\partial z} \right].$$

(2.27)

Explicit treatment of the capillary term means that the capillary pressure is computed based on the saturation values from the previous time step [54]. The finite difference approximation is written as:

$$\Delta\left[C\,\Delta P_c \right]_{i,j,k} = \left[\Delta_x\left(C^x\,\Delta_x P_c \right) + \Delta_y\left(C^y\,\Delta_y P_c \right) + \Delta_z\left(C^z\,\Delta_z P_c \right) \right]_{i,j,k}.$$

(2.28)

Here C is the capillary transmissibility, as shown below; index i corresponds to the discretization along the x-axis, j along the y axis and k along the z axis.

Each term on the right hand side of equation (2.28) is expended using centered second-difference equation [5, 56] for all grid blocks i,j,k:

$$\Delta_x\left(C^x\,\Delta_x P_c \right) = \frac{C^X_{i+1/2,j,k}\left[P_{c,i+1} - P_{c,i} \right]_{jk} + C^X_{i-1/2,j,k}\left[P_{c,i-1} - P_{c,i} \right]_{jk}}{\left(\Delta x \right)^2};$$

(2.29)

$$\Delta_y\left(C^y\,\Delta_y P_c \right) = \frac{C^Y_{i,j+1/2,k}\left[P_{c,j+1} - P_{c,j} \right]_{ik} + C^Y_{i,j-1/2,k}\left[P_{c,j-1} - P_{c,j} \right]_{ik}}{\left(\Delta y \right)^2};$$

(2.30)

$$\Delta_z\left(C^z\,\Delta_z P_c \right) = \frac{C^Z_{i,j,k+1/2}\left[P_{c,k+1} - P_{c,k} \right]_{ij} + C^Z_{i,j,k-1/2}\left[P_{c,k-1} - P_{c,k} \right]_{ij}}{\left(\Delta z \right)^2}.$$

(2.31)

The coefficients C^x, C^y and C^z are representing the inter-block transmissibility for a block-centered grid. As it is stated by Aziz and Settari [5] there is no unique way for obtaining the inter-block transmissibility term. Typically, the harmonic averaging resulting in the most accurate prediction of the flow rate is used. The harmonic averaging is derived from the assumption of the piecewise constant interface transmissibility [5].

The transmissibility is introduced on an example of $C^z_{i,j,k+1/2}$ as:

$$C^z_{i,j,k+1/2} = \frac{A}{\Delta z_{k+1/2}} k_{k+1/2} \lambda_{o,k+1/2} . \tag{2.32}$$

Here $\Delta z_{k+1/2}$ is the distance between centers of two neighboring blocks, A is the interface area between two blocks, and $k_{k+1/2} \lambda_{k+1/2}$ is the harmonic average of the properties between the neighboring blocks, introduced as:

$$k_{k+1/2} \lambda_{k+1/2} = \frac{\delta_k + \delta_{k+1}}{\dfrac{\delta_k}{k_k \lambda_{o,k}} + \dfrac{\delta_{k+1}}{k_{k+1} \lambda_{o,k+1}}} , \tag{2.33}$$

here δ is the distance from the center to the interface. Equations (2.32) and (2.33) may be used for the calculation of the transmissibilities at any interface, not necessarily coinciding with block faces. For the inter-block interface:

$$\delta_k = \frac{\Delta z_k}{2} . \tag{2.34}$$

Introducing equation (2.34) into (2.33):

$$k_{k+1/2} \lambda_{k+1/2} = \frac{\Delta z_k + \Delta z_{k+1}}{\dfrac{\Delta z_k}{k_k \lambda_{o,k}} + \dfrac{\Delta z_{k+1}}{k_{k+1} \lambda_{o,k+1}}} . \tag{2.35}$$

Introducing the harmonic average, equation (2.35) into the capillary transmissibility, equation (2.32):

$$C_{i,j,k+1/2} = \frac{A}{\Delta z_{k+1/2}} \frac{\Delta z_k + \Delta z_{k+1}}{\dfrac{\Delta z_k}{k_k \lambda_{o,k}} + \dfrac{\Delta z_{k+1}}{k_{k+1} \lambda_{o,k+1}}} . \tag{2.36}$$

Considering that

$$\Delta z_{k+1/2} = \frac{\Delta z_k}{2} + \frac{\Delta z_{k+1}}{2} , \tag{2.37}$$

the capillary transmissibility is obtained as:

$$C_{i,j,k+1/2}^{z} = \frac{2\,A_{k+1/2}}{\dfrac{\Delta z_k}{k_k \lambda_{o,k}} + \dfrac{\Delta z_{k+1}}{k_{k+1} \lambda_{o,k+1}}} \,.$$ (2.38)

The capillary transmissibilities in all three-dimensions are shown in Table 2-1.

$x_{i+0.5,j,k}$	$y_{i,j+0.5,k}$	$z_{i,j,k+0.5}$
$\dfrac{2\,\Delta y_i\,\Delta z_i}{\dfrac{\Delta x_i}{k_i \lambda_{o,i}} + \dfrac{\Delta x_{i+1}}{k_{i+1} \lambda_{o,i+1}}}$	$\dfrac{2\,\Delta x_j\,\Delta z_j}{\dfrac{\Delta y_j}{k_j \lambda_{o,j}} + \dfrac{\Delta y_{j+1}}{k_{j+1} \lambda_{o,j+1}}}$	$\dfrac{2\,\Delta x_k\,\Delta y_k}{\dfrac{\Delta z_k}{k_k \lambda_{o,k}} + \dfrac{\Delta z_{k+1}}{k_{k+1} \lambda_{o,k+1}}}$

Table 2-1. Capillary transmissibilities C^x, C^y and C^z for the SFD method.

As it is mentioned above the solution of the CVP equation is similar to the solution of the SFD modified pressure equation. The multiplier of the capillary viscous potential gradient $\underline{\nabla}\Upsilon$ in equation (2.14) coincides with the multiplier of the water pressure gradient in the equation (2.2). Gravity term in both equation is exactly the same as well. The only difference between SFD method and the CVP equation lies in the discretization of the additional capillary term. By the analogy with equations (2.27)-(2.29) the $\underline{\nabla}\Phi$ gradient is discretised as:

$$\Delta\left[N\Delta\Phi\right]_{i,j,k} = \left[\Delta_x\left(N^x \Delta_x \Phi\right) + \Delta_y\left(N^y \Delta_y \Phi\right) + \Delta_z\left(N^z \Delta_z \Phi\right)\right]_{i,j,k}.$$

(2.39)

$x_{i+0.5,j,k}$	$y_{i,j+0.5,k}$	$z_{i,j,k+0.5}$
$\dfrac{2\,\Delta y_i\,\Delta z_i}{\dfrac{\Delta x_i}{k_i \lambda_{t,i}\Omega_i(s)} + \dfrac{\Delta x_{i+1}}{k_{i+1}\lambda_{t,i+1}\Omega_{i+1}(s)}}$	$\dfrac{2\,\Delta x_j\,\Delta z_j}{\dfrac{\Delta y_j}{k_j \lambda_{t,j}\Omega_j(s)} + \dfrac{\Delta y_{j+1}}{k_{j+1}\lambda_{t,j+1}\Omega_{j+1}(s)}}$	$\dfrac{2\,\Delta x_k\,\Delta y_k}{\dfrac{\Delta z_k}{k_k \lambda_{t,k}\Omega_k(s)} + \dfrac{\Delta z_{k+1}}{k_{k+1}\lambda_{t,k+1}\Omega_{k+1}(s)}}$

Table 2-2. Capillary transmissibilities N^x, N^y and N^z for the CVP method.

Each term on the right hand side of the equation (2.39) is expended using centered second-difference scheme. For the discretization along x-axis:

$$\Delta_x \left(N^x \, \Delta_x \Phi \right) = \frac{N^X_{i+1/2,j,k} \left[\Phi_{c,i+1} - \Phi_{c,i} \right]_{jk} + N^X_{i-1/2,j,k} \left[\Phi_{c,i-1} - \Phi_{c,i} \right]_{jk}}{\left(\Delta x \right)^2} ;$$

(2.40)

The pressure equation is solved on the finite-difference grid limited by the impermeable boundary conditions around the simulated reservoir. The impermeable boundary can be interpreted as an imaginary layer of grid blocks with absolute zero permeability, located around the specified reservoir. This boundary condition does not require modification for the simulation with capillary effects.

The governing pressure equations in the systems (2.26) and (2.25) are derived using the total incompressibility assumption far from the wells. For the grid block containing a well an additional source / sink term is added to the right-hand side of the pressure equation, see equation (1.11).

2.2.3. Well equations accounting for capillary effects

The wells can be restricted either by the flow rate or by the pressure. The well model in the streamline simulator is rather simplistic, compared to the finite-difference simulators [8].

The total flow rate out of the well is obtained as a sum of the flow rates in all the layers where the well is completed and opened:

$$q_s = \sum_{k=1}^{n_l} T_k^{well} \left(P_k^{well} - P_k \right),$$

(2.41)

where P_k^{well} is the pressure in the wellbore, P_k is the pressure in the block and n_l is the number of layers containing the well. The layer transmissibility term is given by [5]:

$$T_k^{well} = \frac{2\pi \Delta z_k}{\ln \left(\dfrac{r_{o,k}}{r_{w,k}} \right) + s_k} \lambda_{t,k} .$$

(2.42)

Here s_k is the skin factor, $r_{o,k}$ is the Peaceman radius [56], $r_{w,k}$ is the wellbore radius, and index k stays for current block.

If the well pressure is specified, equation (2.41) is used to compute the well flow rate. If the well is restricted by the flow rate, equation (2.41) is used to obtain the well pressure.

To account for capillary effects, the equation (2.41) should be evaluated for each phase, since the phase pressures are different:

$$q_{s,j} = \sum_{k=1}^{n_I} \frac{2\pi\Delta z_k}{\ln\left(\dfrac{r_{o,k}}{r_{w,k}}\right) + s_k} \lambda_j^k \left(P_{k,j}^{well} - P_{k,j}\right), \tag{2.43}$$

here j denotes water or oil phases.

Adding the phase rates and considering that the pressures of the fluids in the well are equal:

$$q_s = \sum_{k=1}^{n_I} T_k^{well}\left(P_k^{well} - \frac{\lambda_w}{\lambda_t}P_{w,k} - \frac{\lambda_o}{\lambda_t}P_{o,k}\right). \tag{2.44}$$

Substituting the capillary pressure, equation (1.21) instead of the oil phase pressure it is obtained:

$$q_s = \sum_{k=1}^{n_I} T_k^{well}\left[P_k^{well} - P_{w,k} - \frac{\lambda_o}{\lambda_t}P_{c,k}\right]. \tag{2.45}$$

The equation (2.45) is derived for the SFD method of introduction of capillary effects into the pressure equation. To obtain the CVP well equation the water pressure in equation (2.45) is substituted with the capillary-viscous potential, equation (2.8):

$$q_s = \sum_{k=1}^{n_I} T_k^{well}\left[P_{bhp}^{well} - \Upsilon_k + \Phi_k\left(J_k(s) - \Upsilon_0(s)\right) - \frac{\lambda_o}{\lambda_t}\Phi_k J_k(s)\right]. \tag{2.46}$$

Reformulating :

$$\Phi_k\left(J_k(s) - \Upsilon_0(s)\right) - \frac{\lambda_o}{\lambda_t}\Phi_k = \Phi_k\left[f_w J_k(s) - \Upsilon_0(s)\right], \tag{2.47}$$

Applying equation (2.13):

$$q_s = \sum_{k=1}^{n_l} T_k^{well} \left[P_{bhp}^{well} - \Upsilon_k + \Omega(s)\Phi_k \right]. \tag{2.48}$$

The gravitational effects are introduced by relating the pressure in the grid block to the user-specified pressure value in the certain grid block [5, 8]:

$$P_k^{well} = P_{bhp}^{well} + 0.5 \sum_{i=1, i\neq bhp}^{k} \left(\gamma_{i-1} + \gamma_i \right)\left(D_i - D_{i-1} \right), \tag{2.49}$$

here index *bhp* stands for the bottom hole pressure and the block were it is specified and γ is the ratio of the total gravity mobility to the total mobility:

$$\gamma_i = \frac{\lambda_{g,i}}{\lambda_{t,i}}. \tag{2.50}$$

In the current formulation the well pressure is specified in the top well containing grid block. Therefore equation (2.49) is evaluated for all the grid blocks containing well, except for the top one. Introducing equation (2.49) into the boundary condition for the SFD method (2.45):

$$q_s = \sum_{k=1}^{n_l} T_k^{well} \left[P_{bhp}^{well} - P_{w,k} - \frac{\lambda_o}{\lambda_t} P_{c,k} + \frac{1}{2} \sum_{i=2}^{k} (\gamma_{i-1} + \gamma_i)(D_i - D_{i-1}) \right], \tag{2.51}$$

and the CVP method (2.48):

$$q_s = \sum_{k=1}^{n_l} T_k^{well} \left[P_{bhp}^{well} - \Upsilon_k + \Omega(s)\Phi_k + \frac{1}{2} \sum_{i=2}^{k} (\gamma_{i-1} + \gamma_i)(D_i - D_{i-1}) \right]. \tag{2.52}$$

2.2.4. Calculating the flow velocity

After the pressure values are obtained on the finite difference grid the streamlines are traced using the Darcy velocity. The total flow velocity for both methods is calculated as a sum of the average block transmissibilities multiplied by the corresponding gradients and divided by the cross-sectional area of the block interface. For the SFD method the grid block total velocity over the *k+1/2* face is calculated as:

$$u_{t,k+\frac{1}{2}} = \frac{T_{k+\frac{1}{2}}}{A_{k+\frac{1}{2}}}\left(P_{k+1} - P_k\right) + \frac{C_{k+\frac{1}{2}}}{A_{k+\frac{1}{2}}}\left(P_{C,k+1} - P_{C,k}\right) + \frac{G_{k+\frac{1}{2}}}{A_{k+\frac{1}{2}}}\left(D_{k+1} - D_k\right).$$

(2.53)

The total velocity in terms of the CVP is found as:

$$u_{t,k+\frac{1}{2}} = \frac{T_{k+\frac{1}{2}}}{A_{k+\frac{1}{2}}}\left(\Upsilon_{k+1} - \Upsilon_k\right) + \frac{N_{k+\frac{1}{2}}}{A_{k+\frac{1}{2}}}\left(\Phi_{C,k+1} - \Phi_{C,k}\right) + \frac{G_{k+\frac{1}{2}}}{A_{k+\frac{1}{2}}}\left(D_{k+1} - D_k\right).$$

(2.54)

Here T is the water pressure and CVP transmissibility, G is the gravity transmissibility as introduced by Batycky [8].

The streamline are traced using the Pollock's methods [57], based on the total velocity calculated by means of equations (2.53) or (2.54).

2.2.5. Solution of the saturation equation

As it is mentioned in Chapter 1, the gravitational effects are typically accounted by tracing so-called gravity lines [8, 21]. The gravity forces act in the vertical direction. The direction of the displacing fluid flow may always be determined from the density difference and is unique for the given simulation case. For the oil-water displacement water, as a denser fluid, tends to move downwards. The gravity lines can be traced for each individual vertical stack of the blocks from the top block down. On the other hand, the direction of the displacing fluid flow under the capillary forces gradient depends upon the fluid saturations and the reservoir properties in each point inside the reservoir. It is impossible to determine a unique direction of the capillary driven flow, or to use some kind of "capillary lines". To avoid using 3 operator splitting steps, accounting for viscous, gravity and capillary forces separately, capillary and gravity forces are simultaneously accounted for on the finite-difference grid. The solution of the saturation equation (2.24) using the operator splitting method is described below.

The viscous forces are accounted for along the streamlines:

$$\phi \frac{\partial s_w}{\partial t_1} + \underline{\mathbf{u}}_t \cdot \underline{\nabla} f_w = 0 \, . \tag{2.55}$$

Using the time of flight concept, presented in Chapter 1 [18, 32, 68] equation (2.55) is transformed from the three-dimensional Cartesian coordinates, to the one-dimensional coordinate along the streamlines:

$$\frac{\partial s_w}{\partial t_1} + \frac{\partial f_w}{\partial \tau} = 0 \, , \tag{2.56}$$

while gravitational and capillary effects are resolved on the finite-difference grid:

$$\frac{\partial s_w}{\partial t_2} + \frac{1}{\phi} \underline{\nabla} \cdot \left(k \frac{\lambda_w \lambda_o}{\lambda_t} \underline{\nabla} P_c \right) + \frac{1}{\phi} \underline{\nabla} \cdot \left(k \frac{\lambda_o \lambda_w}{\lambda_t} \left(\rho_o - \rho_w \right) g \underline{\nabla} D \right) = 0 \tag{2.57}$$

Equation (2.56) requires a single boundary condition, which is specified at the injection well:

$$s\big|_{\tau=0} = s_{injected} \, . \tag{2.58}$$

Solution of the equation (2.56) is described by Batycky [8]. After the equation (2.56) is solved along the streamlines, the saturations are mapped back to the finite-difference grid [8].

Equation (2.57) is solved explicitly on the finite difference grid. This step is referenced as a corrector step, capable of relocating the fluids inside the porous media, but not changing their total amounts. The simulation space for the corrector step is bounded by the no-flow boundaries and does not contain any source or sink terms. A first-order forward-in-time, backward-in-space finite-difference scheme [55] is used. For simplicity the discretized form of the equation (2.57) is shown in one dimension along the x-axis:

$$\frac{s_{w,i}^{n+1} - s_{w,i}^n}{\Delta t} + \frac{1}{\phi} \left(C_{i+1/2}^n \frac{P_{c,i+1}^n - P_{c,i}^n}{\left(\Delta x \right)^2} - C_{i-1/2}^n \frac{P_{c,i}^n - P_{c,i-1}^n}{\left(\Delta x \right)^2} \right)$$

$$+ \frac{1}{\phi} \left(G_{i+1/2}^n \frac{D_{i+1}^n - D_i^n}{\left(\Delta x \right)^2} - G_{i-1/2}^n \frac{D_i^n - D_{i-1}^n}{\left(\Delta x \right)^2} \right) = 0 \, , \tag{2.59}$$

here C and G are correspondingly capillary and gravity transmissibilities, described in the previous section.

The three-dimensional discretization form contains Δy and Δz terms similar to the Δx term in equation (2.59).

An important question arises during solution of the saturation equation (2.59) when a displacement front (more generally, the capillary transition zone) moves from one block to another. The multiplier of the capillary and gravity gradients, equation (2.57) contains the $k\dfrac{\lambda_w \lambda_o}{\lambda_t}$ term. For the reservoir simulation problems the oil phase is immobile at the irreducible water saturation, as well as the water phase is immobile at the residual oil saturation. Therefore the product of phase mobilities is often close to zero in the block behind and the block ahead the displacement front. For the solution procedures, based on the center-point grids, used both in Eclipse and CapSL, this fact might create certain numerical problems. Generally the transmissibility terms $C_{i+1/2}^n$ and $G_{i+1/2}^n$ can be found using the *i-th+1* block properties, the *i-th* block properties or by averaging the $k\left(\lambda_w \lambda_o / \lambda_t\right)$ values of these two blocks. As it is mentioned above, typically, the harmonic averaging of the $k\left(\lambda_w \lambda_o / \lambda_t\right)$ values in the neighboring blocks is used :

$$\Lambda_{i+1/2}^n = \frac{\delta_i + \delta_{i+1}}{\dfrac{\delta_i}{k_i \dfrac{\lambda_{w,i}\lambda_{o,i}}{\lambda_{t,i}}} + \dfrac{\delta_{i+1}}{k_{i+1}\dfrac{\lambda_{w,i+1}\lambda_{o,i+1}}{\lambda_{t,i+1}}}} \ , \qquad\qquad (2.60)$$

where δ_i is the distance from the i-th block center to the boundary.

And the capillary transmissibility is found as:

$$C_{i+1/2}^n = \frac{A}{\Delta x_{i+1/2}}\Lambda_{i+1/2}^n . \qquad\qquad (2.61)$$

If the mobility of any of the phases in any of the neighboring blocks approaches zero, corresponding $\delta_i \lambda_{t,i} / k_i \lambda_{w,i}\lambda_{o,i}$ approaches infinity, therefore the $\Lambda_{i+1/2}^n$ approaches zero. As a result, the IMPES Eclipse saturation step, and the CapSL corrector step equation (2.59), have two requirements to be able to redistribute fluids between two blocks with respect to capillary and gravitational forces:

- Both grid blocks must have the water saturation at least slightly higher than initial water saturation. For the CapSL, this means that grid blocks must be flooded during solution along the streamlines and for Eclipse, that the blocks must be flooded by the viscous flow during the previous time step.

- Both grid blocks must have the oil saturation higher than residual oil saturation. Therefore, if the water penetrates into the previously unflooded grid block it should not fill it up to the maximum water saturation during the single saturation time step.

Aziz and Settari [5] also state that for the multiphase flow the choice of the averaging might be dictated by the numerical techniques used. In case of capillary forces the harmonic averaging of the λ_d may not be the best choice, since it may require time step smaller than IMPES stability condition, making both simulators slower and more dispersed.

In reality, the displacement front represents a zone with a wide range of saturations, and an average mobility in this zone highly differs from the mobilities at its ends. An average mobility of oil and water in the capillary transition zone corresponds to mobility at some average saturation between the saturation values behind and ahead of the displacement front. For the sake of simplicity, one may take an arithmetic average saturation:

$$s_{i+1/2} = \frac{\Delta z_i s_i + \Delta z_{i+1} s_{i+1}}{\Delta z_i + \Delta z_{i+1}} \tag{2.62}$$

and to calculate the phase mobilities on the border corresponding to this average saturation:

$$\Lambda_{i+1/2}^n = \frac{\delta_i + \delta_{i+1}}{\dfrac{\delta_i}{k_i} + \dfrac{\delta_{i+1}}{k_{i+1}}} \cdot \frac{\lambda_w \left(s_{i+1/2}\right) \lambda_o \left(s_{i+1/2}\right)}{\lambda_t \left(s_{i+1/2}\right)} \cdot \tag{2.63}$$

To distinguish the methods further in the text the saturation equation solution using equation (2.60) is called harmonic mean method. The saturation equation solution using equation (2.63) is called average saturation method.

In many simple cases there is no difference between using the harmonic mean and the average saturation method. However, in certain cases the latter method should provide better simulation results. Comparison of the simulation results obtained using these two methods is presented in Chapter 3.

The outline of the solution routine for the equation (2.59) is as follows:

1. Start with the first grid block;
2. Calculate capillary and gravity flux through all the faces of the grid block;
3. Calculate and save the water saturation change in the current block due to all fluxes;
4. Repeat steps 2-3 for all the grid blocks;
5. Calculate the saturation values on the current time step using the saturation on the previous step and the saved saturation change values.

The explicit solution scheme used for the corrector step is conditionally stable [55] and requires limitation of the time step size [29]:

$$\frac{F_i \Delta t}{V_{pi}} \leq 1, \tag{2.64}$$

where Δt is the maximum stable time step, V_p is the grid block pore volume and F is some function of rates, reservoir and fluid properties.

Flux F is evaluated for each grid block as maximum total gravity and capillary flux through any face of the block. The maximum stable time step is calculated as:

$$\Delta t \leq \max_{j=1..6} \left[\frac{C_j \left(P_{C,i\rightarrow j} - P_{C,i} \right) + G_j \left(D_{i\rightarrow j} - D_i \right)}{V_{pi}} \right], \tag{2.65}$$

where index j represents one of the six faces of the grid block in the Cartesian 7-point stencil,   index i represents the current grid block and index $i \rightarrow j$ represents the neighboring block through the face j.

In case of very strong capillary forces in a heterogeneous porous medium with large permeability variation the corrector step may result in "overshoot" of the saturation values in some grid blocks. That is the saturation in some specific blocks become larger than 1-s_{or}. Such an overshoot is the result of the explicit

treatment of the phase mobilities during a single corrector step. In this case the corrector step is rejected and repeated with half the current time step.

2.2.6. Possibilities for the material balance error

Main sources of the numerical error in the black oil streamline simulator accounting for the gravity and / or capillary effects are:

- Mapping from finite-difference grid to streamlines and back;
- The operator splitting error.

The numerical errors associated with mapping are described by Mallison et al. [48]. Mallison et al. also suggest modifications to the mapping routine allowing a significant decrease in the mapping error. It is easy to comprehend that the mapping error increases with increase of the number of remappings performed. This ultimately means that the mapping error increases with increase of the number of time steps.

On the other hand, solution of the operator splitting method converges to the analytical solution at infinitely large number of time steps. Strictly speaking it should be possible to estimate the "optimal" number of time steps, where the total numerical error is at minimum, as sketched on Figure 2-2.
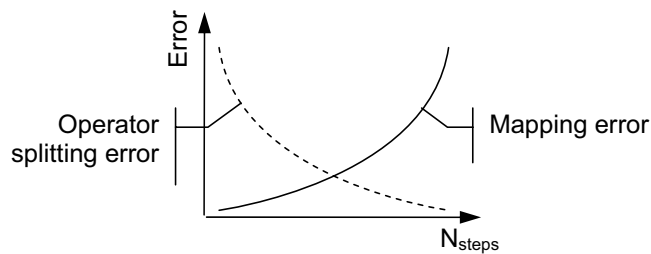
Figure 2-2. The mapping and the operator splitting errors.

2.2.7. Time step selection

The CapSL, in its current formulation, has several different time step types. The first one is the pressure update time step, discussed here. The other two time steps control the solution of the saturation equation. The time step t_1 is associated with solution of equation (2.56) along the streamlines. One-dimensional explicit solution of the saturation equation along a given streamline is restricted by the local CFL condition. Therefore, the time step along each streamline is introduced [8]. The value of another time step - t_2 is related to the solution of the "corrector" step on the finite difference grid, equation (2.57) and is discussed above. Equations (2.56) and (2.57) may be consecutively solved several times for each pressure time step to correctly account for the cross flow due to capillary and/or gravity forces. To avoid confusion between different time steps of the streamline method the "time step" term is used with regard to the pressure update time step. Each pressure update time step may include one or more "saturation steps". The "saturation step" term is used in regard to single solution of the saturation equation, including both the solution along the streamlines and on the finite difference grid. The stable saturation step size is equal to the smallest of the step along the streamlines or on the finite difference grid. Typically the gravity / capillary step on the finite difference grid is smaller than the viscous step along the streamlines, therefore the saturation time step size is limited by the stability condition of the corrector step, equation (2.57). The size of the saturation step is determined using equation (2.66). Several saturation steps might be performed during each time step. This allows decreasing the operator splitting error of the saturation step without recalculating the pressure field.

Selection of a stable time step size for the pressure update time step poses a rather complicated problem. Compared to the finite-difference methods the restrictions on the time step size of the streamline method are lifted mainly due to complete decoupling of the pressure and the saturation update time steps [8]. Such decoupling is possible due to the movement of the fluids along the streamlines. This leads to two advantages: 1) the solution of the saturation

equation is limited by the stability criteria along the particular streamline, not by the largest flow velocity in the whole simulated domain; 2) the pressure equation does not have to be recalculated every time the saturation equation is solved.

Therefore the only remaining question about time step selection is the question of convergence. In other words: how many pressure updates are necessary to accurately capture non-linearity of the displacement?

Two different methods of the time step selection are available. The first one is based on the user-specified output times. This method attempts to make the time step as large as the user-specified saturation or pressure output times or the well history specifications allow. The time step can be rejected if the mass balance error is too large. Details of the mass balance error evaluation and the time step rejection are provided below. The second time step selection routine is based on the paper by Ichiro et al. [40]. The stability condition for the streamline method is derived from the three-dimensional IMPES stability condition [67]:

$$Cn = \frac{\Delta t}{\phi}\left(\frac{u_x}{\Delta x} + \frac{u_y}{\Delta y} + \frac{u_z}{\Delta z}\right)f'_w,$$ (2.66)

and for the streamline method the velocity in the stability condition is substituted for the correction velocity, which is the difference between initial and instantaneous velocity at the current step. It is assumed that the change in the volumetric flux through the block face is proportional to the time step size and for each block it may be found as:

$$Cn = \frac{\Delta t}{PV}\sum_{inflow}\left((q_f - q_0)\max_{S_w}\left(\frac{f_w}{s_w}\right)\right),$$ (2.67)

here Cn is the Courant number: the dimensionless number allowing to take the time steps smaller or larger than the stable time step [29]; Δt is the time step; PV is the pore volume of the block; q_f is the volumetric flux after the time step; q_0 is the volumetric flux before the time step. On the basis of the equation (2.67) the size of the next time step may be estimated from the maximum change of the velocity during the current step. The method suggested is used to estimate the size of the next time step, based on the size of the current time step and the

flow velocity change. The method described above provides a quick, CPU-cheap and efficient solution to estimate the time step size.

A better time step selection algorithm may probably be obtained by following the method suggested by Coats [28]. This method is obtained for the finite-difference IMPES solution and should be re-evaluated for the streamline method.

After the time step is performed the mass balance error is evaluated:

$$E = V_{water,initial} + \sum_{i=1}^{n_{steps}} V_{water,injected} - \sum_{i=1}^{n_{steps}} V_{water,produced} - V_{water,in\ place} . \qquad (2.68)$$

Here V is volume and n_{steps} is the number of time steps performed.
If the mass balance error exceeds the user-specified value, the step may be rejected and repeated with, for example, half the current time step size.

Originally in 3DSL Batycky [8] suggested another method, the so-called "true time". The underlying idea is to find a "true" time step size from the cumulative water balance on the given time step, see Section 1.3.3. As a result the mass balance error is "converted" into the time step size error. However, the streamline simulator is based on the numerical approximations, rather than on the exact analytical solutions. Any approximation and therefore any numerical method have an error associated with it. Two main sources of the numerical error in the streamline simulation are mentioned above. A numerical error is as important parameter as the solution speed. It is important not only to compare how fast the numerical simulation delivers the predictions, but how fast the numerical simulation delivers the predictions within the certain level of accuracy. It should also be mentioned that for the viscous dominated simulation runs the mass balance error is typically very small and the time steps are rather large. As a result the correction to the time step size does not have any serious effects on the simulation times.

2.3. Illustration of the capillary effects

A simple illustration of the capillary effects is given on an example of the homogeneous water wet reservoir with the low permeable intrusion, as shown in Figure 2-3. The run-specific data are combined in Table 2-3.
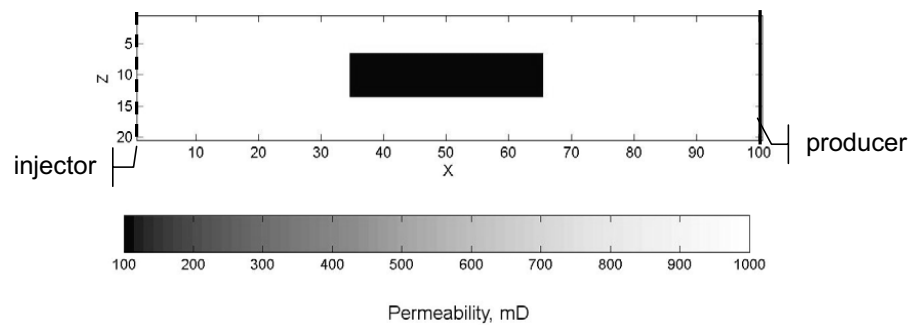
Figure 2-3. Permeability field with the low permeable zone (100 mD) inside the high permeable reservoir (1000 mD).

The relative permeability values are simple second order dependencies of the saturation. The Leverett function is constructed using the van Genuchten model [77]. The relative permeability curves and the Leverett function are specified in the tabulated form in the input to both the Eclipse and the CapSL. The plots are constructed from the same number of data points connected by the straight lines between two points.

The four decimals in the s_{max} and the s_{min} values are necessary to reproduce the Leverett function curve as show in Table 2-3. The end points of the Leverett function are extremely sensitive to these values due to the asymptotic behavior of the van Genuchten model [77].
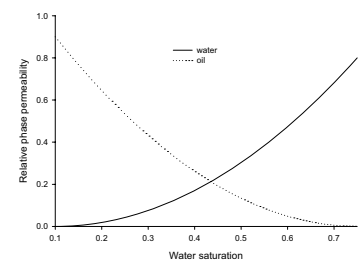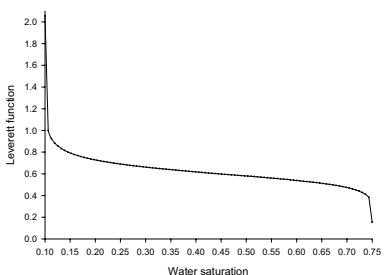
Parameter	Value
Simulation grid	100·20 areal slice; 1·1·1 m grid blocks
Porosity	0.2
Pore volume	400 m^3
Viscosities	Water – 1 cP Oil - 1cP
Relative permeabilities	$k_{rw} = k_{rwor}\left(\dfrac{s - s_{wi}}{1 - s_{wi} - s_{or}}\right)^2$ $k_{ro} = k_{rowi}\left(1 - \dfrac{s - s_{wi}}{1 - s_{wi} - s_{or}}\right)^2$ $k_{rwor} = 0.8$ $k_{rowi} = 0.9$ $s_{wi} = 0.1$ $s_{or} = 0.25$
Densities	Water – 1000 kg/m^3 Oil – 1000 kg/m^3
Injection rate	1.0 m^3/day or 1 pore volume injected (PVI) in 400 days
$P_{production}$	20.5 MPa
σ	30 mN/m
Capillary pressure	$J(s) = \alpha\left[\left(\dfrac{s - s_{min}}{1 - s_{max} - s_{min}}\right)^{-1/m} - 1\right]^{1/n} - y, \quad n = \dfrac{1}{1-m}$ $\alpha = 0.6$ $m = 0.9$ $y = 0$ $s_{min} = 0.0999$ $s_{max} = 0.2499$

Table 2-3. Simulation data for the simulation of the low permeable zone inside the high permeable reservoir.

The displacement fronts neglecting capillary effects are presented in Figure 2-4.

Figure 2-4. Saturation profiles for the low permeable zone inside the high permeable reservoir simulation without accounting for capillary forces.

Two zones are highlighted in Figure 2-4. The solid line surrounds the low permeable zone, the dashed line surrounds the high permeable zone after (corresponding to the direction of the flow) the low permeable zone. These two zones are of the particular interest, since capillary effects are expected to strongly alter the saturation displacement front in these two zones. Figure 2-5 shows the saturation profiles at the same PVI, obtained by the CapSL utilizing the SFD pressure equation modification without accounting for capillary effects in the saturation equation. Figure 2-6 shows the corresponding saturation profiles obtained by the CapSL utilizing the CVP equation without accounting for capillary effects in the saturation equation.

The SFD and the CVP saturation profiles are quite different. The permeability field is symmetric with respect to the horizontal line passing through the middle of it. Therefore the saturation profiles must be symmetric with respect to this line as well. However, the SFD method shows an asymmetry in the saturation profiles.

The increase in the simulation time with capillary effects is below 5% for both methods. This time comparison is preliminary, the detailed information on comparison of the methods is presented in Chapter 3.

Figure 2-5. Saturation profiles for the low permeable zone inside the high permeable reservoir simulation obtained by the CapSL utilizing the SFD method without accounting for capillary effects in the saturation equation.
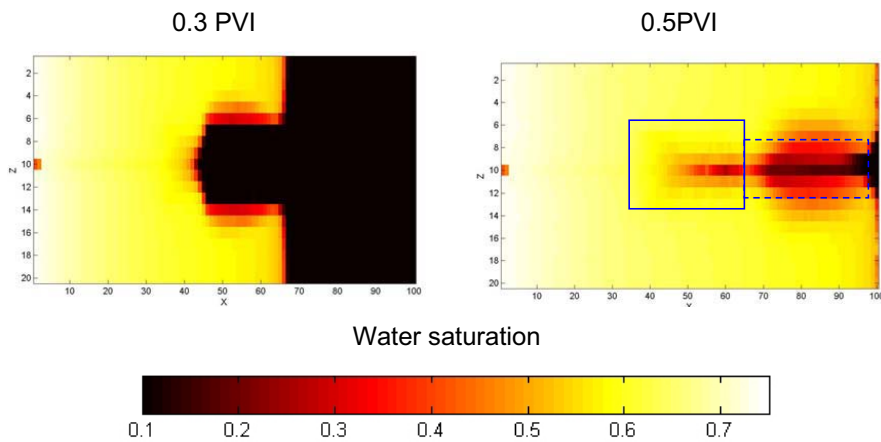
Figure 2-6. Saturation profiles for the low permeable zone inside the high permeable reservoir simulation obtained by the CapSL utilizing the CVP method without accounting for capillary effects in the saturation equation.

As it can be seen from the comparison of Figures 2-5 and 2-6 with Figure 2-4, two main effects of the capillary forces are:

- Higher sweep of the low permeable zone;
- Smearing of the displacement front, resulting in the faster sweep of the high permeable area after the low permeable zone.

The smearing of the saturation front is achieved only due to the change in the total velocity and the location of the streamlines as a result of accounting for the capillary forces in the pressure equation.

The simulation results accounting for the capillary forces both in the pressure and the saturation equations are presented in Figure 2-7.

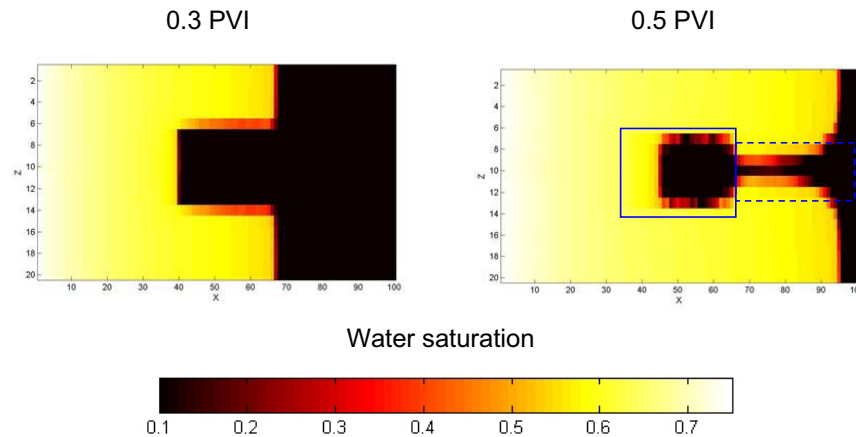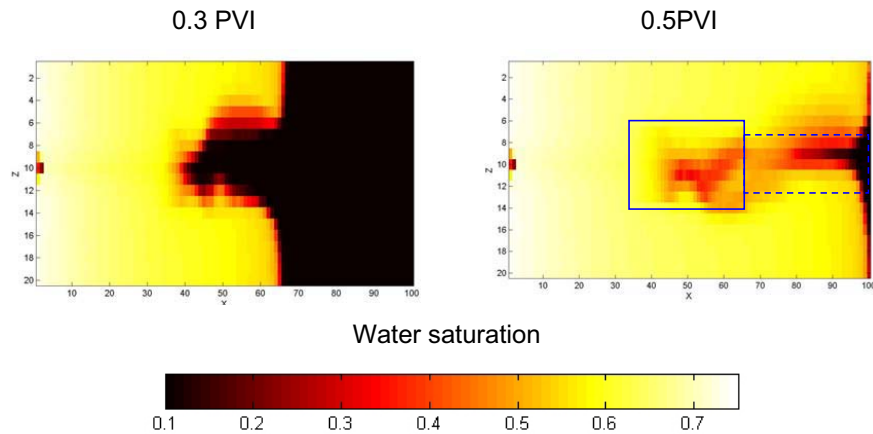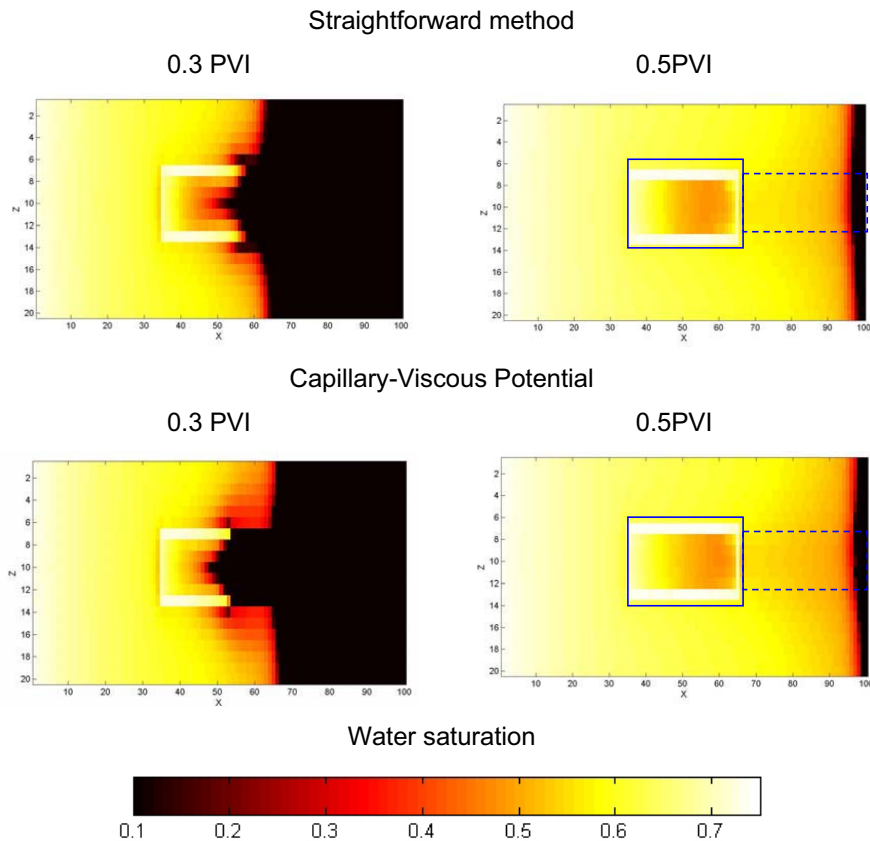*Figure 2-7. Saturation profiles for the low permeable zone inside the high permeable reservoir simulation accounting for capillary forces in the pressure and the saturation equations.*

Simulations using the CVP and the SFD methods show a good match.

Introduction of the capillary effects results in a higher water saturation in the low permeable zone and in smearing of the displacement front. With the capillary effects accounted for both in the pressure and the saturation equations, the average water saturation in the low permeable zone after 0.5 PVI injected has increased approximately twice: from 0.30 to 0.61 compared to the simulation neglecting the capillary forces.

The cumulative oil production curves for 1) simulation neglecting capillary effects; 2) using the CVP method neglecting the capillary effects in the saturation equation; and 3) accounting for capillary effects both in the pressure and the saturation equations are compared on Figure 2-8.
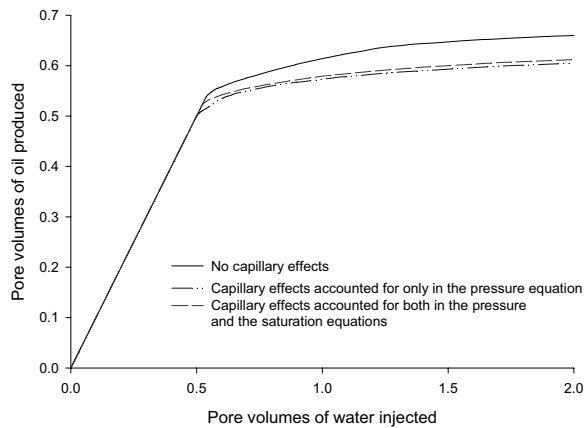
Figure 2-8. Oil production curves for the low permeable zone inside the high permeable reservoir simulation.

The breakthrough occurs at around 0.54 PVI if the capillary effects are neglected, at around 0.5 PVI if the capillary effects are accounted for only in the pressure equation and at 0.53 PVI if the capillary effects are fully accounted for. A faster breakthrough time can be explained by smearing of the saturation front due to the capillary forces. Slowing down the front with respect to the modification of the saturation equation is due to increase of the capillary cross flow.

Comparison of the CapSL (accounting for capillary effects both in the pressure and the saturation equations) and the Eclipse 100 (IMPES mode) predictions after 0.3 and 0.5 PVI, Figures 2-9 and 2-10, respectively, shows that the CapSL predictions result in weaker capillary crossflow.
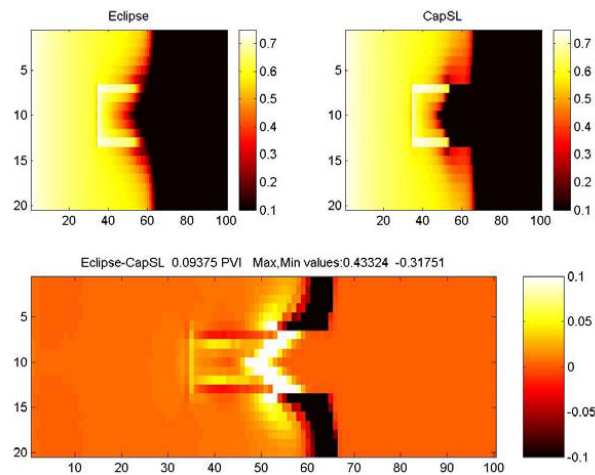
Figure 2-9. Comparison of the Eclipse and the CapSL saturation plots for the low permeable zone inside the high permeable reservoir simulation after 0.3 PVI.
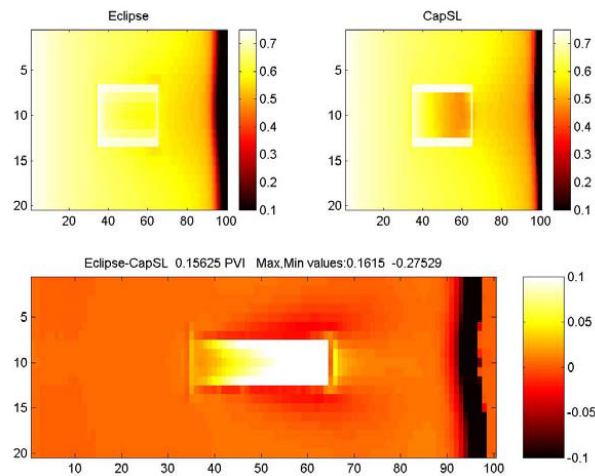
Figure 2-10. Comparison of the Eclipse and the CapSL saturation plots for the low permeable zone inside the high permeable reservoir simulation after 0.5 PVI.

When the average saturation method is used and several saturation steps per time step are performed, the CapSL prediction converges to the Eclipse results, as shown in Figures 2-11 and 2-12.
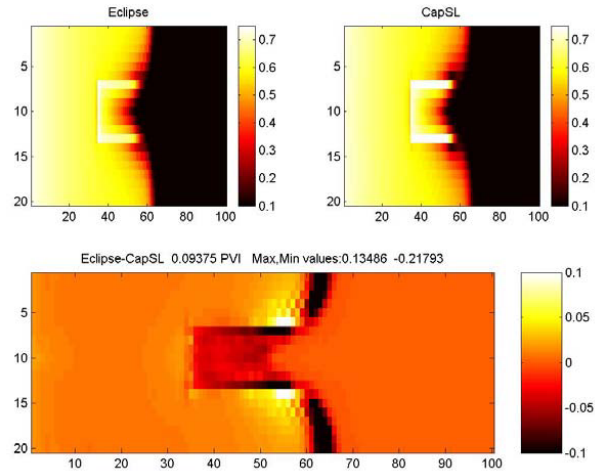
Figure 2-11. Comparison of the Eclipse and the CapSL(using average saturation method) saturation plots for the low permeable zone inside the high permeable reservoir simulation after 0.3 PVI.
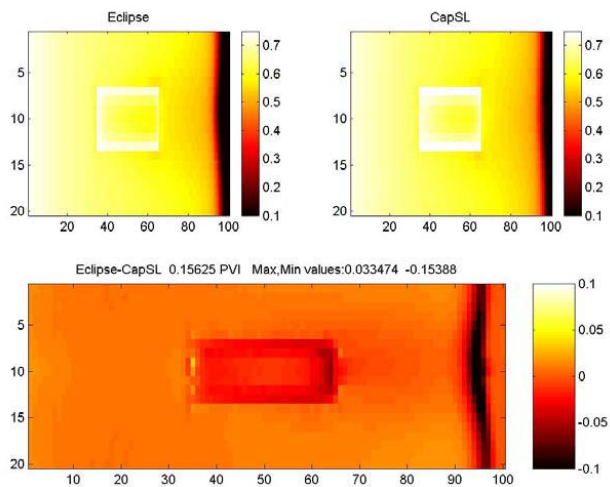
Figure 2-12. Comparison of the Eclipse and the CapSL(using average saturation method) saturation plots for the low permeable zone inside the high permeable reservoir simulation after 0.5 PVI.

However, even in this case the capillary crossflow in the CapSL predictions is slightly lower compared to the Eclipse. One of the possible explanations may be higher numerical dispersion in the Eclipse.

Finally, the comparison of the cumulative oil production curves using the CVP with different saturation equation modifications and the Eclipse 100 is presented in Figure 2-13.
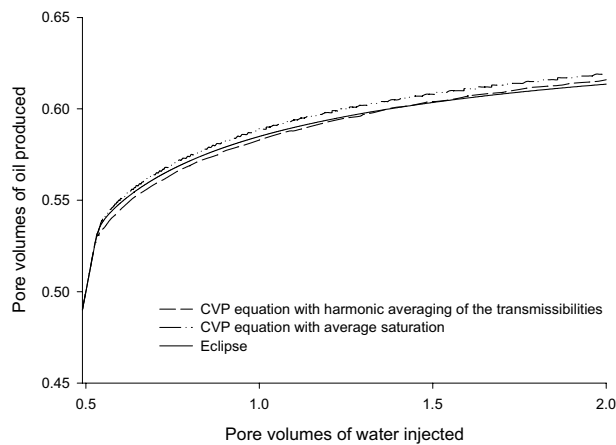
Figure 2-13. Oil production curves predicted by the Eclipse and the CapSL for the low permeable zone inside the high permeable reservoir simulation.

The oil production curves predicted by the CapSL using the average saturation method by the Eclipse show not only a good match in general, but show similar trends.

The maximum mass balance error of the streamline simulator in all the simulations mentioned above remains below 0.2% relative to the pore volume.

The next chapter will present more simulation examples. The CapSL simulator will be tested on the synthetic cases and compared to the Eclipse.

Chapter 3. Comparison of various methods of accounting for capillary effects

The chapter starts with a comparison of the various modification methods described in Chapter 2. Several test cases are presented. The capillary-viscous potential method (CVP) and the straightforward method of introduction of capillary effects into the pressure equation (SFD) are compared first. The saturation equation modifications are discussed. The time step methods are tested.

It is very difficult to compare only the modifications of the pressure equation or only the time step selection routine. A comparison of the CVP and the SFD methods without the time step selection routine and the saturation equation modification is not entirely correct and complete. Introduction of the capillary effects into the pressure equation influences the initial condition of the saturation step by altering the streamline locations. The stability of the modified scheme may restrict or ease up the time steps size limitation. The introduction of capillary effects into the saturation equation influences the pressure equation solution on the next time step through the capillary pressure term. The time step size determines how many local steps along the streamlines and on the finite-difference grid are required due to the CFL (Courant-Freidrich-Levi [76]) stability condition [19, 20] during the single pressure update time step. An attempt is carried out to separately analyze the effects of introduction of capillary effects into the pressure and the saturation equations and the automatic time step size selection routine. However, a lot of cross influence is discovered and discussed.

3.1. Data for the test cases

Extensive comparison have been carried out in different geometries and different heterogeneity scales. Characteristic results for the most striking examples are presented below. Three different simulation cases are chosen to test the streamline simulator:

- The first test case represents a 2D synthetic case, resembling a checkerboard comprised of multiple low and high permeable homogeneous zones;
- The second test case represents a 2D slice of a heterogeneous porous medium;
- The third test case represents a 3D simulation case based on the SPE10 comparative project [24].

The reservoir rock in these simulation cases is considered to be water wet.

3.1.1. Test case 1

The permeability field of the checkerboard test case is presented in Figure 3-1. The rest of the simulation data are presented in Table 3-1.
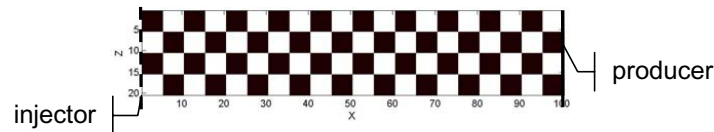
Figure 3-1.Checkerboard permeability field. The low permeable zone (black) is 100.0mD, the high permeable zone (white) is 400.0mD.

This test case represents a heterogeneous medium with the permeability variation in both longitude and transverse directions. This test case is synthetic and from the first glance may look as a simple simulation case, however, it is actually not. Sharp permeability transitions make this case rather complicated to handle by the numerical methods.
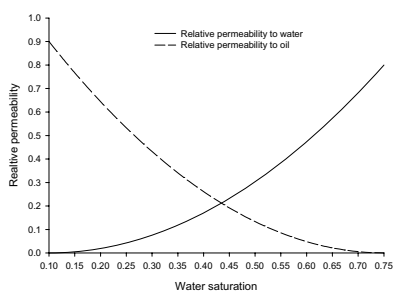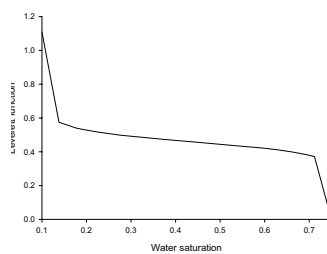
Parameter	Value	
Grid	100·20·1m areal slice; Each checker-block is 5·5m	
Porosity	0.2	
Pore volume	400 m^3	
Viscosities	Water – 1 cP	Oil - 1cP
Relative permeabilities	$k_{rw} = k_{rwor}\left(\dfrac{s - s_{wi}}{1 - s_{wi} - s_{or}}\right)^2$ $k_{ro} = k_{rowi}\left(1 - \dfrac{s - s_{wi}}{1 - s_{wi} - s_{or}}\right)^2$ $k_{rwor} = 0.8$ $k_{rowi} = 0.9$ $s_{wi} = 0.1$ $s_{or} = 0.25$	
Densities	Water – 1000 kg/m^3	Oil – 1000 kg/m^3
Injection rate	1.0 m^3/day (1 pore volume injected in 400 days)	
$P_{production}$	20.5 MPa	
σ	30 mN/m	
Capillary pressure	$$J(s) = \alpha\left[\left(\frac{s - s_{min}}{1 - s_{max} - s_{min}}\right)^{-1/m} - 1\right]^{1/n} - y, \ \ n = \frac{1}{1 - m}$$ $\alpha = 0.5$ $m = 0.93$ $y = 0.05$ $s_{min} = 0.0999$ $s_{max} = 0.75$	

Table 3-1. Simulation data for checkerboard case.

3.1.2. Test case 2

The second test case is similar to the one used by Thiele [70]. This test case represents a two-dimensional slice of a heterogeneous medium. The porosity of the medium is kept constant; however, the permeability varies from 273mD to 135D. The average permeability value is 9D. The permeability field is constructed using log-normal distribution and is presented in Figure 3-2. The simulation data are presented in Table 3-2.
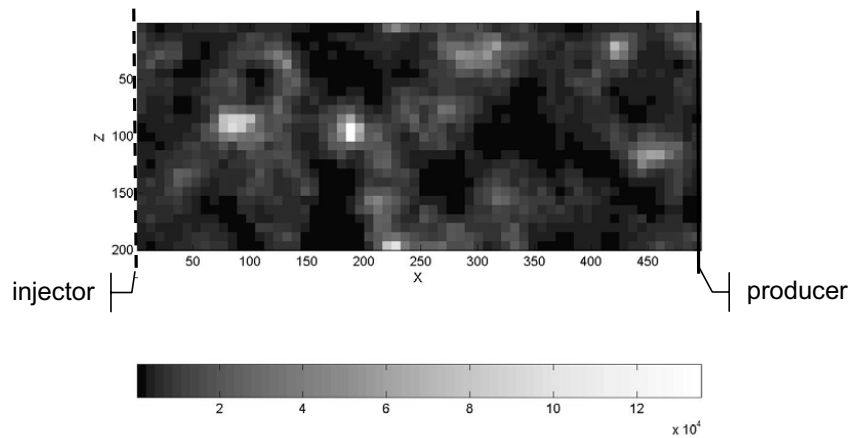
Figure 3-2. Second test case. Permeability field.

The fluid viscosities are based on the data from the SPE fifth comparative project [45].
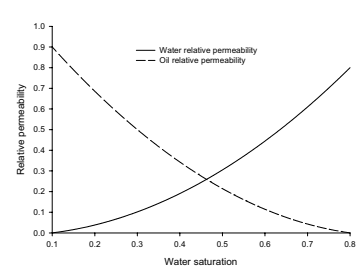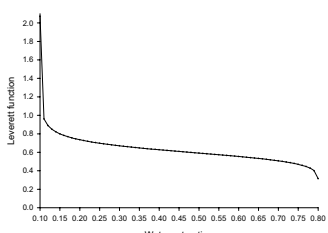
Parameter	Value
Grid	124·50 areal slice; 406.72·3.28·164 m reservoir
Porosity	0.2
Pore volume	43756.56 m^3
Viscosities	Water – 0.25 cP Oil – 0.40 cP
Relative permeabilities	$k_{rw} = k_{rwor}\left(\dfrac{s-s_{wi}}{1-s_{wi}-s_{or}}\right)^2$ $k_{ro} = k_{rowi}\left(1-\dfrac{s-s_{wi}}{1-s_{wi}-s_{or}}\right)^2$ $k_{rwor} = 0.8$ $k_{rowi} = 0.9$ $s_{wi} = 0.1$ $s_{or} = 0.2$
Densities	Water – 1000 kg/m^3 Oil – 1000kg/m^3
Injection rate	43.79 m^3/day (1 pore volume injected in about 1000 days)
$P_{production}$	11.03 MPa
σ	30 mN/m
Capillary pressure	$$J(s) = \alpha\left[\left(\frac{s-s_{min}}{1-s_{max}-s_{min}}\right)^{-1/m}-1\right]^{1/n}-y, \;\; n=\frac{1}{1-m}$$ $\alpha = 0.6$ $m = 0.9$ $y = 0$ $s_{min} = 0.09999$ $s_{max} = 0.801$

Table 3-2. Second test case. Simulation data.

3.1.3. Test case 3

The third test case is the upscaled grid from the 10th SPE reservoir comparative project [24]. The porosity field is presented in Figure 3-3. The permeability varies around 7 orders of magnitude from 0.007 to 3565mD with an average of 53.8mD and is presented in common logarithm scale in Figure 3-4. The simulation data is gathered in Table 3-3.
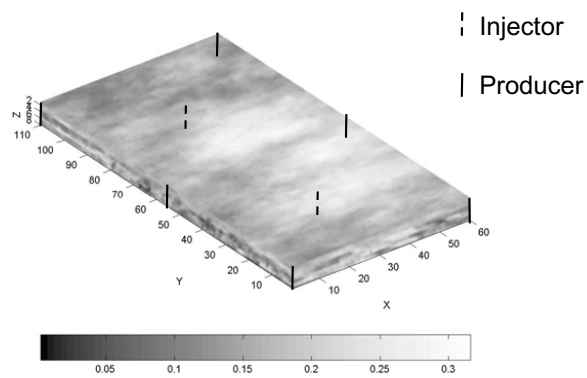
Figure 3-3. The third test case. The porosity field.
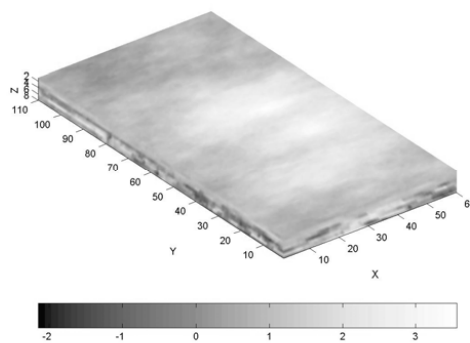
Figure 3-4. Thr third test case. The permeability field in common logarithmic scale.
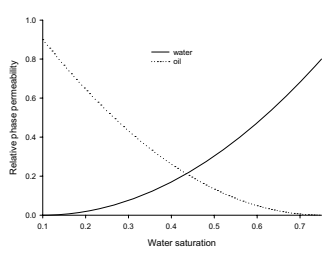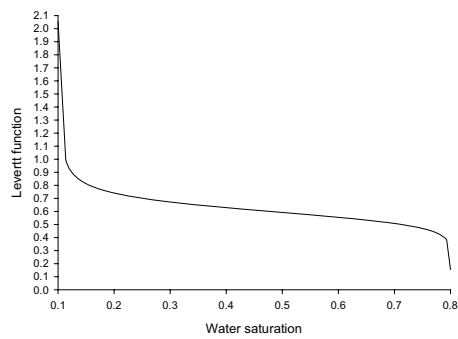
Parameter	Value
Grid	60·100·8; 6.0·6.0·6.5 m grid blocks
Pore volume	2'108'569 m^3
Viscosities	Water – 0.4 cP Oil – 0.25 cP
Relative permeabilities	$k_{rw} = k_{rwor}\left(\dfrac{s - s_{wi}}{1 - s_{wi} - s_{or}}\right)^2$ $k_{ro} = k_{rowi}\left(1 - \dfrac{s - s_{wi}}{1 - s_{wi} - s_{or}}\right)^2$ $k_{rwor} = 0.8$ $k_{rowi} = 0.9$ $s_{wi} = 0.1$ $s_{or} = 0.25$
Densities	Water – 1000 kg/m^3 Oil – 1000 kg/m^3
Injection rate	2 injectors 1084.474 m^3/day each
$P_{production}$	6 producers at 30 MPa BHP
σ	30 mN/m
Capillary pressure	$$J(s) = \alpha\left[\left(\frac{s - s_{min}}{1 - s_{max} - s_{min}}\right)^{-1/m} - 1\right]^{1/n} - y, \quad n = \frac{1}{1 - m}$$ $\alpha = 0.6$ $m = 0.9$ $y = 0.017$ $s_{min} = 0.0999$ $s_{max} = 0.800001$

Table 3-3. Third test case. Simulation data.

The 6 decimals in the s_{max} value are necessary to reproduce the Leverett function curve as show in Table 3-3. The end points of the Leverett function are

extremely sensitive to these values due to the asymptotic behavior of the van Genuchten model [77]. For example, at a water saturation of 0.8 the Leverett function has the value of 0.141 when s_{max} equal to 0.800001. If the s_{max} is changed to 0.801, the Leverett function at $s_w=0.8$ increases by more than a factor of two to the value of 0.297.

3.2. Estimation of the displacement regime

The governing equations (2.24) and (2.25) may be transformed to a dimensionless form. For this purpose a set of the dimensionless groups is introduced. Using these groups the relative magnitude of the capillary, gravity and viscous forces may be determined. The approach of making the equations dimensionless is given by, for example, Bedrikovetsky [9] and Zhou et al. [80] and is in general similar. However, the details may differ and as a result several sets of the dimensionless groups are derived. These groups may be applied for two different purposes:

- Estimate the displacement regime to choose the optimum simulation tools and simulation options;
- Estimate if the simulation results do make sense from the point of view of the physics of the fluid flow in porous media.

The estimation of the displacement regime is carried out using two groups of the dimensionless parameters. The first set is presented by Bedrikovetsky [9]. The dimensionless parameters include the capillary-viscous ratio:

$$\varepsilon_1 = \frac{\sigma k_{rowi} \cos\theta \sqrt{k_{av}/\phi_{av}}}{U\mu_0 L} \, ,$$

(3.1)

The anisotropy ratio:

$$\varepsilon_2 = \frac{H^2 k_x}{L^2 k_z} \, ,$$

(3.2)

and the capillary-gravity ratio:

$$\varepsilon_3 = \frac{(\rho_w - \rho_o)gH}{\sigma \cos\theta \sqrt{\phi_{av}/k_{av}}}.$$ (3.3)

Here k_{rowi} is the end point oil relative permeability, index i represents the average properties, L is the characteristic length, U is the linear velocity, k_{av} is the average field permeability, ϕ_{av} is the average field porosity.

The displacement regimes are classified according to Table 3-4.

Dimensionless parameters	Displacement regime
$\varepsilon_1 \cdot \varepsilon_2^{-1} < 1;\ \varepsilon_3 < 1$	Viscous Dominant
$\varepsilon_1 \cdot \varepsilon_2^{-1} > 1;\ \varepsilon_3 \approx 1$	Vertical Equilibrium
$\varepsilon_1 \cdot \varepsilon_2^{-1} > 1;\ \varepsilon_3 < 1$	Capillary Dominant
$\varepsilon_1 \cdot \varepsilon_2^{-1} > 1;\ \varepsilon_3 > 1$	Gravity Dominant
$\varepsilon_2 < 1$	Commingled Layers

Table 3-4. Determination of the displacement regimes by means of Bedrikovetsky dimensionless groups.

Zhou et al. [80] derived different set of dimensionless parameters.

The gravity to viscous ratio is estimated as:

$$N_{gv} = \frac{\Delta\rho g L k_{av}}{Hq\mu_o},$$ (3.4)

The capillary to viscous ratio as:

$$N_{cv} = \frac{LP_c^* k_{av}}{H^2 q\mu_o},$$ (3.5)

here q is the flow rate, P_c^* is the characteristic transverse capillary pressure of the medium:

$$P_c^* = \int_{s_{wi}}^{1-s_{or}} \frac{P_c(s_w)}{1 - s_{or} - s_{wi}}\,ds,$$ (3.6)

here s_w is the water saturation, s_{or} is the residual oil saturation and s_{wi} is the initial water saturation.

Introducing the capillary pressure, equation (1.17) into equation (3.6):

$$P_c^* = \int_{s_{wi}}^{1-s_{or}} \frac{\frac{\sigma \cos\theta}{\sqrt{k/\phi}} J(s_w)}{1 - s_{or} - s_{wi}} ds,$$ (3.7)

and regrouping the variables:

$$P_c^* = \frac{\sigma \cos\theta}{\sqrt{k/\phi}(1 - s_{or} - s_{wi})} \int_{s_{wi}}^{1-s_{or}} J(s_w) ds.$$ (3.8)

The mobility ratio is introduced as:

$$M = \frac{\lambda_w}{\lambda_o},$$ (3.9)

and the shape factor as:

$$R_l^2 = \frac{L^2 k_z}{H^2 k_x}.$$ (3.10)

The displacement regime may be determined using Table 3-5.

Dimensionless parameters	Displacement regime
$\dfrac{(N_{gv} + N_{cv})M}{1+M} \ll 1.0$	Viscous Dominant
$\dfrac{(N_{gv} + N_{cv})M}{1+M} \ll 1.0;\ R_l^2 > 1.0$	Vertical Equilibrium
$N_{gv} \ll N_{cv};\ \dfrac{MN_{cv}}{1+M} \gg 1.0$	Capillary Dominant
$N_{gv} \gg N_{cv};\ \dfrac{MN_{gv}}{1+M} \gg 1.0$	Gravity Dominant
$N_{gv} \approx N_{cv};\ \dfrac{MN_{cv}}{1+M} \gg 1.0$	Capillary-Gravity Equilibrium
$\dfrac{(N_{gv} + N_{cv})M}{1+M} \ll 1.0;\ R_l^2 \ll 1.0$	Commingled Layers

Table 3-5. Determination of the displacement regimes by means of Zhou et al. dimensionless groups.

3.3. Comparison of the pressure equation modifications

First the CVP and the SFD methods of accounting for capillary effects in the pressure equation are compared on the test case 1 without the saturation equation modification and without any kind of automatic time step selection routine. The effects of the grid refinement and the number of time steps on the simulation time and the material balance error of both methods are investigated. Later the CVP and the CFD methods are compared with inclusion of the capillary effects in the saturation equation.

Three different grid sizes are used in this test:

- The coarse grid comprised of 20·4 grid blocks. Each checker block is represented by just one block;
- The medium size grid comprised of 100·20 grid blocks. Each checker block is represented by 5 blocks in each direction (25 in total);
- The fine scale grid comprised of 500·100 grid blocks. Each checker block is represented by 25 blocks in each direction (625 in total).

Each run simulates 800 days or 2 PV of water injection using 20 time steps. The comparison is performed based on the oil production curves and the displacement profiles, that is to say on the production history.

The comparison of the CPU time and the maximum mass balance error is performed for the following runs: 1) neglecting capillary effects; 2) using the SFD method of introduction of capillary effects into the pressure equation; 3) using the CVP method. The SFD and the CVP simulation runs are performed neglecting the capillary effects in the saturation equation.

The methods of both Bedrikovetsky and Zhou et al. indicate the capillary dominated displacement, as shown in Table 3-6.

Dimensionless parameters		Value
Bedrikovetsky	$\varepsilon_1 \cdot \varepsilon_2^{-1}$	34.78
	ε_3	0
	Displacement regime	Capillary Dominant
	$MN_{cv}/(1+M)$	1.63
Zhou et al.	N_{gv}	0
	N_{cv}	3.27
	Displacement regime	Capillary Dominant

Table 3-6. Determination of the displacement regimes. Checkerboard case.

The simulation without capillary effects is tested first. The oil production curves for three different grids are shown in Figure 3-5.
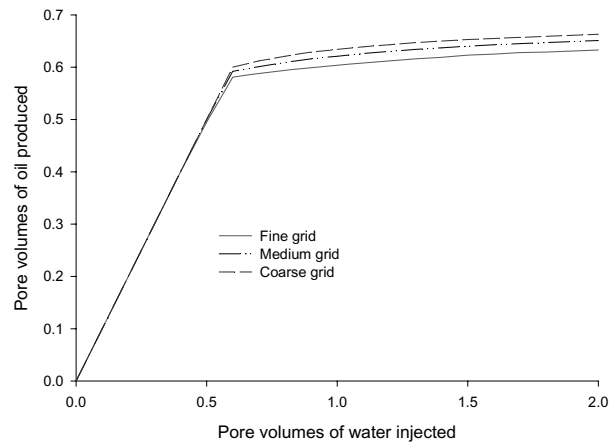
Figure 3-5. The checker board case. Oil production for the simulation without capillary effects on different simulation grids.

The oil production curves show the volume of oil produced as a function of the volume of water injected. For the immiscible incompressible case before the breakthrough the volume of oil produced is equal to the volume of water injected, indicated by the straight line on Figure 3-5. However, after the breakthrough the production well produces the water-oil mixture, rather than just

oil. The total amount of the produced fluid is equal to the volume of water injected; however, the fraction of the oil in the produced fluid is smaller than one. The inflection point of the oil production curve corresponds to the breakthrough time.

Higher total oil production on the coarse grid may be explained by higher sweep efficiency, or the area covered by water. Higher sweep efficiency also results in delayed breakthrough in terms of pore volumes of water injected.
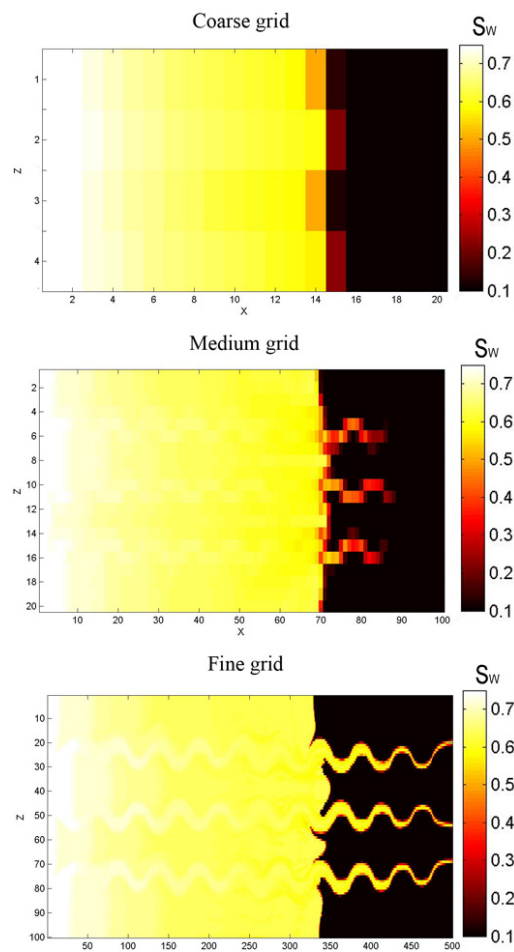
Figure 3-6. The checkerboard case. Displacement profiles without capillary effects after 0.4PVI.

In the fine grid simulation it is possible to observe the fingering of water inside the water saturated region (white fingers inside the yellow region in Figure 3-6). In retrospect the fingers inside the water saturated zone are practically invisible in the medium grid – the fingering of water is only indicated in the oil saturated media (yellow fingers inside the black region in Figure 3-6). In the coarse grid the fingering is captured only by the difference in the saturation of the neighboring blocks around the saturation front.

The difference in the breakthrough time is due to the fingering of the water through the high permeable checkers. The coarse model fails to capture these effects, as shown in Figure 3-6.

The oil production curves for the simulations using the CVP and the SFD methods are shown in Figure 3-7. The oil production curves are shown starting from 0.5 PVI to highlight the difference in the oil production curves after the breakthrough.
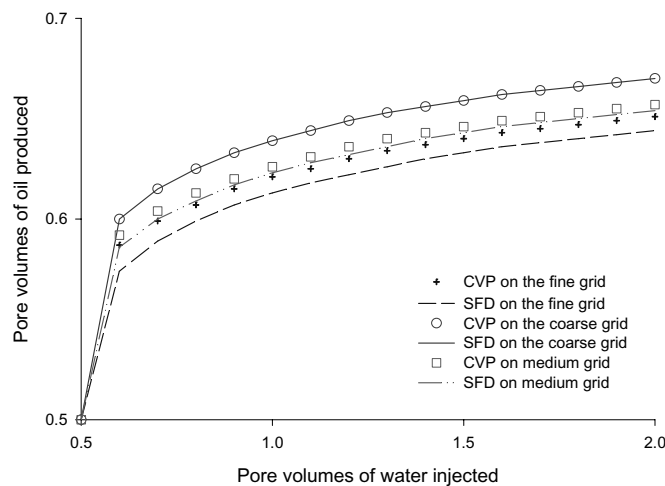
Figure 3-7. The checkerboard case. Oil production for the simulation on different grids sizes with capillary effects introduced only in the pressure equation.

The CVP modification method shows a small difference in the oil production curves on the medium and the fine grids compared to the SFD method. Behavior of the oil production curves simulated using the SFD modification is similar to simulation without capillary effects.

Introduction of capillary effects into the pressure equation only is not sufficient to completely remove the fingering of water; however, the water saturation in the fingers decreases, as shown in Figure 3-8. The SFD method pulls back the fingers to a larger extent, comparing to the CVP method. However, the SFD method shows more numerical problems in the water saturated zone.
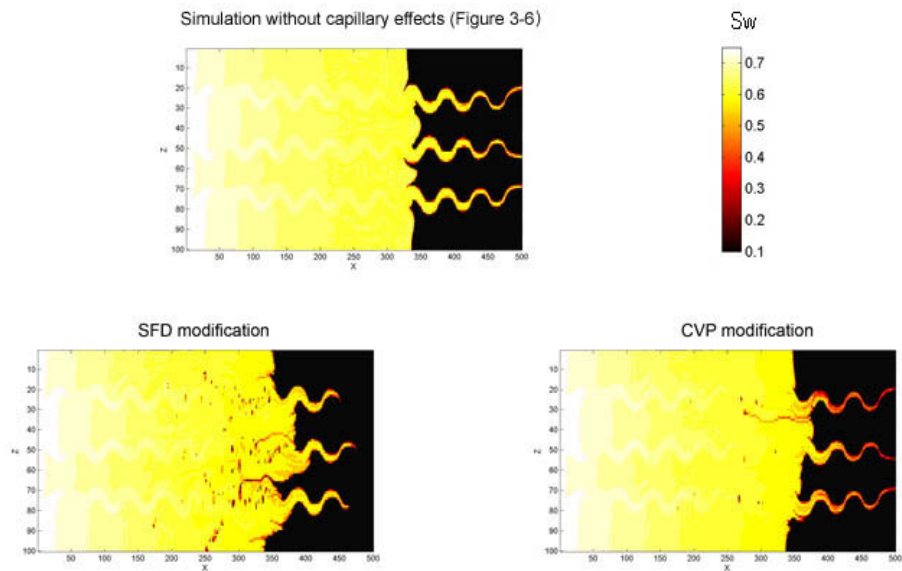
Figure 3-8. The checkerboard case. Displacement profiles at 0.4 PVI.

All simulations show increase of the CPU time required with increase of the grid size. The CVP method is the fastest on all the three grids. The simulation times versus the grid size are plotted in Figure 3-9. Speed ups of the simulation time with the CVP method compared to the simulation without capillary effects and the SFD method may be due to the reformulation of the pressure equation. The

solution in terms of the CVP is more uniform, resulting in faster convergence of the numerical solver.

The maximum material balance error decreases as a function of grid size. The positive mass balance error corresponds to amount of water injected being larger compared to the amount of water produced and an amount of water increased in the reservoir. The material balance error on the coarse grid may be explained by the averaging of the fluid properties in the large blocks. The material balance error on the fine scale grid may be associated with the large time steps. Simulations on all three grids are performed using 20 time steps. However, due to the scheme stability considerations larger number of time steps may be required for simulations on the finer grids. Moreover, as it is shown in Figure 3-8 both the CVP and the SFD methods show some numerical instabilities in the saturation values behind the water front.
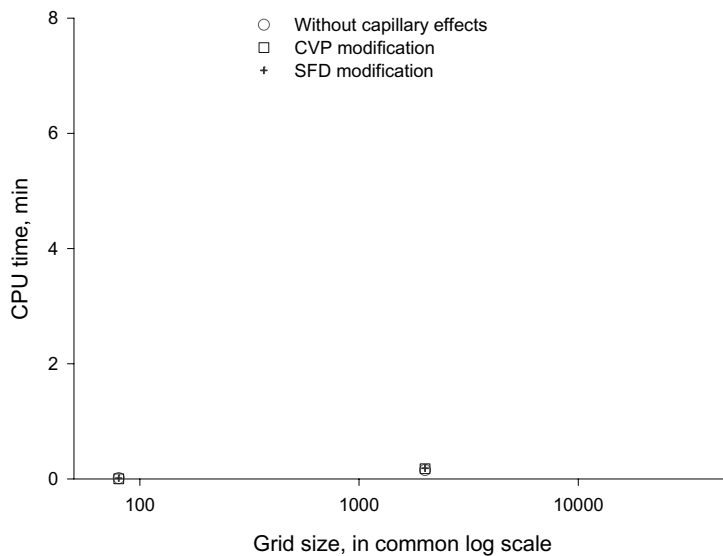
Figure 3-9. The checkerboard case. CPU time for various grid sizes.

The absolute value of the final mass balance error of the CVP method is comparable to the simulation without capillary effects, however, the SFD

modification results in higher, in absolute values, mass balance error, as shown in Figure 3-10.
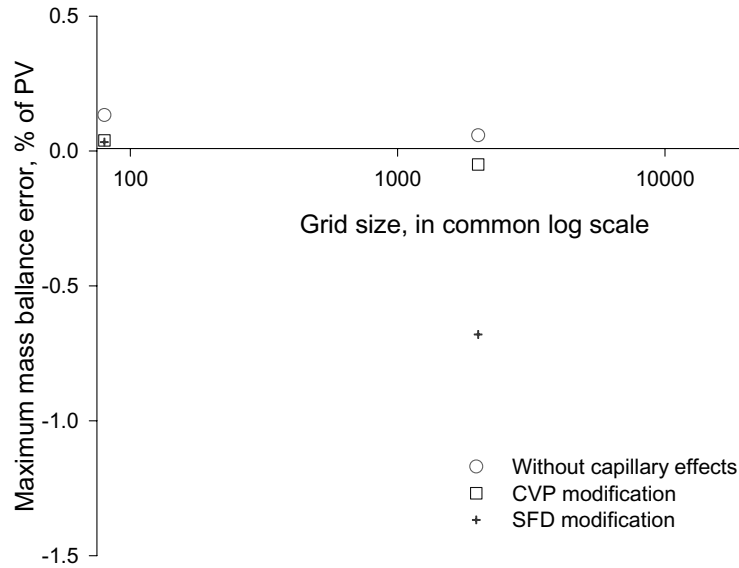
Figure 3-10. The checkerboard case. Maximum mass balance error for various grid sizes.

Since the medium grid captures the main features of the flow and the simulation times are significantly shorter comparing to the fine grid, the influence of the number of time steps is investigated on the medium grid.

Influence of the number of time steps on the total CPU time requirement is rather small, as shown in Figure 3-11.
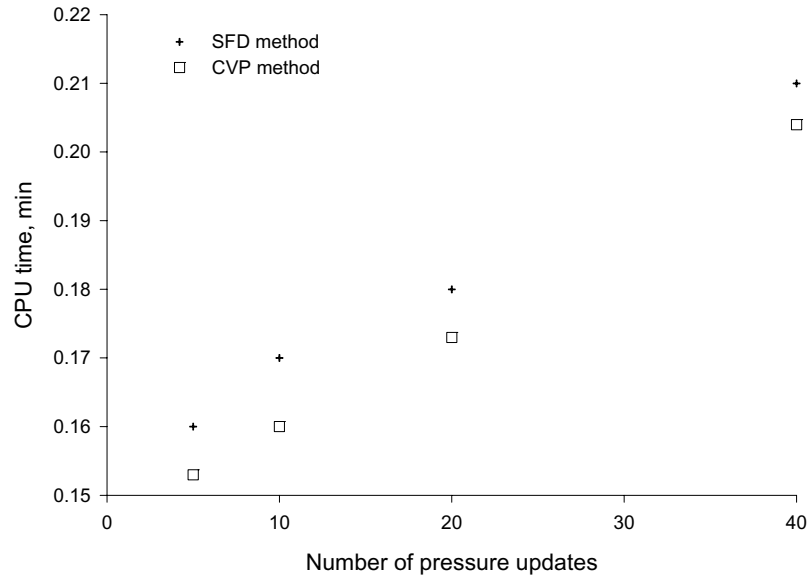
Figure 3-11. The checkerboard case. CPU time for various number of pressure updates.

When the number of time steps increases 8 times (from 5 to 40), the CPU time only increases about 35%.

Tracing the streamlines with respect to the capillary pressure should lift up the restriction on the time step size associated with the capillary non-linearities in the similar way as it does for the non-linearities associated with mobilities, see Section 2.2.7. Therefore the CPU time may be restricted only by the numerical solver. The pressure solutions for the small time step sizes converge faster, compensating for the larger number of the solutions required.

The material balance error does not show any significant dependency on the time step size. It decreases in absolute value for the SFD modification method, however, the CVP method shows smaller mass balance error for any number of time steps taken, as shown in Figure 3-12.
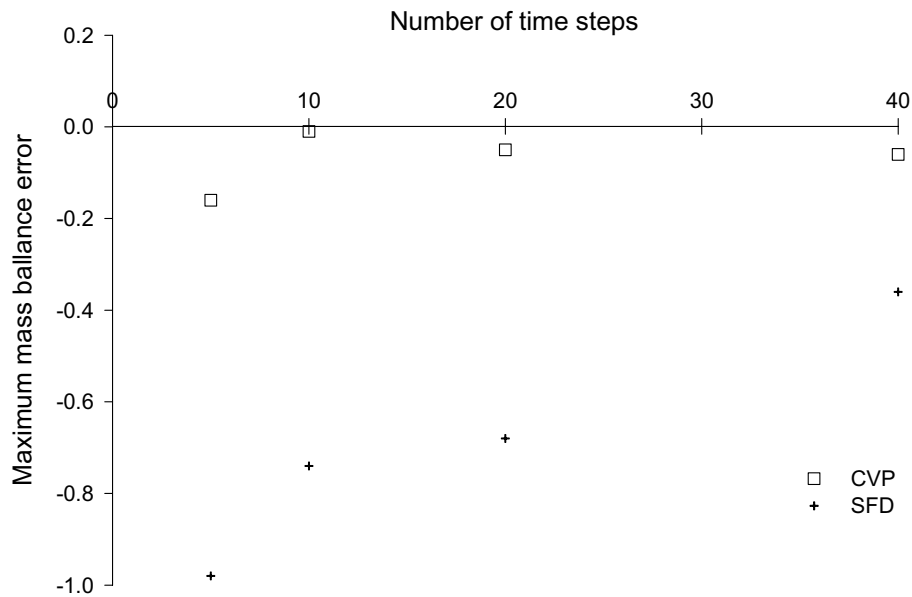
Figure 3-12. The checkerboard case. Maximum mass balance error for various number of time steps.

The number of time steps has quite a pronounced effect on the oil production curves. It may be concluded from Figure 3-13 that 20 time steps provide sufficient quality of the solution.

The oil production curves, starting from 0.5PVI for different numbers of time steps are shown in Figure 3-13.

Based on the simulations presented above, it may be concluded that the CVP method delivers smaller mass balance error. However, both modification methods should be further compared with full account for capillary effects.
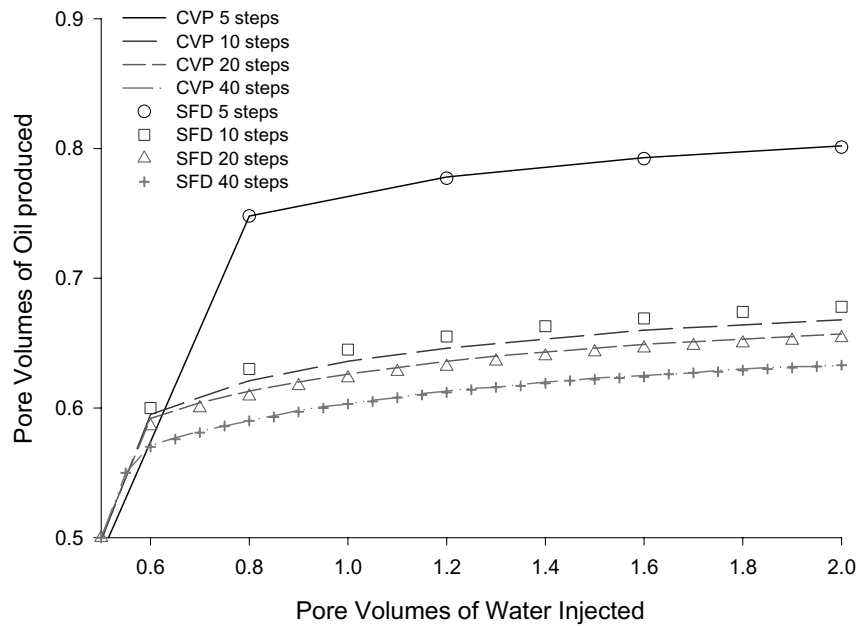
Figure 3-13. The checkerboard case. Oil production curves for the simulations using different number of time steps, with capillary effects introduced only in the pressure equation.

The simulation accounting for capillary effects both in the pressure and the saturation equations is performed using 20 time steps. Harmonic averaging of the transmissibilities in the saturation corrector step is used. Comparison of the saturation fronts obtained with the CVP and the SFD methods after 0.3 and 0.5 PVI are presented in Figures 3-14 and 3-15.
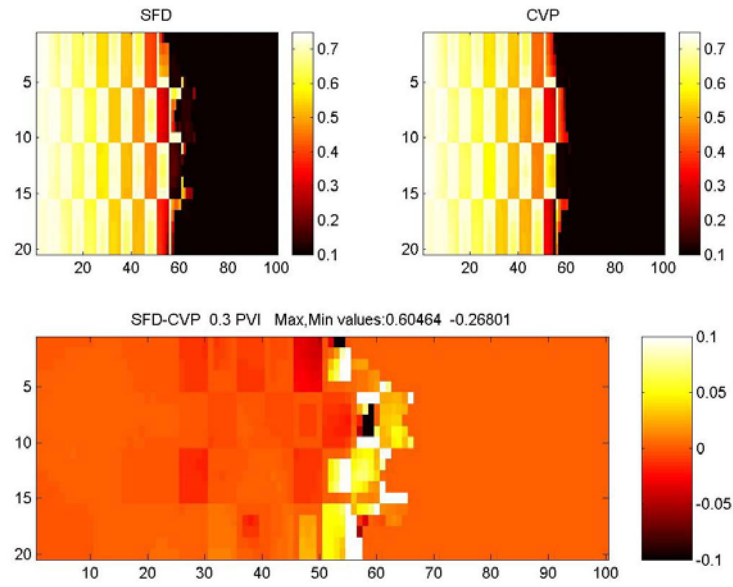
Figure 3-14. The checkerboard case. Comparison of the pressure equation modifications. Saturation plots after 0.3 PVI.
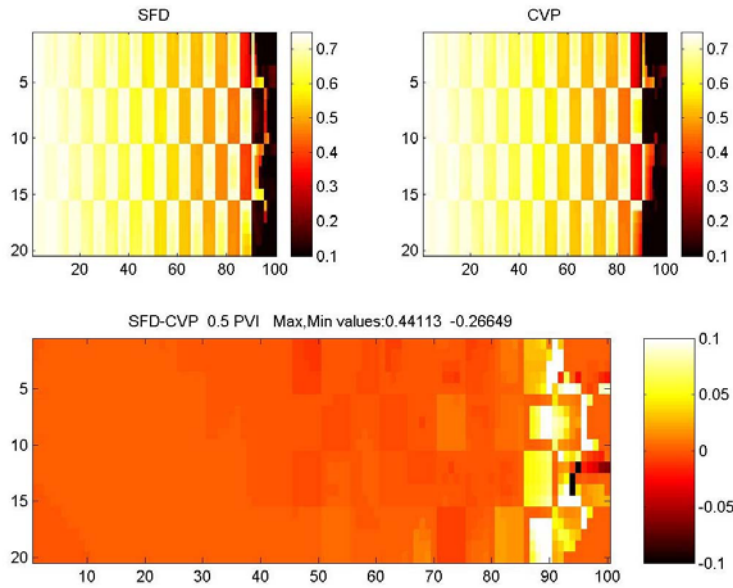
Figure 3-15. The checkerboard case. Comparison of the pressure equation modifications. Saturation plots after 0.5 PVI.

The CPU time and the maximum mass balance error are shown in Table 3-7. It may be noticed that the mass balance error is lower for the simulations accounting for capillary effects both in the pressure and the saturation equations compared to the simulations accounting for capillary effects only in the pressure equation. This may be coincidental, rather than a general fact.

	SFD	CVP
CPU time, min	0.30	0.28
Mass balance error, %PV	-0.60	-0.02

Table 3-7. The checkerboard case. Comparison of the pressure equation modifications. The simulation time and the mass balance error.

In this test the CVP method is faster and results in smaller mass balance error. An attempt was carried out to compare speed of the SFD and the CVP methods at approximately the same level of accuracy. The SFD method was restricted to the 0.1% maximum mass balance error. However, it was not possible to complete the simulation run. The time step size very quickly decreased to the minimum allowed value of several minutes, but the mass balance error remained larger than 0.1%. Small time steps resulted in a large number of mappings from the finite-difference grid to the streamlines and back. As a result the numerical error associated with re-mapping exceeded 0.1%. Moreover the CVP modification method shows less instabilities in the saturation values comparing to the SFD method.

The numerical instabilities disappear after the breakthrough in case of applying the SFD or the CVP methods as shown in Figure 3-16 for the saturation profiles after 1.0 PVI.

SFD   CVP
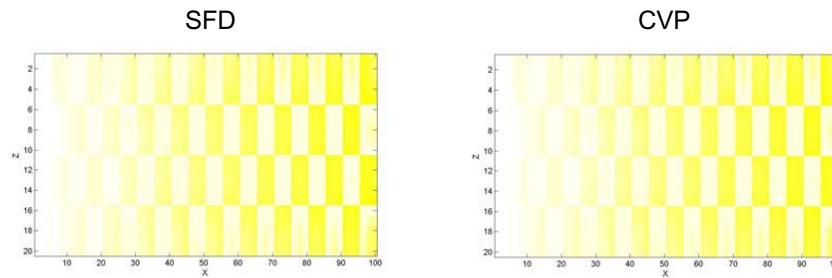
Figure 3-16. The checker board case. Comparison of the pressure equation

modifications. Saturation plots after 1.0 PVI

The simulations with capillary effects accounted for in the saturation equation confirm the advantages of the CVP method, namely the smaller numerical error and the faster solutions. Comparisons of the harmonic averaging of the transmissibilities and the arithmetic averaging of the saturation during the transmissibility evaluations in the corrector step are going to be performed based on the CVP pressure modification scheme.

3.4. Comparison of the saturation equation modifications

As it is shown in the previous section, the saturation equation using the harmonic averaging of the capillary transmissibilities may results in unstable saturation values. The same simulation (800 days or 2 PV of water injection using 20 time steps) is repeated with the average saturation method. The difference in the saturation profiles obtained using the harmonic averaging and the average saturation methods is quite pronounced. The saturation plots after 0.3 and 0.5 PVI are shown in Figures 3-17 and 3-18.

Harmonic average
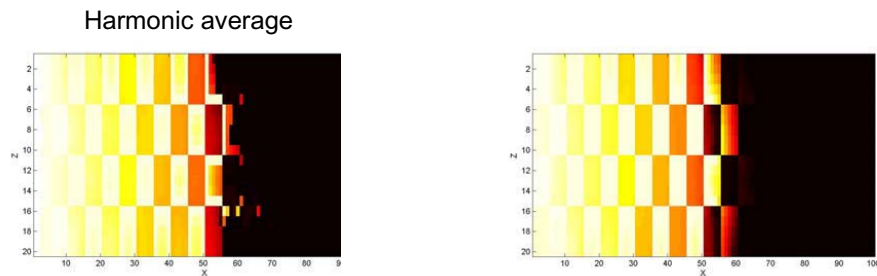
Figure 3-17. The checkerboard case. Comparison of the saturation equation modifications. Saturation plots after 0.3 PVI.

Harmonic average   Average saturation
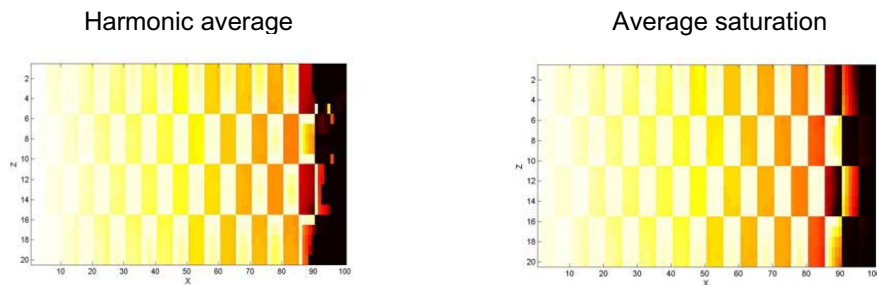
Figure 3-18. The checker board case. Comparison of the saturation equation modifications. Saturation plots after 0.5 PVI.

Comparisons of the CPU times and the mass balance errors are presented in Table 3-8.

	Harmonic average	**Average saturation**
CPU time, min	0.28	0.25
Mass balance error, %PV	-0.02	-0.006

Table 3-8. The checkerboard case. Comparison of the saturation equation modifications. The simulation time and the mass balance error.

The displacement profile looks more stable for the simulation using the average saturation method. The results obtained using the average saturation are

compared to the Eclipse 100. The Eclipse 100 simulations are performed in the IMPES mode. The IMPES mode is selected to minimize the numerical dispersion associated with the finite difference solution. The displacement profiles after 0.3 and 0.5 PVI are compared to the Eclipse 100 are shown in Figures 3-19 and 3-20. There are few pronounced differences between the Eclipse and the CapSL for this simulation case. The Eclipse predicts stronger end-effects between the high and the low permeable checker blocks and slower propagation of water inside the low permeable checkers. The low permeable checker blocks in the Eclipse simulation can be easily identified in Figures 3-19 and 3-20. The water saturation in the boundary layer of the preceding (in the direction of the flow) high permeable checker-block is rather low. On the other hand, the water saturation in the boundary low permeable grid blocks facing the next high permeable checker-block is high. Both these effects are due to the capillary end-effects, discussed later in this chapter.
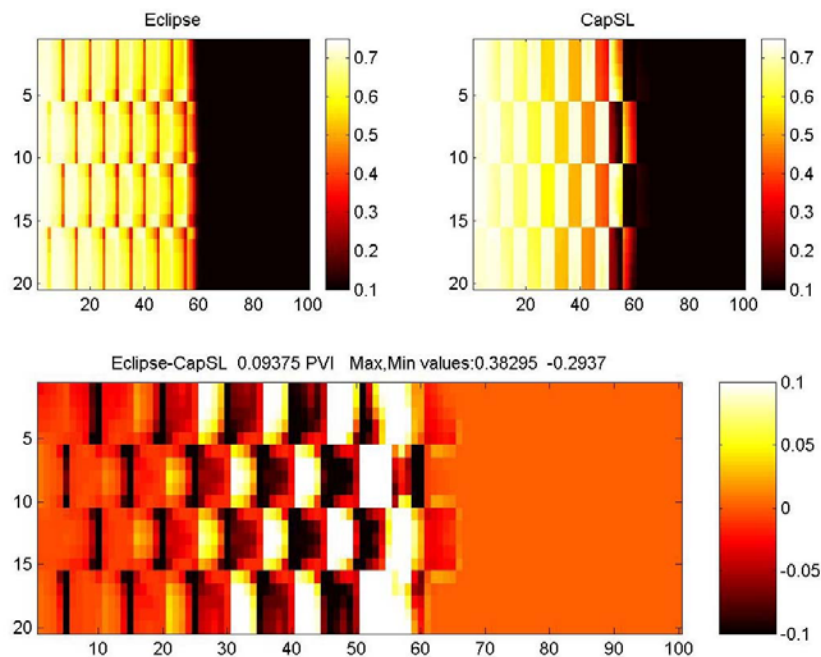
Figure 3-19.The checkerboard case. Comparison of the Eclipse and the CapSL saturation plots after 0.3 PVI.
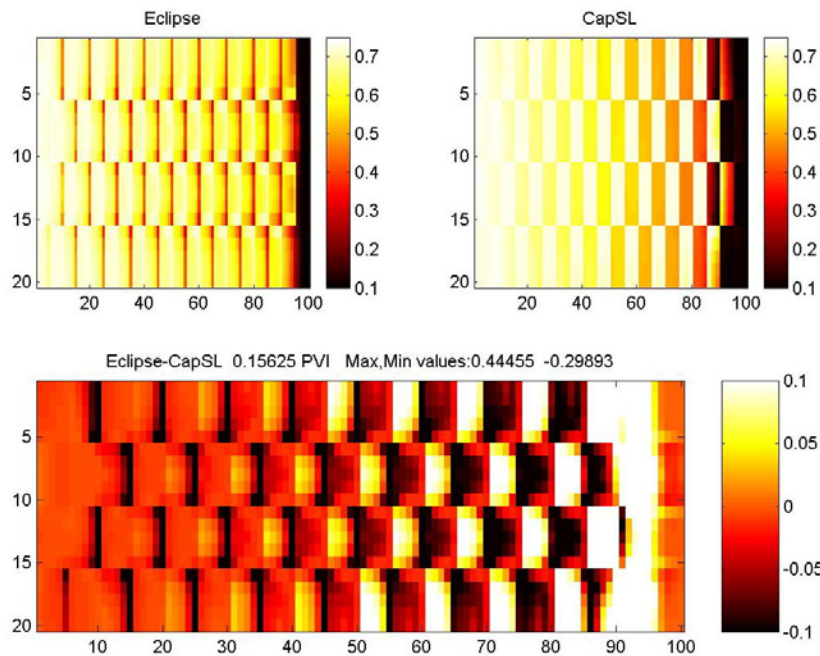
Figure 3-20. The checkerboard case. Comparison of the Eclipse and the CapSL
saturation plots after 0.5 PVI.

Low permeable checker-blocks in the CapSL simulation have uniformly high saturation, comparing to the uniformly low saturation in the high permeable checker blocks. Moreover, the CapSL predicts that penetration of the water into the next vertical column of the checker blocks starts diagonally between the low permeable checker blocks in the neighboring columns. The high permeable checker blocks are swept at a later time. The Eclipse predicts that the low permeable checker blocks have a higher water content comparing to the high permeable ones, however, the water penetrates into all the checker blocks in the vertical column at the same time. This difference might be due to several reasons. First of all, the Eclipse 100 performed 4555 time steps. Streamline simulation was completed with 20 time steps. Due to the higher number of the time steps and the nature of the finite difference method the Eclipse solution is more affected by the numerical diffusion. Secondly, the Eclipse solves the saturation equation in one step on the finite difference grid, while the CapSL uses the operator splitting method. Therefore the streamline simulation is

affected by the operator splitting error. Finally, the flow paths of the two simulators are different. The flow path in the block-centered finite-difference simulation is represented by the set of the straight lines connecting the block centers. The streamline flow path is much more realistic, as sketched in Figure 3-21
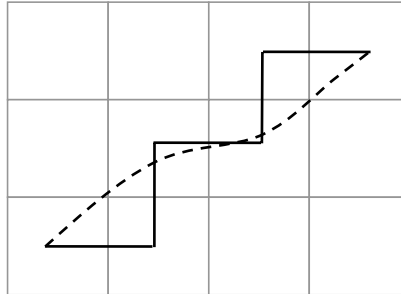
Figure 3-21. The difference of the flow paths between finite-difference (solid line) and streamline (dashed line) methods.

In general as a result of more realistic flow path and smaller numerical dispersion the streamline simulation provide better prediction quality. However, the operator splitting error may be rather large for the large time steps. The comparison of the CapSL and the Eclipse results is performed using the automatic time step selection routine, as shown in the next section.

3.5. Comparison of the time step selection routines

The stability condition for the finite-difference IMPES methods demands that the saturation front does not propagate by more than one grid block per single time step. Therefore, increasing the number of grid blocks by a factor of two requires decreasing the time step size by a factor of two as well, leading to the second order dependency of the simulation time from the grid size. For the streamline

methods, however, the dependence is less straightforward, as discussed in Section 2.2.7.

Comparison of the various time step routines is performed using the optimal choice of the methods of accounting for capillary effects in the pressure and the saturation equations – the CVP method and the average saturation method.

As it is was shown previously, the stable solution for the test case 1 with the capillary effects is obtained using 20 time steps. However, the difference between the Eclipse and the CapSL predictions is quite pronounced. The CapSL predicts a faster front propagation, and a higher sweep of the low permeable checker blocks, as shown in Figures 3-19 and 3-20.

The automatic time step routine presented in the Section 2.2.7, is applied. The saturation profiles obtained using the automatic time step routine are compared to the profiles obtained using 20 time steps in Figure 3-22. Comparison with the Eclipse is shown in Figure 3-23. The comparisons of the CPU time and the mass balance error are presented in Table 3-9.

	20 time steps	Automatic time steps
CPU time, sec	15	24 (138 time steps)
Mass balance error, %PV	-0.006	-0.5

Table 3-9. The checkerboard case. Comparison of the time step routines. The simulation time and the mass balance error.

The mass balance error for the simulation utilizing the automatic time step routine is larger compared to the simulation using 20 time steps. Increase of the mass balance error means that increase of the mapping error overcomes the decrease of the operator splitting error.

0.3PVI

20 steps   Automatic steps

0.5PVI

20 steps   Automatic steps
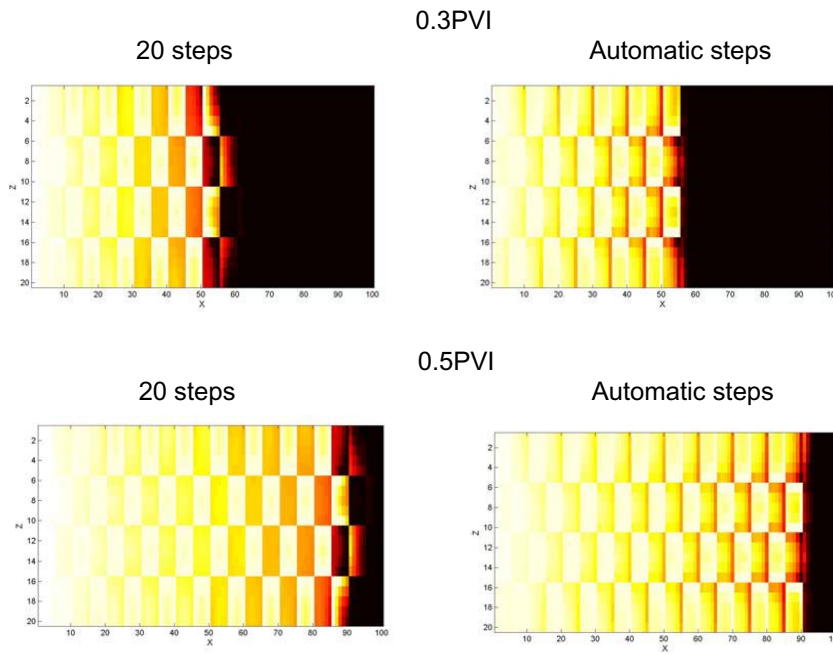
Figure 3-22. The checkerboard case. Comparison of the time step selection routines.
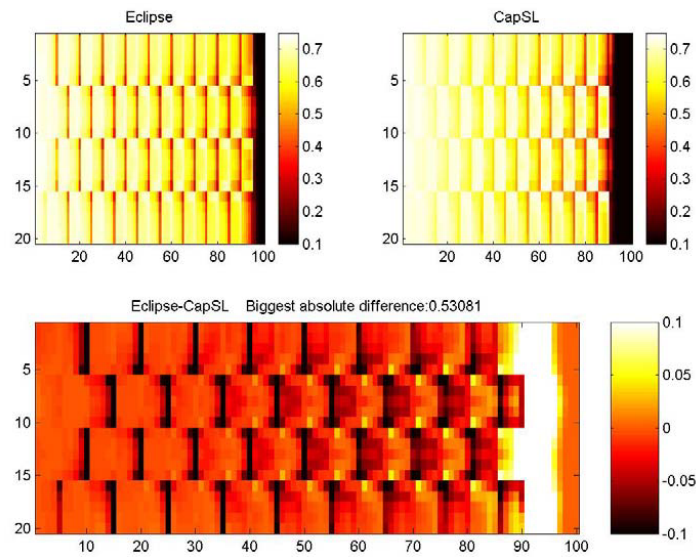
Figure 3-23. The checkerboard case. Comparison of the Eclipse and the CapSL(using automatic time steps) saturation plots after 0.5 PVI.

With automatic time step selection the predictions are much closer to the ones obtained with the Eclipse 100. The saturation front in the Eclipse simulation still propagates faster, however the difference in the saturation in the swept area is much smaller. Better match with the Eclipse 100 simulation results, see Figures 3-20 and 3-23, may partially be a consequence of a higher numerical smearing of the front in the CapSL as a result of a larger number of the time steps. On the other hand, during the single time step the fluid mobilities are calculated explicitly as functions of the saturation on the previous time step. As a result, smaller time steps taken by the CapSL allow for more frequent update of the fluid mobilities and may result in a better prediction of the cross flow.

Another automatic time step selection method is based on performing several saturation steps per each time step. In this method several consequent solution steps of the saturation equation along the streamlines and on the finite-difference grid are performed for each pressure solution step, see Section 2.2.7. Comparisons of the saturation fronts using different automatic time step selection routines after 0.3 and 0.5 PVI are shown in Figures 3-24 and 3-25.

Comparisons of the CPU time and the mass balance error are presented in Table 3-10.

<div align="center">Automatic steps   Saturation update steps</div>
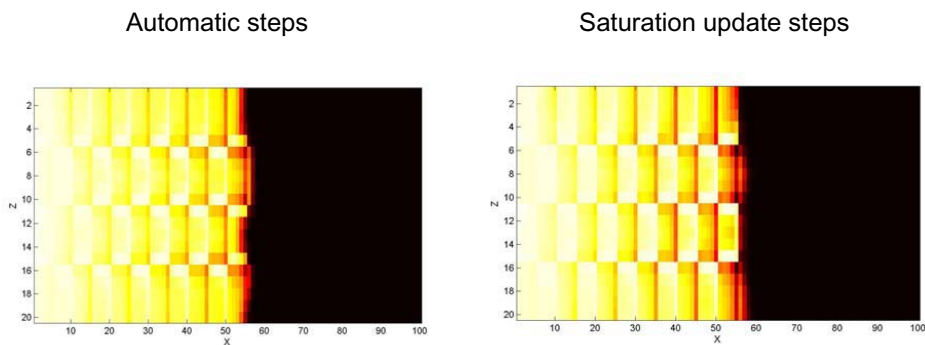
Figure 3-24. The checkerboard case. Comparison of the automatic time step and saturation step selection. Saturation plots after 0.3 PVI.

Automatic steps   Saturation update steps
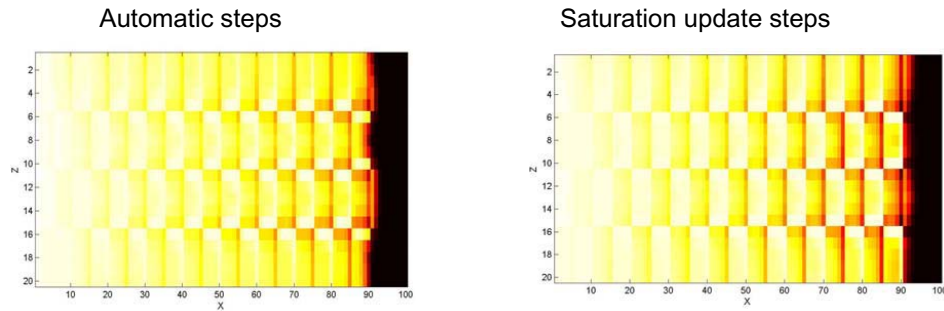
Figure 3-25. The checkerboard case. Comparison of the automatic time step and saturation step selection. Saturation plots after 0.5 PVI.

	Automatic time steps	Automatic saturation time steps
CPU time, min	0.41 (138 time steps)	1.1 (1010 saturation steps)
Mass balance error, %PV	-0.5	0.26

Table 3-10. The checkerboard case. Comparison of the time step and the saturation step selection routines. The simulation time and the mass balance error.

The automatic saturation step routine results in the slower run since it uses the most restricted time step selection. It is possible that such a restriction is not necessary for the streamline simulation, but the detailed research of the time step selection routine is not included in this thesis.

The simulation using both automatic time step selection and automatic selection of the saturation steps finished in 1.3 minutes, after 131 time steps and 1180 saturation steps, being the slowest streamline simulation run for the given test

case. The mass balance error is -0.09%. The comparison of the saturation profiles with the Eclipse is presented in Figures 3-26 and 3-27.

A faster propagation of the displacement front predicted by the Eclipse compared to the CapSL is due to the combination of the following factors: 1) The difference in the flow paths, see Figure 3-21; 2) The difference in the saturation equation solutions; 3) Numerical dispersion of the finite-difference solution in Eclipse.

Comparison of the CPU times and the mass balance errors using the CapSL with fully automatic time step selection and the Eclipse 100 is presented in Table 3-11.
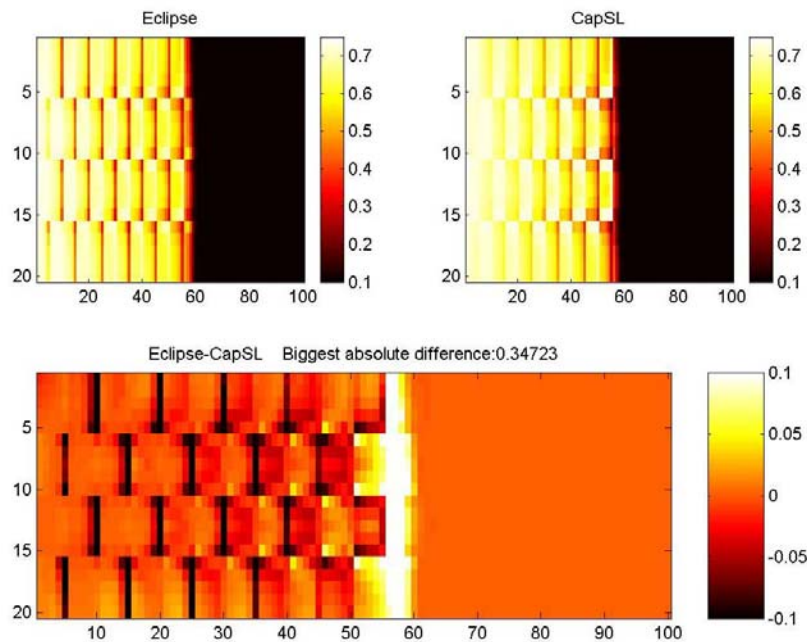
Figure 3-26. The checkerboard case. Comparison of the Eclipse and the CapSL (fully automatic steps) saturation plots after 0.3 PVI.
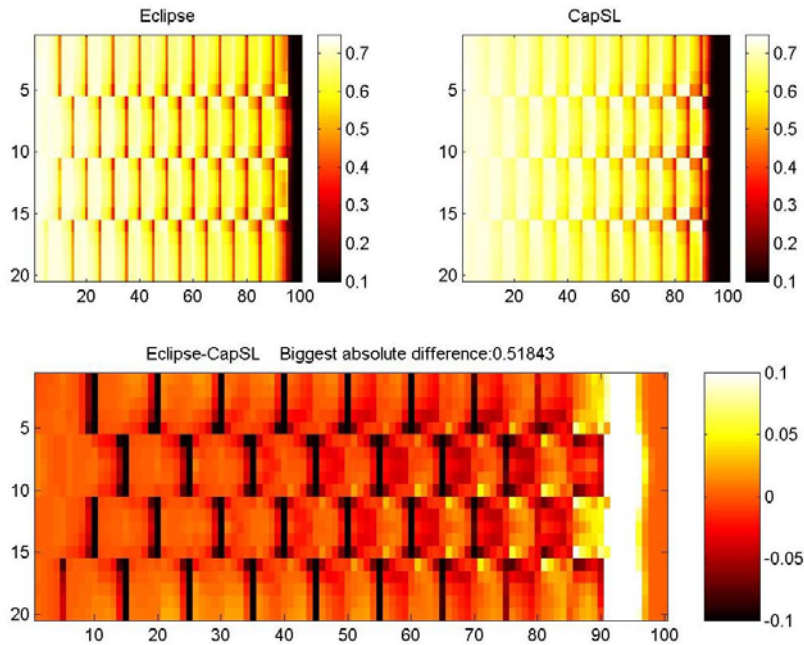
Figure 3-27. The checkerboard case. Comparison of the Eclipse and the CapSL
(fully automatic steps) saturation plots after 0.5 PVI.

	Fully automatic steps	**Eclipse**
CPU time, min	1.3 (1180 saturation steps,131 time steps)	1.4 (4556 steps)
Mass balance error, %PV	-0.09	0.06

Table 3-11. The checkerboard case. Comparison of the Eclipse and the
CapSL(fully automatic steps). *The simulation time and the mass balance error.*

Comparison of the oil production curves is presented in Figure 3-28. As a result of faster propagation of the displacement front and lower local sweep efficiency the Eclipse predicts faster breakthrough and slightly lower oil production. However, the oil production curves have the same trend and are generally close to each other.
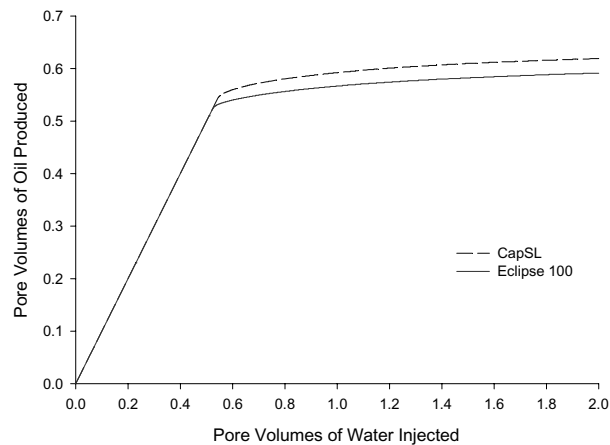
Figure 3-28. The checkerboard case. Comparison of the Eclipse and the CapSL(fully automatic steps). Oil production curves.

Based on the results presented above it may be concluded that the simulation with fully automatic time step selection delivers the best match with the Eclipse 100 simulations. The mass balance error for the simulation with fully automatic time step selection is comparable to the simulation using 20 time steps. However, the CapSL simulation with automatic time step selection results in the simulation times comparable to the Eclipse.

For the sake of the simulation speed one may use manual steps with restricted maximum mass balance error. In case of the fluctuations in the saturation values or a large number of rejected steps the automatic time step selection routine may be applied.

3.6. Simulation of the two-dimensional heterogeneous case

First, the simulation of the test case 2 is performed neglecting capillary effects to estimate the difference between the simulators in the numerical smearing of

the saturation front. The saturation plots are compared in Figures 3-29 and 3-30 after 0.25 and 0.5 PVI.

Figure 3-29. Test case 2. Comparison of the Eclipse and the CapSL saturation plots without capillary effects after 0.25 PVI.

Figure 3-30. Test case 2. Comparison of the Eclipse and the CapSL saturation plots without capillary effects after 0.5 PVI.

The streamline simulation run is carried out in 40 time steps. The Eclipse simulation completed after 886 steps. The Eclipse simulation shows higher numerical smearing, however, match of the simulation results is very good.

The simulation with capillary effects is performed using the interfacial tension value of 30 mN/m. The values of the dimensionless parameters suggested by Bedrikovetsky (Table 3.4) indicate the capillary dominated displacement: $\varepsilon_1/\varepsilon_2 = 8.1$; $\varepsilon_3 = 0$. However, the parameters suggested by Zhou et al. (Table 3.5) show the viscous dominant regime: $M \cdot N_{cv}/(1+M) = 0.6$; $N_{gv} = 0$.

The streamline simulation with capillary forces is carried out by application of the CVP method and the harmonic averaging method. 2000 days or about 2 pore volumes of water injected are simulated in 40 time steps. Comparisons of the displacement profiles after 0.25 and 0.5 PVI are presented in Figures 3-31 and 3-32. The oil production curves are compared in Figure 3-33.

Figure 3-31. Test case 2. Comparison of the Eclipse and the CapSL saturation plots with capillary effects after 0.25 PVI.

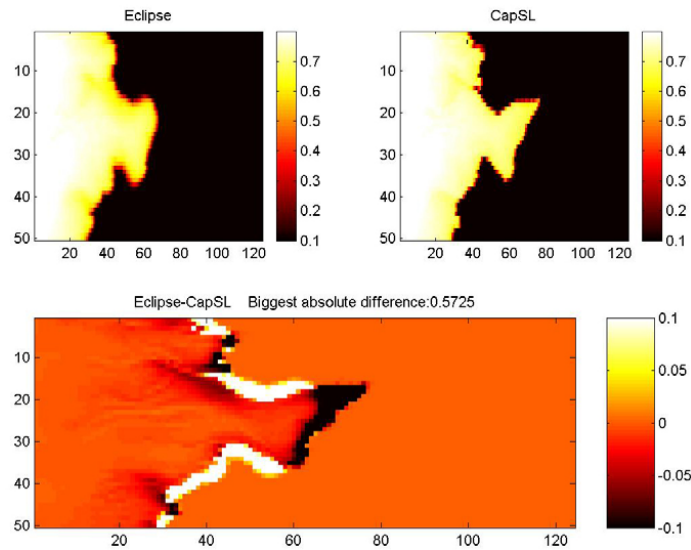*Figure 3-32. Test case 2. Comparison of the Eclipse and the CapSL saturation plots with capillary effects after 0.5 PVI.*
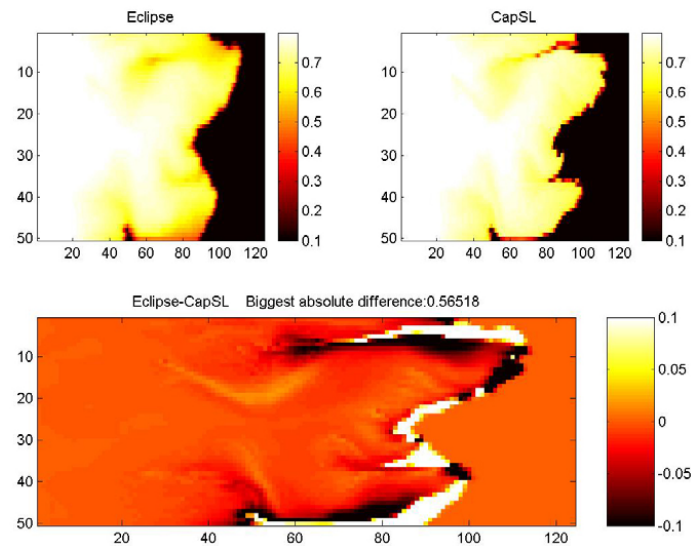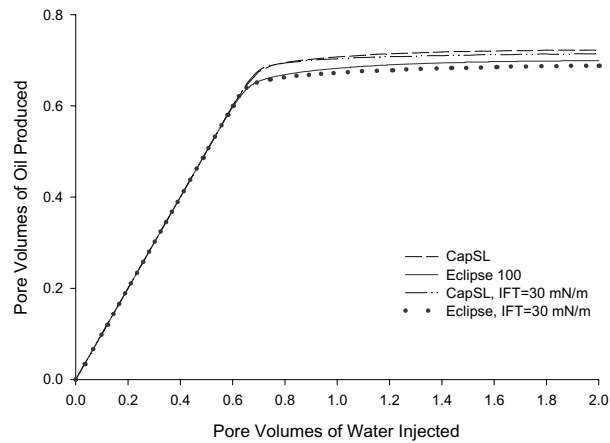

Figure 3-33. Test case 2. Comparison of the Eclipse and the CapSL oil production curves.

The difference between the saturation profiles for the simulations including and neglecting capillary effects is rather large; however the difference in the oil production curves is quite modest.

The simulators performance data is gathered in Table 3-12.

	Neglecting cap. eff.		With cap. eff.	
	CapSL	**Eclipse**	**CapSL**	**Eclipse**
CPU time, min	0.34 (40 time steps)	2 (886 steps)	2.93 (40 time steps)	8 (6981 steps)
Mass bal. error, %PV	0.14	~0	0.04	~0

Table 3-12. Test case 2. Comparison of the Eclipse and the CapSL. The simulation time and the mass balance error.

The CapSL is around 3 times faster comparing to the IMPES Eclipse 100 simulations. The mass balance error is higher for the simulations performed with the CapSL, however, it remains below 0.2%. Judging by Table 3-12, the Eclipse code is much better optimized comparing to the CapSL. For the simulation with capillary effects a single time step in the Eclipse takes around 0.07 seconds. A single time step in the CapSL is around 1.8 seconds. The function timing profile of the CapSL simulation shows that the most time consuming routines are: 1) The corrector step, consuming around 1/3 of the simulation time; 2) The routine calculating the linear approximation of the tabulated values consuming around 1/3 of the simulation time. According to the profile, a single call of this routine lasts only about $1 \cdot 10^{-4}$ millisecond. However, this routine is used for calculating all the physical properties of the phases as functions of saturation, including the relative permeabilities, fractional flow function, and the Leverett function, and it is called around 300 million times in the current simulation run. For the simulation without capillary effects the corrector routine is not used, and the number of calls to the linear approximation routine is significantly smaller as well, resulting in lower simulation time, as shown in Table 3-12.

The streamline simulator shows a higher oil production for the simulations both neglecting and accounting for capillary effects. For the simulation neglecting the capillary effects the higher oil production is due to the later breakthrough as a result of the smaller dispersion of the front. The slopes of the oil production curves after the breakthrough predicted by the CapSL and the Eclipse are in a good agreement. For the simulation with capillary effects both simulators agree on the breakthrough time, however, due to higher local sweep efficiency the CapSL predicts higher oil production again.

The displacement front predicted by the Eclipse shows slower sweeping of the high permeable blocks, see Figures 3-29 and 3-30. Some of these zones remain less swept, comparing to the CapSL even after two pore volumes of water injected, as shown in Figure 3-34.
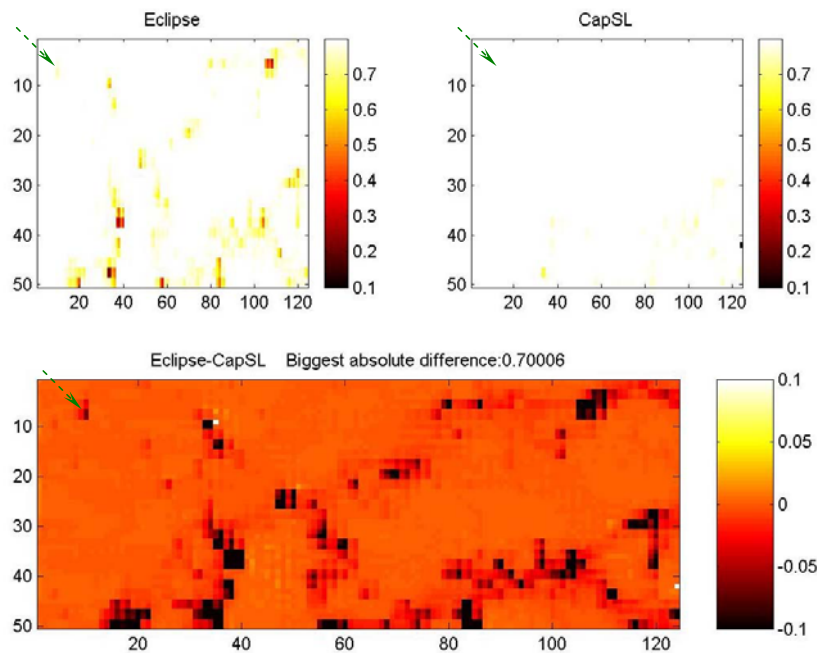
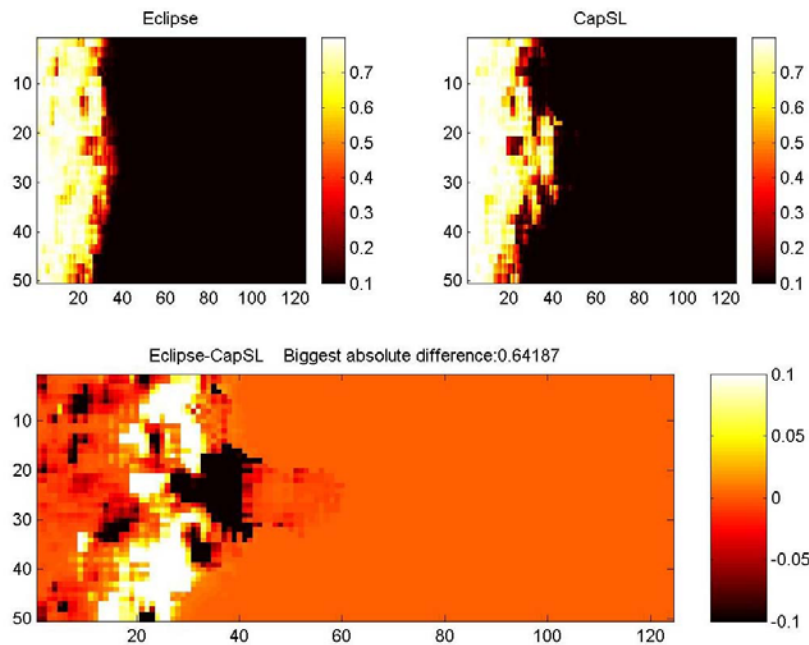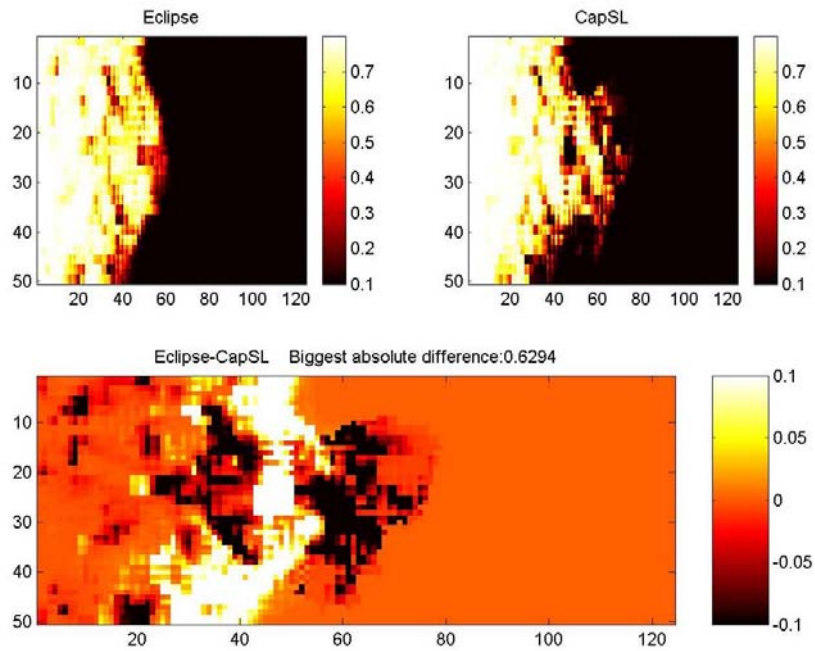*Figure 3-34. Test case 2. Comparison of the Eclipse and the CapSL saturation plots with capillary effects after 2PVI.*

The high permeable blocks are swept as soon as the water saturation in the surrounding blocks rises to the maximum value. The only explanation of slower sweep of the high permeable blocks predicted by Eclipse is that due to the numerical dispersion the saturation increases very slowly to the maximum water saturation, allowing water to flow around the high permeable zone. The low permeable blocks surrounding the high permeable block in the row 9, column 10 in Figure 3-34 (shown with the green arrow) have a water saturation of 0.80 after 2.0 PVI, as predicted by CapSL. The Eclipse shows the water saturation value of around 0.77 – 0.79.

The mass balance error and the CPU time of two different pressure modification methods are shown in Table 3-13.

	CVP + harmonic averaging	SFD + harmonic averaging
CPU time, min	2.93	2.2
Mass. bal. error, %PV	0.04	-0.26

Table 3-13. Test case 2. Comparison of the CVP and the SFD modifications.
The simulation time and the mass balance error.

The SFD method shows no difference in the displacement behavior comparing to the CVP method.

The results presented in Table 3-13 show that for the large scale stochastically heterogeneous simulations with strong capillary forces it is not necessary to use the automatic time step selection routine. Moreover, the simulation with automatic time step selection routine uses 943 steps, and takes nearly two hours. The simulation results in a large mass balance error due to the mapping error.

3.7. Simulation of the three-dimensional heterogeneous case

The last comparison of the CapSL simulations is performed for the 3D simulation case, presented in Section 3.1, see Figures 3-3 and 3-4 and Table 3-3. The SPE10 comparative project [24] has a three orders of magnitude lower permeability in the vertical direction compared to the horizontal one, therefore the gravity effects may be neglected. This case simulates 2000 days or around 2 PV of water injection. The streamline simulation is performed using 20 time steps with application of the CVP and the average saturation methods. Figures 3-35 and 3-36 present the displacement profiles after around 0.1 and 0.5 PVI.
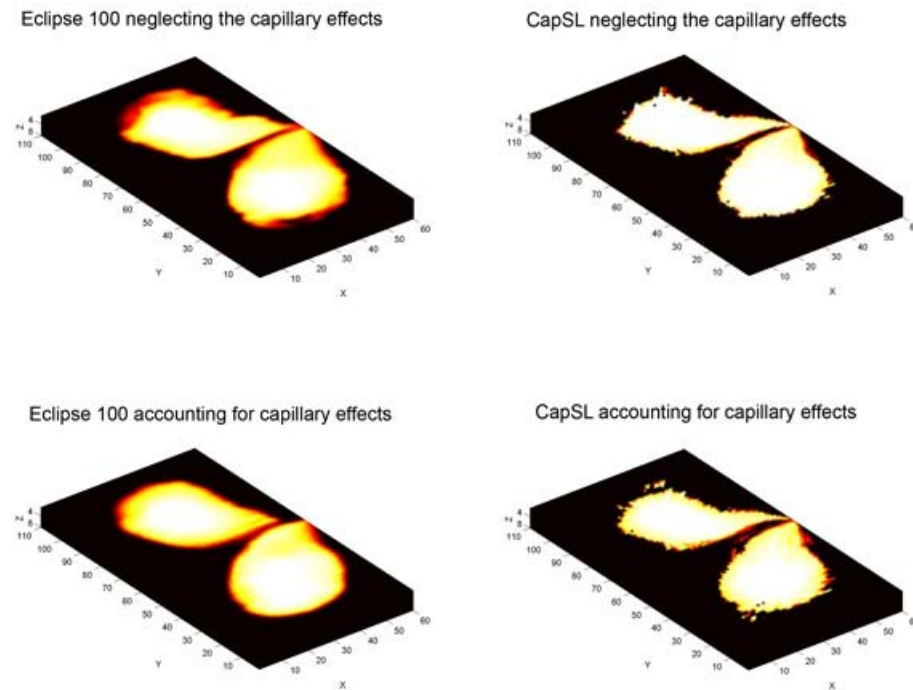
Figure 3-35. Test case 3. Comparison of the Eclipse and the CapSL saturation plots after 0.1 PVI.
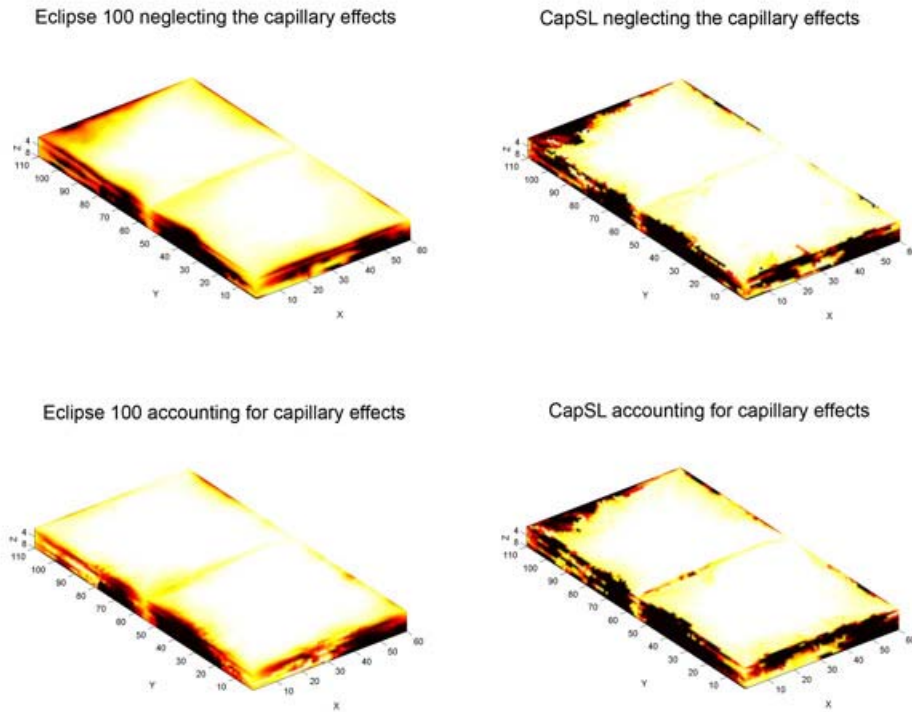
Figure 3-36. Test case 3. Comparison of the Eclipse and the CapSL saturation plots after 0.5 PVI.

The simulation time and the numerical error are reported in Table 3-14.

	Eclipse w/o cap.	**CapSL w/o cap.**	**Eclipse with cap.**	**CapSL with cap.**
CPU time, min	4.85 hours (6930 time steps)	2.9 min (20 time steps)	3.82 hours (6548 time steps)	3 min (20 time steps)
Mass balance error, %PV	1.7	-0.54	2.5	2.7

Table 3-14. Test case 3. Comparison of the Eclipse and the CapSL. The simulation time and the mass balance error

The CapSL results are less affected by the numerical dispersion and better capture the fine features of the displacement front. Comparison of the oil production curves is presented in Figure 3-37.
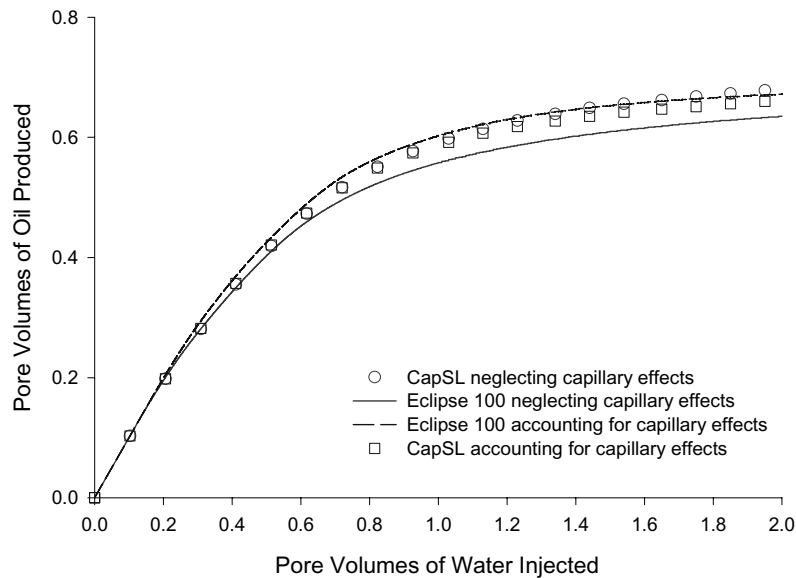
Figure 3-37. Test case 3. Comparison of the Eclipse and the CapSL oil production curves.

Several important conclusions might be drawn based on the analysis of this case. The dimensionless capillary numbers suggest that on the reservoir scale the simulation is viscous dominated. The dimensionless parameters suggested by Bedrikovetsky (Table 3-4) are: $\varepsilon_1/\varepsilon_2 = 0.09$; $\varepsilon_3 = 0$. The dimensionless parameters suggested by Zhou et al. are: $M \cdot N_{cv}/(1+M) = 0.004$; $N_{gv} = 0$. Predictions obtained with the streamline simulator are in a good agreement with the estimation of the displacement regime. The capillary effects show some influence on the local displacement, as shown in Figures 3-35 and 3-36, however, their effect on the total oil production may be neglected. The Eclipse predicts higher total oil production for the simulation accounting for the capillary

effects, compared to the one neglecting the capillary effects. Such behavior might be explained by comparable orders of magnitude of the capillary forces and the numerical dispersion in the Eclipse simulations. Hence, the breakthrough predicted by the Eclipse without capillary forces happens sooner, compared to the CapSL, resulting in a lower total oil production. The oil production curves predicted by the CapSL and the Eclipse for the simulation with capillary effects show a good agreement.

The SFD and the CVP methods show excellent match as well. Both the CVP and the SFD simulations complete in about 3 minutes and have the same mass balance error. Simulations with average saturation do not improve the CapSL performance as well.

Both the Eclipse and the CapSL simulations result in rather high volume balance errors. The CapSL simulations with automatic time step selection routines resulted in the same volume balance error.

3.8. Comparison summary

Based on the simulation cases presented in this chapter, the two simulation types may be distinguished.

The first type is the simulations of the heterogeneous reservoirs comprised of two and more homogeneous zones with several well-defined permeability borders. Typically, such kinds of runs are used for the simulation of the laboratory scale displacements or the preliminary assessment of the models on the simple permeability data. The CVP method may be recommended to speed up the simulation and to decrease the numerical error. The average saturation method should be chosen to provide correct description of the capillary cross flow through the permeability borders. The application of the automatic time

step routines facilitates better mach with the Eclipse simulation results, but may also result in larger numerical errors.

For the simulations of the stochastically heterogeneous or similar reservoirs with varying permeability and / or porosity it is advisable to take large time steps. The time steps may be restricted by specifying the maximum mass balance error. There is no principal difference in the simulations using various methods of accounting for capillary effects in the pressure and the saturation equations. Typically, such runs represent the full-scale simulation of the reservoir data. The streamline simulator may be used as a tool to access the difficulties and visualize the relative strength of the capillary and the gravitational forces as well as the main reservoir simulation tool.

4. Sample calculations and effects

This chapter starts with illustration and discussion of the capillary end-effects. The effect of the rock wettability on the capillary forces is discussed. Streamline simulations of alternated wet media are presented.

Later in the chapter the CapSL is tested in the range of capillary forces and mobility ratios corresponding to water / oil displacements.

The chapter concludes with the CapSL and the Eclipse 100 [62] simulations of the lab-scale data kindly provided by Yildiray Cinar, SUPRI-C, Department of Petroleum Engineering, Stanford University.

4.1 Capillary effects in porous media

Capillary effects in porous media may be separated into the three groups:
- Smearing of the saturation front by capillary effects;
- Capillary effects on the borders of the media with different permeability;
- Capillary effects on the borders of the media with different wettability.

This section is divided into the two parts. First, the water wet media is investigated, the effects of heterogeneity in the water wet reservoirs are presented. Later, the alternated wet media is simulated.

4.1.1. Capillary effects in water wet medium

The front smearing effects are illustrated on a simple one-dimensional laboratory-scale 1D case. The simulation grid is comprised of 1500 grid blocks. The sample is 15·5·5 cm in size. The production pressure is 1 atm; the injection

rate is 6.25 cc/h. The relative permeability curves and the J-function are taken from the test case 3, see Table 3-3. The initial water saturation is 0.1. The water viscosity is 0.7cP, the oil viscosity is 0.9cP. The interfacial tension between the fluids is set to 0.3 mN/m. The sample permeability is 400mD. 4 hours of water injection are simulated. The simulation is capillary dominated with $\varepsilon_1 = 4.5$, $\varepsilon_2 = 0.11$.

The displacement profiles after 3, 5 and 10 time steps obtained with the CapSL are presented in Figure 4-1.

Smearing of the saturation front is due to the gradient of the Leverett function and happens in heterogeneous and homogeneous, water wet and oil wet porous media [13]. For the one-dimensional case the simulation neglecting capillary effects is described by the Buckley-Leverett equation [22]. The one-dimensional simulation accounting for capillary effects is described by the Rappoport – Leas equation [58].
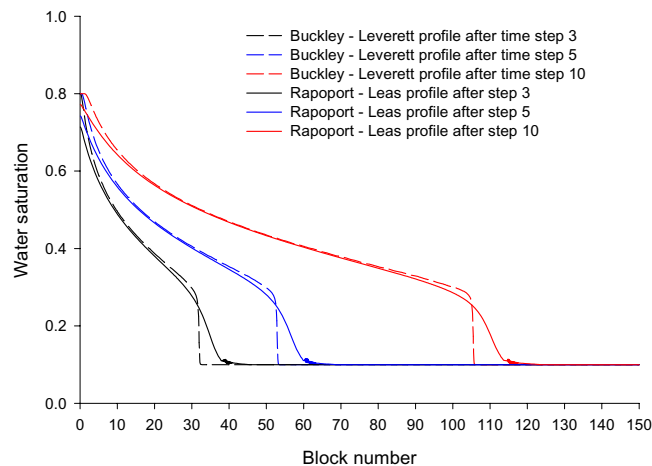
Figure 4-1. 1D saturation profiles neglecting and accounting for capillary effects.

The capillary cross-flow is illustrated by simulating a part of the reservoir. The sample is 150·1·1 m and simulated on the 1D grid with 1500 grid blocks. The fluid data is taken from the test case 3, see Table 3-3. The capillary to viscous

ratio is very small: $\varepsilon_1 = 0.03$, however, the anisotropy ratio is very small as well, as a result the case is capillary dominated with $\varepsilon_1 / \varepsilon_2 = 172$.

On the borders of the different permeabilities the $\nabla\Phi$ gradient plays a vital role. The end-effects appear on the borders of permeability between the low and the high permeable media [12, 13]. The simulation grid is now comprised of 500 blocks with 100mD permeability, followed by 500 blocks with 400mD permeability and finished with 500 blocks with 100mD permeability again. The saturation profiles after time steps 2, 3, 5 and 10 are presented in Figure 4-2. The saturation discontinuities may be noticed around 500th and 1000th grid blocks. When water propagates in the low permeable media and reaches the border with the high permeable one, the water saturation on the boundary in the low permeable zone quickly increases up to the maximum water saturation. Then the water phase breaks through into the high permeable zone. Upon reaching the end of the high permeable zone the water is sucked out of the high permeable into the low permeable media by the $\nabla\Phi$ gradient. The boundary layers in the high permeable media are swept by water with time.
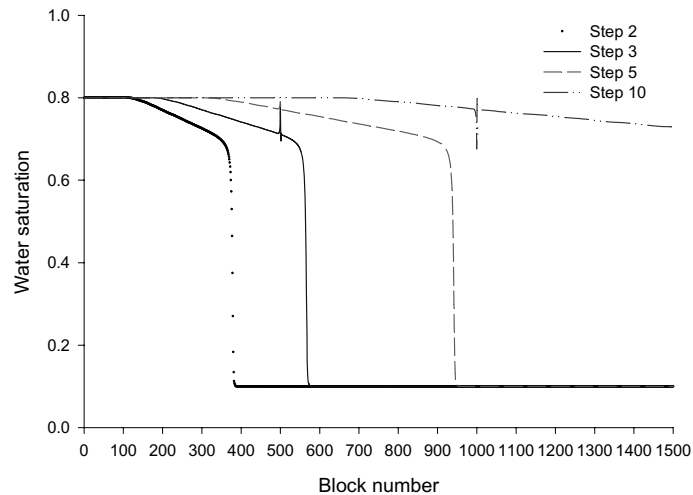
Figure 4-2. 1D saturation profiles in heterogeneous media.

The simulations demonstrated above are one-dimensional and homogeneous in the transverse direction. In order to investigate the cross flow effect, the two dimensional simulation system is used as sketched in Figure 4-3.

The top layer is homogeneous and consists of low permeable Rock1 with the permeability of 100mD. The bottom layer consists of Rock1 and Rock2 with the permeability of 400mD. Both Rock1 and Rock2 are water wet. The size of the grid blocks is 1·1·1m as in the 1D simulation. The pore volume of the 2D simulation sketched in Figure 4-3 is twice as large as the pore volume of the 1D simulations presented at the beginning of this section. To be able to compare the results to the 1D simulation the injection rate is doubled. The results are shown in Figure 4-4.
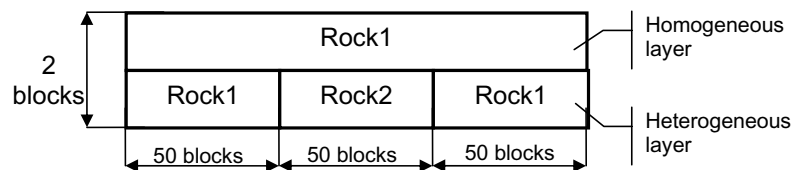
Figure 4-3. 2D cross flow investigation grid.

The saturation profiles in the heterogeneous layer are compared to the 1D profiles in Figure 4-2. The homogeneous layer saturation profiles are compared to the homogeneous 1D profiles from Figure 4-1.

As it may be seen from Figure 4-4, the saturation profiles in the first 500 blocks of the 2D simulation match with corresponding 1D profiles.

Differences in the saturation profiles in both homogeneous and heterogeneous layers appear in the Rock2 zone, above it and right after it. The saturation in the Rock2 zone is lower compared to the 1D simulation due to the capillary cross flow. The water is transferred into more preferable Rock1 above, therefore the water saturation in the homogeneous layers is higher comparing to the 1D profile.

As it may be seen from Figure 4-4, after the sixth time step the water saturation in the end of the Rock2 zone is lower compared to the 1D solution due to capillary forces acting not only in the longitude but in the transverse direction as well. Also, it may be noticed that the front in the homogeneous layer of the 2D simulation is slightly ahead of the homogenous 1D solution after step 3 and behind the homogeneous 1D solution after step 6. Speeding up the saturation front after step 3 is due to additional capillary cross flow influx from the underlying Rock2. This influx is due to the permeability difference and is controlled by the $\nabla \Phi$ gradient. On the other hand, due to the capillary cross flow a significant amount of water travels in transverse direction, rather than in longitude one. As a result water propagates slower towards production well, resulting in the slow down of the front after time step 6.
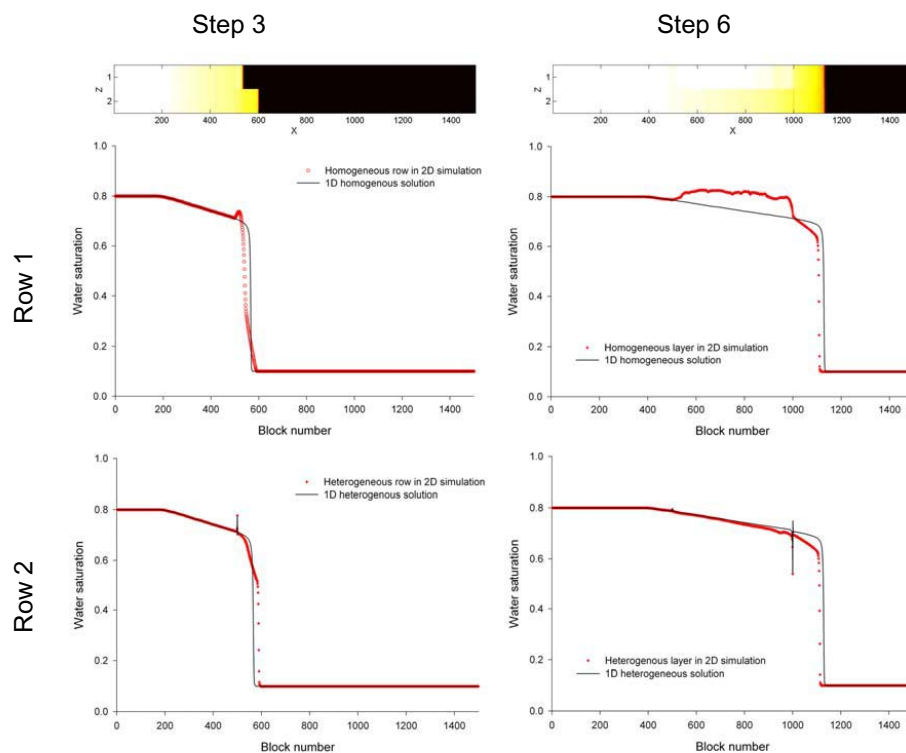
Figure 4-4. 2D heterogeneous simulation. Saturation profiles.

4.1.2. Capillary effects in oil wet and alternated wet media

The relative permeability functions and the Leverett curve for the oil wet and the water wet rocks may be entirely different. For simplicity of comparison, we assume that behavior of the water phase in the oil wet rock is similar to the behavior of the oil phase in the water wet rock. Hence, the relative permeability curves and the Leverett function as functions of the wetting phase saturation are exactly the same in the oil wet and the water wet media. However, the governing systems of equations are solved in terms of the water phase properties regardless of the rock wettability. Since the sum of the water and the oil saturations must be always equal to unity, the curves for the oil wet rock in terms of water saturation are flipped along the vertical axes passing through the 0.5 water saturation, compared to the water wet case. The relative permeability curves and the Leverett function for the oil wet rock, in comparison with the water wet rock, are presented in Figure 4-5.
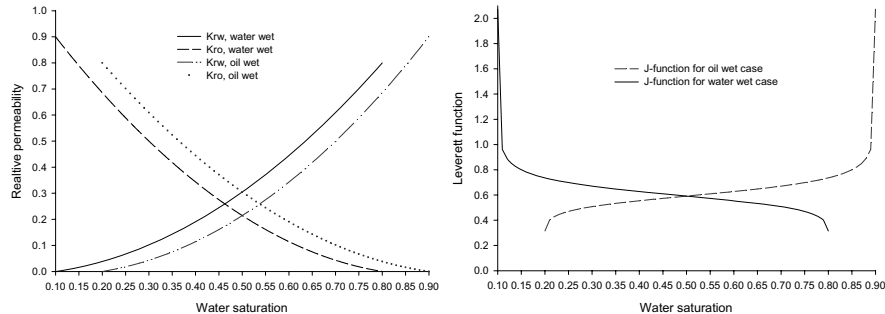
Figure 4-5. The relative permeabilities and the Leverett function curves for the water and the oil wet rocks.

The 1D simulation in the alternated wet medium is carried out on the grid similar to the heterogeneous simulation in Section 4.1.1. The first 500 blocks of the simulation are water wet, the next 500 are oil wet and the last 500 are water wet again. The permeability in all the blocks is fixed at 100mD. The saturation profiles are presented in Figure 4-6.

In general, the behavior of the saturation profiles in the water wet regions is similar to the heterogeneous water wet simulation, Figure 4-2.

The water saturation in the oil wet zone does not show a drop as in the heterogeneous water wet simulation. The main reason for this lies in the difference in the relative permeabilities and the Leverett function curves in the oil wet zone compared to the water wet one.

The saturation region where the water phase is mobile is also different. Water in the water wet media is mobile if its saturation is above 0.1. The oil in the water wet media is mobile if its saturation is above 0.2. In the oil wet media the water saturation has to be above 0.2 and the oil saturation above 0.1 for the phases to be mobile. This leads to higher water saturation in the oil wet zone, compared to the water wet one.
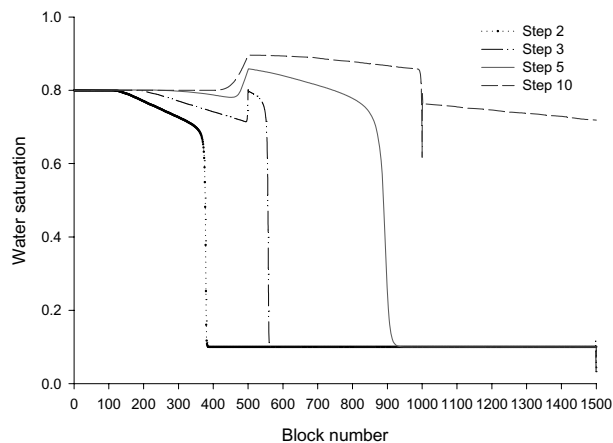
Figure 4-6. 1D saturation profiles for alternated wet reservoir.

The 2D alternated wet simulation is performed on the grid presented in Figure 4-3.

The permeabilities of Rock1 and the Rock2 are fixed at 100mD. The Rock1 is water wet, the Rock2 is oil wet. The saturation profiles are shown in Figure 4-7.

The capillary forces between the oil wet and the water wet media are much stronger, compared to the capillary forces between the zones with different permeabilities. The maximum capillary pressure difference in the water wet media may be achieved on a border of the zones with different heterogeneities:

$$\Delta P_{c,max} = \Phi\left(high\ perm\right) \cdot J\left(s_{max}\right) - \Phi\left(low\ perm\right) \cdot J\left(s_{min}\right). \qquad (4.1)$$

The maximum capillary pressure difference for the homogeneous alternated wet case is:

$$\Delta P_{c,max} = \Phi \cdot \left(J_{water\ wet}\left(s_{max}\right) + J_{oil\ wet}\left(s_{min}\right)\right). \qquad (4.2)$$

The positive sign in equation (4.2) is due to $\cos\theta = -1$ in the oil wet media.

Stronger capillary forces between Rock2 and Rock1 result in the saturation "hump" inside the Rock2 zone, see Step 6 in Figure 4-7.
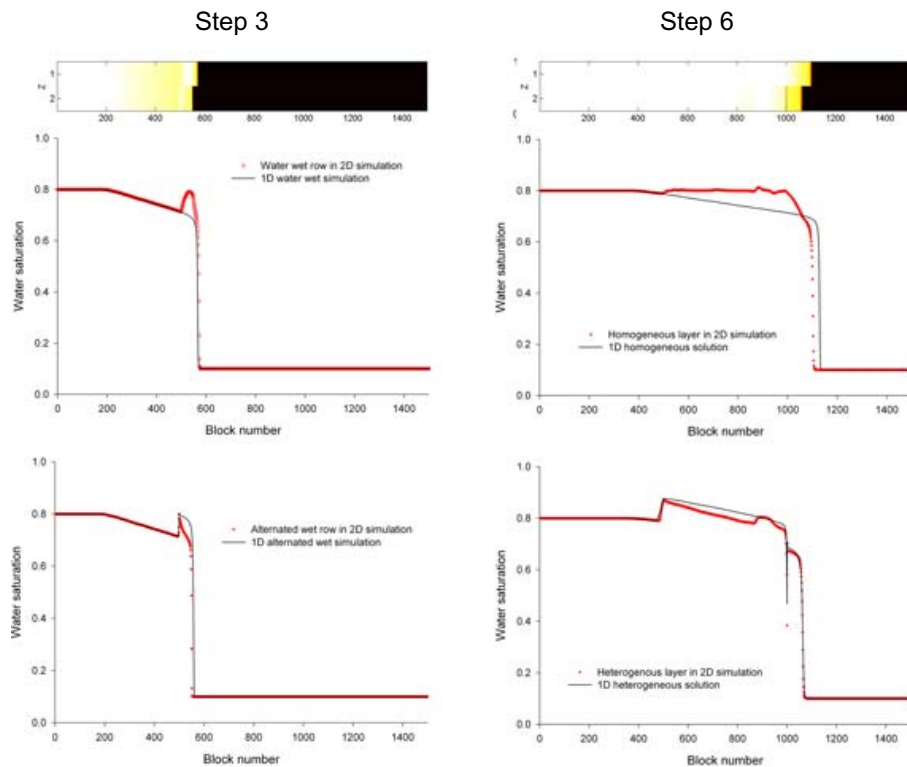
Figure 4-7. Alternated-wetting medium simulation. Saturation profiles.

Due to the strong cross flow water is transferred from Rock2 into above lying Rock1 very quickly. The zone of maximum water saturation in the Rock1 after time step 3 is wider for the alternated wet case, Figure 4-7, compared to the heterogeneous simulation, Figure 4-4. As a result a water bank with maximum water saturation is very quickly formed inside Rock1 above Rock2. This water bank propagates towards the producer well. Since the water saturation in the bank is at its maximum value, no cross flow from the underlying Rock2 is possible. The water saturation behind the bank is lower, resulting in the fact that more water is transferred by the cross flow in the beginning of Rock2 zone, than in the end of it. This explains higher saturation in blocks 750-900 compared to blocks 500-750.

There are also some numerical problems in the alternated wet simulation, for example, a little saturation peak in the heterogeneous layer after the sixth time step. The saturation in this peak exceeds the maximum water saturation, suggesting that the time step selection has to be improved.

The comparison of the CapSL and the Eclipse simulations are presented in Figure 4-8.

Both simulators show a good match in the saturation profile after time step 3. The oil production curves predicted by the Eclipse and the CapSL are showing an excellent match in the breakthrough time and the overall oil production.

It is important to point out that all fine scale simulations required fully automatic time step selection. The simulations with manual steps may result in various saturation instabilities, for example, water saturation might fluctuate or the oil saturation might decrease below immobile oil saturation.
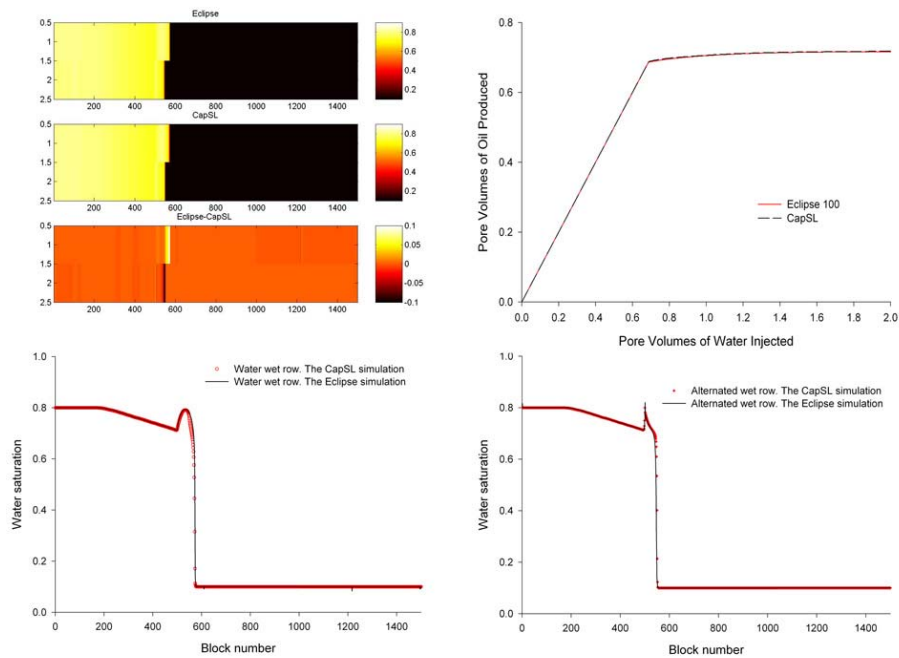
Figure 4-8. Comparison of the CapSL and the Eclipse simulations for alternated wet reservoir.

4.2. Zone of application of the streamline simulator with capillary effects

In Section 3.1 it is shown that the simulation grids comprised of the homogeneous zones are more complicated to handle using the streamline simulator comparing to the stochastically heterogeneous media. Therefore the two-dimensional system, comprised of two zones with different permeability is selected for determination of the zone of application, as sketched in Figure 4-9. The run data are collected in Table 4-1. The values of phase viscosities and interfacial tension vary between the runs and are reported in Table 4-2. The phase densities are set to equal values to completely remove gravity effects.

This case represents a simplified stratified reservoir, in which the capillary effects play a vital role in distribution of the fluids between the zones of different permeabilities. This case is simple enough, so that the effects of capillary forces and phase mobility variations may easily be interpreted.
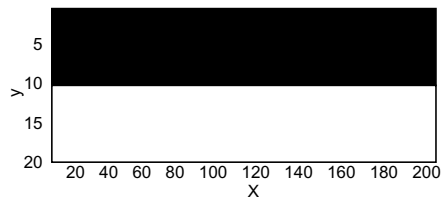
Figure 4-9. The permeability field for investigation the zone of application of the streamline simulator with capillary effects.

The low permeable zone has the permeability of 50mD and is shown in black color in Figure 4-9. The high permeable zone has the permeability of 400mD and is shown in white in Figure 4-9.

The streamline simulations are performed applying the CVP method and the average saturation method in the saturation equation. The automatic time step selection routine is applied as well.

The Eclipse 100 simulations are performed in the IMPES mode. The simulations are performed on the 200·20 grid. The convergence of the numerical schemes is checked by refining the grid to 400·40. The difference in the oil production curves on the different grids is below 0.5% relative to the pore volumes of water injected.
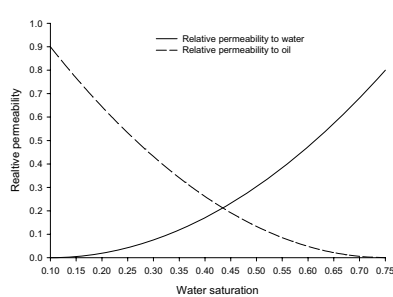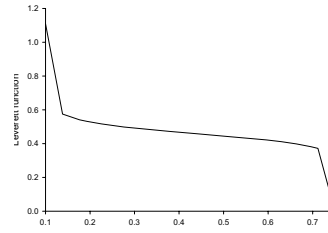
Parameter	Value	
Simulation grid	200·20 areal slice; 4·4·1 m grid blocks	
Porosity	0.4	
Pore volume	25600 m^3	
Densities	Water – 1000 kg/m^3	Oil – 1000 kg/m^3
Relative permeabilities	$k_{rw} = k_{rwor} \left(\dfrac{s - s_{wi}}{1 - s_{wi} - s_{or}} \right)^2$ $k_{ro} = k_{rowi} \left(1 - \dfrac{s - s_{wi}}{1 - s_{wi} - s_{or}} \right)$ $k_{rwor} = 0.8$ $k_{rowi} = 0.9$ $s_{wi} = 0.1$ $s_{or} = 0.25$	
Injection rate	2.0 m^3/day (1 pore volume injected in 12800 days)	
Production pressure	20.0 MPa (producer located on the right)	
Capillary pressure	$J(s) = \alpha \left[\left(\dfrac{s - s_{min}}{1 - s_{max} - s_{min}} \right)^{-1/m} - 1 \right]^{1/n} - y, \quad n = \dfrac{1}{1 - m}$ $\alpha = 0.5$ $m = 0.93$ $y = 0.05$ $s_{min} = 0.0999$ $s_{max} = 0.25$ 	

Table 4-1. The simulation data for investigation the zone of application of the streamline simulator with capillary effects.

Run number	IFT (σ) mN/m	μ_o cP	μ_w cP	$\varepsilon_1/\varepsilon_2$	M	Displ. regime
1	0	1	1	0.058	0.89	Viscous
2	1	1	1	0.292	0.89	Viscous
3	10	1	1	2.916	0.89	Capillary
4	30	1	1	8.748	0.89	Capillary
5	0	5	1	0.000	4.49	Viscous
6	0	10	1	0.000	8.89	Viscous
7	0	20	1	0.000	17.78	Viscous
8	1	5	1	0.058	4.44	Viscous
9	10	5	1	0.583	4.44	Viscous
10	30	5	1	1.750	4.44	Capillary
11	1	10	1	0.029	8.89	Viscous
12	30	10	1	0.875	8.89	Viscous
13	1	20	1	0.015	17.78	Viscous
14	30	20	1	0.437	17.78	Viscous
15	72	20	1	1.048	17.78	Viscous

Table 4-2. Run specific data for investigation the zone of application of the streamline simulator with capillary effects.

The parameters presented in Table 4-2 cover a wide range of mobility ratios and interfacial tensions typical for reservoir simulation problems. The results are divided into three groups: 1) Varying interfacial tension at constant mobility ratio ; 2) Varying mobility ratio at constant interfacial tension; 3) Varying both interfacial tension and mobility ratio.The simulation times for the various runs are not compared since all the runs took less than a minute. However, the number of time steps and the mass balance error are reported for each run in Table 4-3.

Run number	IFT mN/m	M	Eclipse		CapSL	
			steps	error, % PV	steps	error, %PV
1	0	0.89	1276	$-1.1*10^{-5}$	149	0.39
2	1	0.89	1376	$1.50*10^{-5}$	156	0.33
3	10	0.89	1307	$-2.90*10^{-7}$	204	0.26
4	30	0.89	1252	$-1.70*10^{-4}$	235	0.31
5	0	4.49	778	$-2.50*10^{-7}$	47	0.39
6	0	8.89	707	$8.08*10^{-7}$	50	0.51
7	0	17.78	668	$-1.20*10^{-6}$	56	0.58
8	1	4.44	891	$-6.10*10^{-7}$	62	0.30
9	10	4.44	920	$1.26*10^{-6}$	108	0.13
10	30	4.44	905	$-1.40*10^{-4}$	136	0.21
11	1	8.89	788	$3.22*10^{-6}$	60	0.42
12	30	8.89	840	$-6.20*10^{-5}$	129	0.26
13	1	17.78	735	$1.09*10^{-6}$	62	0.45
14	30	17.78	819	$3.25*10^{-6}$	138	0.25
15	72	17.78	848	$-1.10*10^{-4}$	197	0.07

Table 4-3. Investigation of the zone of application of the streamline simulator with capillary effects. Number of time steps and simulation errors.

The mass balance error in all the Eclipse 100 simulations is fairly close to zero. The error in the CapSL simulations is higher; however, it does not exceed the value of 0.51 %PV. The streamline simulator performs 4 to 16 times less time steps. The dependency of the number of time steps as a function of the mobility ratio is presented in Figure 4-10. The dependency of the number of time steps as a function of interfacial tension is presented in Figure 4-11.

Figure 4-10. Investigation of the zone of application of the streamline simulator with capillary effects. Number of time steps as a function of the mobility ratio.

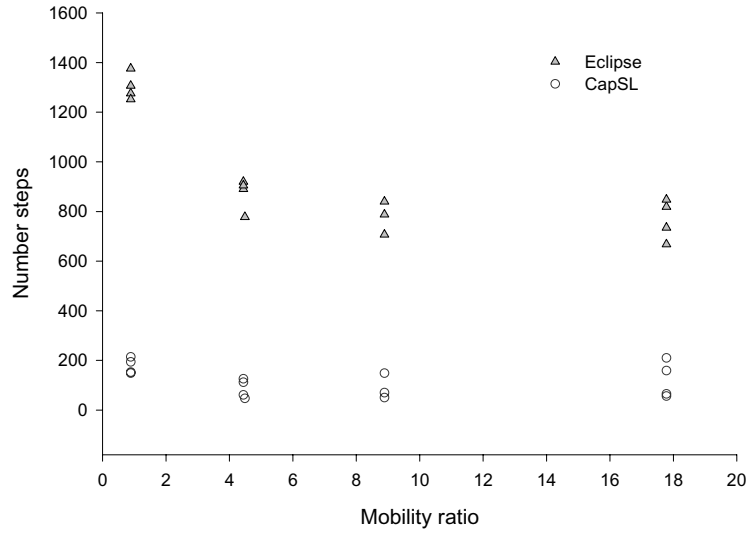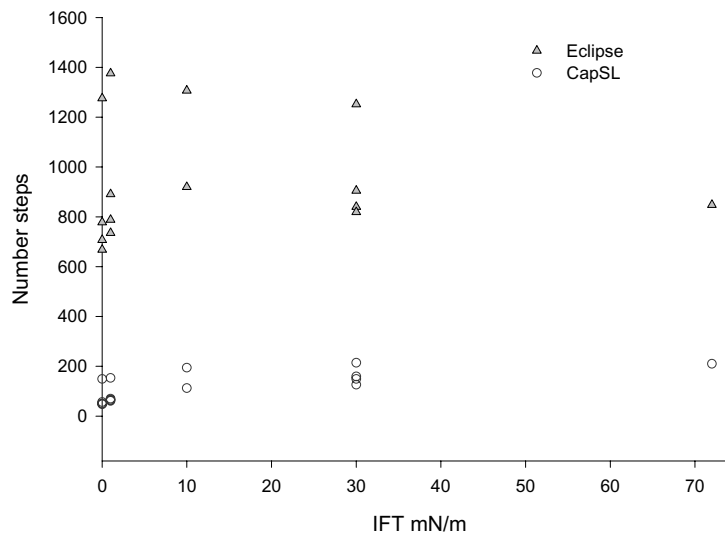*Figure 4-11. Investigation of the zone of application of the streamline simulator with capillary effects. Number of time steps as a function of the interfacial tension*

The number of time steps decreases as a function of the mobility ratio. This is associated with the faster breakthrough. The simulations with higher mobility ratios require smaller time steps before the breakthrough due to faster propagation of the saturation front. On the other hand, breakthrough happens sooner. Since changes in the pressure and the velocity after the breakthrough are rather small, the time steps after breakthrough a typically large. Increasing mobility ratio from 1 to 9, decreases the total number of time steps. However, further increase of the mobility ratio results in the same number of time step or even in a small increase of the number of time steps. The mobility ratio 9 is probably specific for this case and should not be used in a general sense.

The number of time steps increases as a function of the interfacial tension. Increase of the interfacial tension means stronger capillary forces, resulting in smaller time steps to account for capillary cross flow.

First, the effect of increase of capillary forces by increasing the interfacial tensions at constant mobility ratio is observed based on runs 1-4. Secondly, increase of the mobility ratio under constant interfacial tension is studied basing on runs 1, 5-7. Finally, increase of both effects is illustrated on the basis of runs 2, 9, 12, 15.

The oil production curves for the simulation with different interfacial tension and fixed mobility ratio (runs 1-4) are presented in Figure 4-12. The oil production curves obtained using the Eclipse and the CapSL show excellent match. Both simulators agree on later breakthrough times and higher oil productions for the stronger capillary forces. The delayed breakthrough and the higher oil production are both the results of the capillary cross flow.

Figure 4-12. Investigation of the zone of application of the streamline simulator with capillary effects. Oil production curves for runs 1-4.

The saturation profiles after 2000 days (around 0.156PVI) are presented in Figure 4-13.

In all the four runs the Eclipse predicts slightly higher cross flow (white and light yellow zones in the comparison plots). The difference in the saturation profiles increases with an increasing interfacial tension. The difference in the flow profiles is probably due to the numerical smearing of the finite-difference solution.

The simulations with fixed interfacial tension and varying mobility ratio show excellent agreement as well. The oil production curves are shown in Figure 4-14.

Run1

Run 2

Run 3

Run 4

Figure 4-13. Investigation of the zone of application of the streamline simulator with capillary effects.Saturation profiles after 2000 days for the runs 1-4.

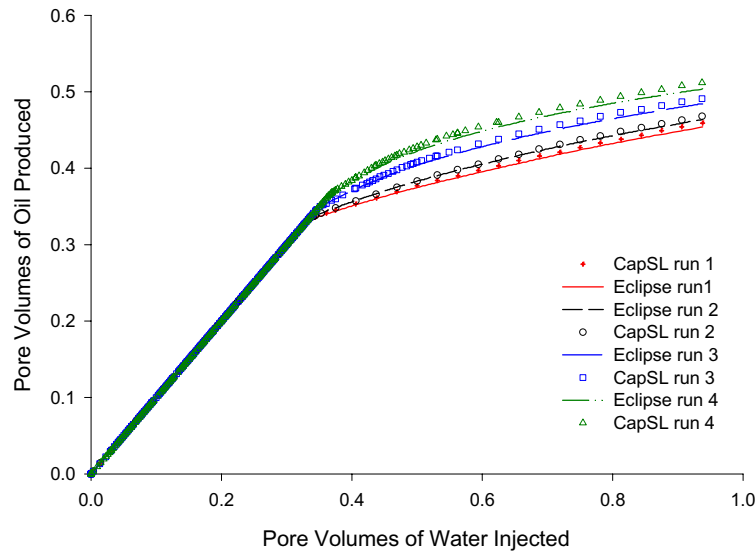*Figure 4-14. Investigation of the zone of application of the streamline simulator with capillary effects. Oil production curves for runs 1, 5, 6, 7.*

The saturation profiles after 2000 days (around 0.156PVI) are presented in Figure 4-15. In Figure 4-15 for each simulation run the top left figure is produced by Eclipse, the top right one by the CapSL and the bottom one is the difference between the Eclipse and the CapSL results.
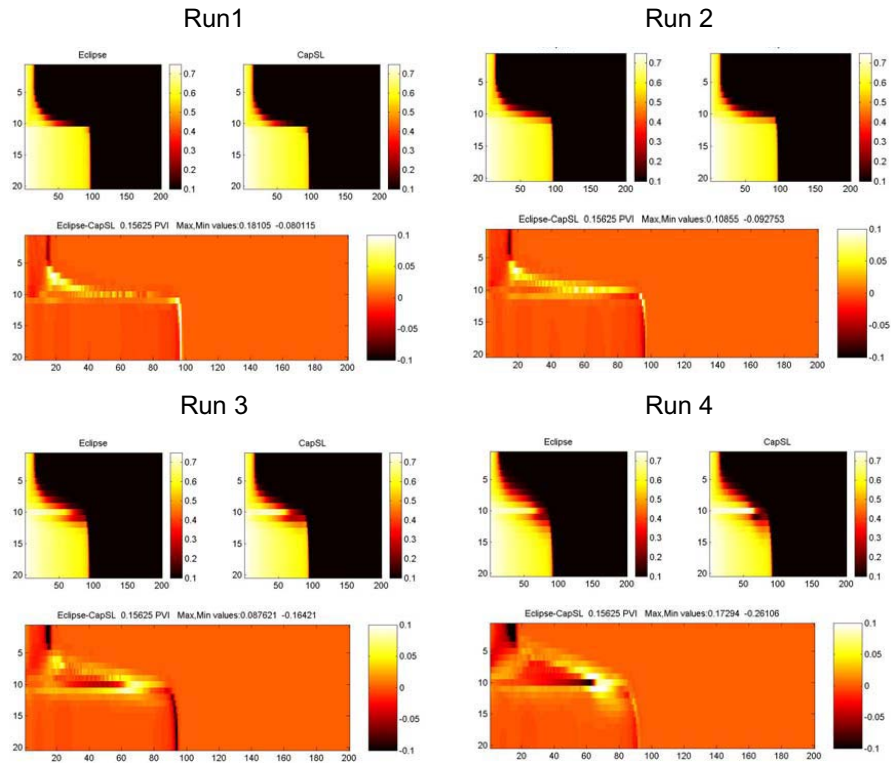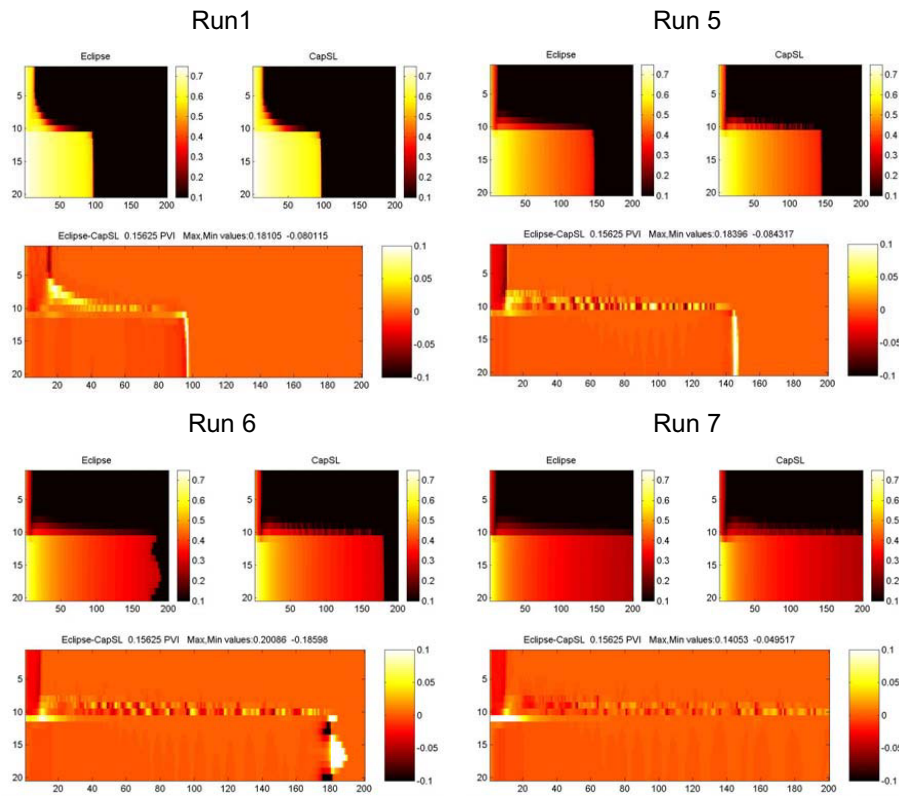

Figure 4-15. Investigation of the zone of application of the streamline simulator with capillary effects. Saturation profiles after 2000 days for the runs 1, 5-7.

The total amount of oil produced decreases with an increasing mobility ratio due to faster breakthrough and smaller sweep efficiency, see Figure 4-15. Both simulators show some numerical instability under high mobility ratios. The Eclipse front in the high permeable area is s-shaped. The CapSL saturation front in the low permeable media shows some disturbance in the saturation values. However it should be pointed out that the situation where the two fluids

have a large viscosity difference and very small interfacial tension lies outside of the real-life cases. The test simulations here are performed in order to test the simulators in the extreme conditions.

The third comparison is more realistic as the interfacial tension increases together with the mobility ratio. The oil production curves are shown in Figure 4-16.

Figure 4-16. Investigation of the zone of application of the streamline simulator with capillary effects. Oil production curves for runs 2, 9, 12, 15.

Increase of the sweep efficiency as a result of stronger capillary cross flow did not compensated for faster breakthrough as a result of increasing viscosity difference. As a result, the total volume of oil produced decreases from run 2 to run 15. The oil production curves predicted by the Eclipse and the CapSL are in excellent agreement. The saturation profiles are presented in Figure 4-17.

Despite the fact that the simulation is viscous dominated for runs 9,12, and 15, the capillary effects are locally important and the capillary cross flow is quite pronounced on the border of zones with different permeabilities.

Run 2   Run 9

Run 12   Run 15

Figure 4-17. Investigation of the zone of application of the streamline simulator with capillary effects. Saturation profiles after 2000 days for the runs 2, 9, 12, 15.
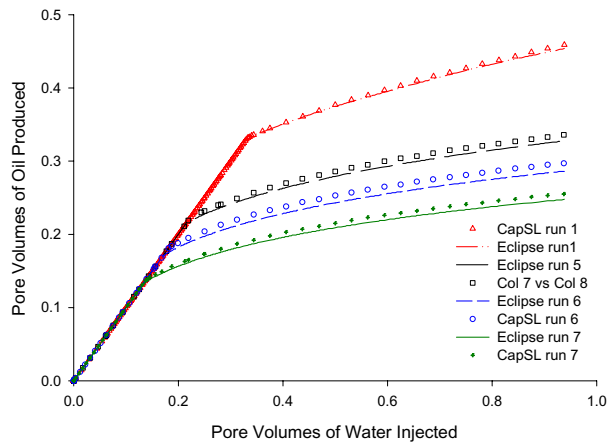
In Figure 4-17 for each simulation run the top left figure is produced by Eclipse, the top right one by the CapSL and the bottom one is the difference between the Eclipse and the CapSL results.

Finally, run 4 is modified to include the gravitational forces and represents the vertical cross-section of a reservoir. The oil density is set to 800 kg/m^3, the water density to 1000 kg/m^3. The saturation profiles predicted by the Eclipse and the CapSL are presented in Figure 4-18.

2000 days   4000 days
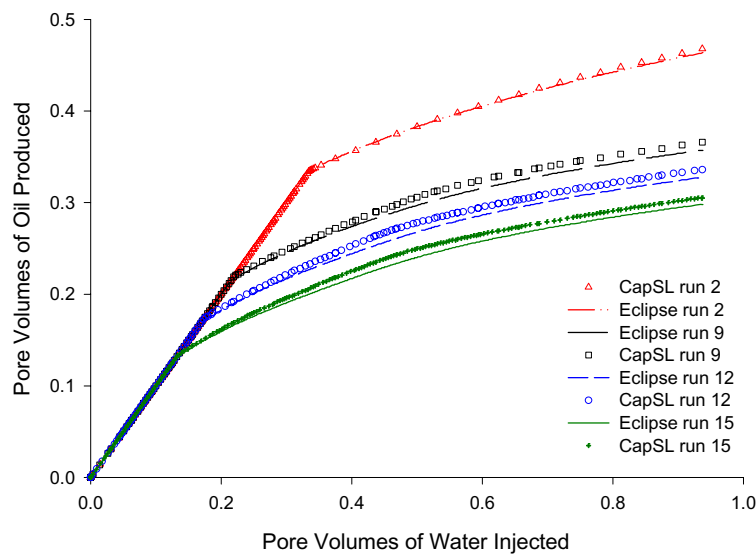

8000 days   12000 days

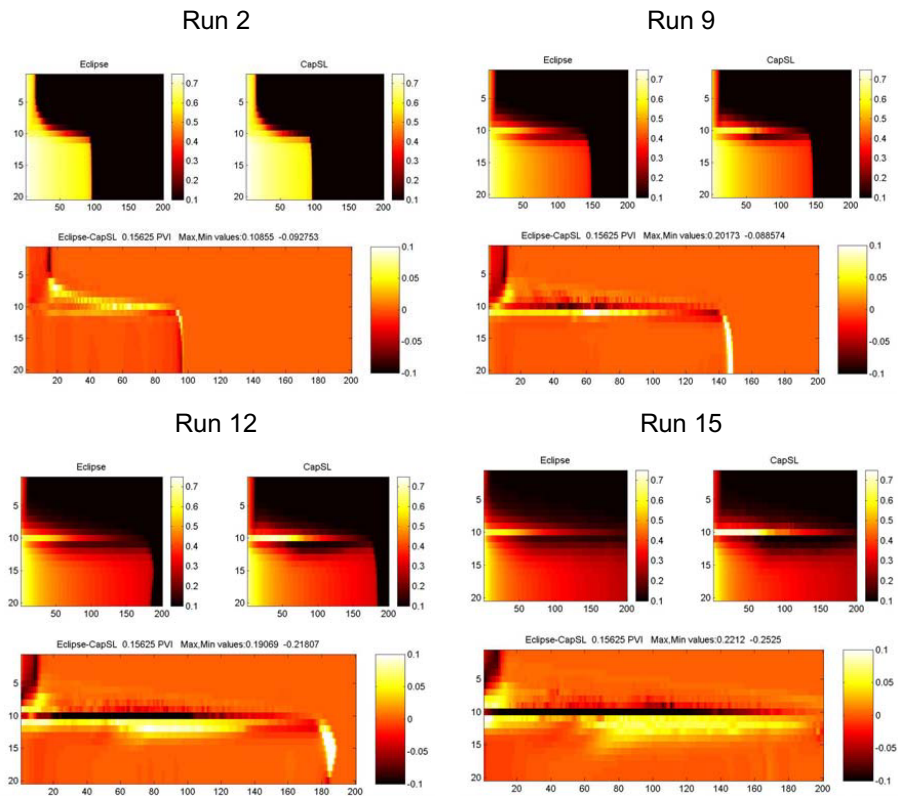*Figure 4-18. Investigation of the zone of application of the streamline simulator with capillary effects. Saturation profiles for run 4 accounting for gravity forces.*

In Figure 4-18 for each simulation run the top left figure is produced by Eclipse, the top right one by the CapSL and the bottom one is the difference between the Eclipse and the CapSL results.

The saturation profiles show a good match. The CapSL shows a slightly stronger capillary cross flow. The increase of the water saturation in the vicinity of the production well reflects drowning of the production well. The oil production curves for run 4 including gravitational effects are shown in Figure 4-19. Due to the higher sweep of the low permeable zone the CapSL predicts higher oil production for the simulation with gravity forces, compared to the Eclipse.
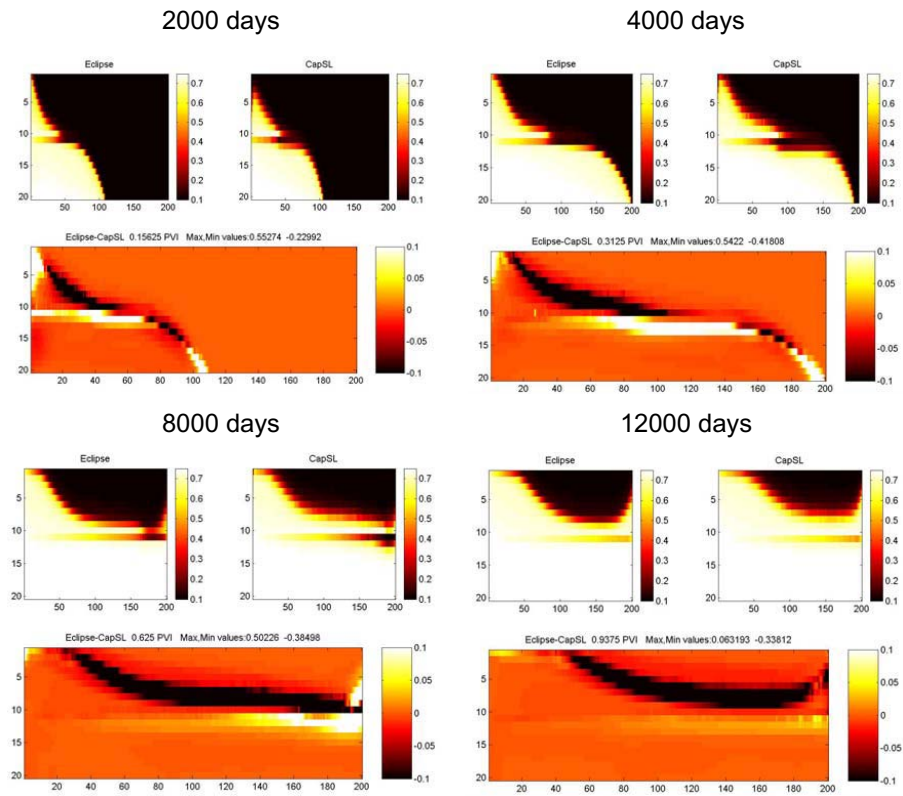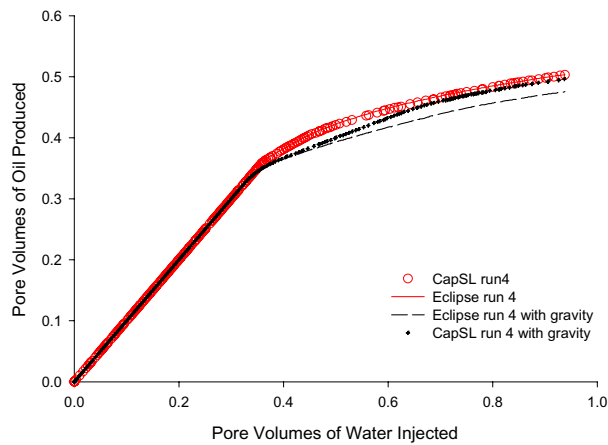
Figure 4-19. Investigation of the zone of application of the streamline simulator with capillary effects. Oil production curves for run 4 with and without gravity.

Based on the comparison of these test runs the following conclusions may be produced:

- The CapSL makes it possible to simulate displacements with capillary effects and to obtain the predictions comparable to the industry-standard reservoir simulator Eclipse 100, using 5 to 10 times less pressure updates;

- The CapSL is applicable to the full test range of the mobility ratios from 0.89 to 17.78, representing the displacements from favorable to highly unfavorable regimes;

- The CapSL is applicable to the full test range of the capillary forces. The capillary forces have been tested in the range of the interfacial tension values from 0 mN/m, representing the tracer flow, to 72 mN/m;

- The test cases with high mobility ratios without capillary forces result in numerical problems in both simulators, such as numerical instabilities on the viscous or capillary enhanced displacement fronts;

- More realistic simulation cases are better handled by both simulators and the predictions obtained are more comparable. For example, the numerical instabilities decrease when the surface tension is non-zero for the fluids with large viscosity difference;

- Both simulators predicts water coning in the vicinity of the production well for the simulation with gravity and capillary effects.

4.3. Laboratory scale simulations

In this section the CapSL and the Eclipse simulations are compared to the experimental data. The laboratory data, the relative permeability and the Leverett function curves as well as the sketches of the laboratory set-up were kindly provided by Dr. Yildiray Cinar and Acting Assistant Professor Kristian Jessen, SUPRI-C, Department of Petroleum Engineering, Stanford University. The full description of the experiments may be found in Cinar et al. [23]. The lab scale experiments are performed using two kinds of glass beads packed and sealed between two plastic blocks. The experiment is performed using four different layouts of the glass beads models as shown in figure 4-20.
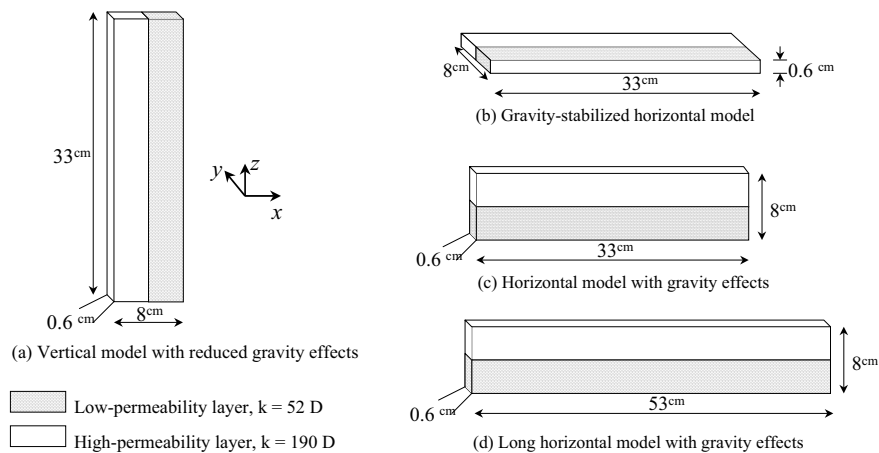

*Figure 4-20. Layouts of the glass beads models.*

The glass beads represented with the white color in Figure 4-20 have the diameter of 0.05cm. The permeability of this layer is 190D. The glass beads

represented with the light gray color have the diameter of 0.025cm. The permeability of this layer is 52D. The porosity of each layer of the glass beads is approximately 39.5%. The dyed water is used to detect the front location using video camcorder. This method allows detecting the areas swept by water; however, it is impossible to determine the exact fluid saturations. The experiments are performed using to sets of fluids with the parameters shown in Table 4-4.

	High interfacial tension		Low interfacial tension	
	iC8-rich "oil"	H_2O-rich	iC8-rich "oil"	H_2O-rich
ρ, g/cm^3	0.692	0.998	0.723	0.795
μ, mPa·s	0.48	1.00	0.836	2.027
IFT, mN/m	38.1		0.024	
$\Delta\rho$, g/cm^3	0.306		0.072	

Table 4-4 Physical properties of the fluids used in the laboratory experiments.

The relative permeability curves and the Leverett function for the low IFT model are presented in Figure 4-21. The relative permeability curves and the Leverett function for the high IFT model are presented in Figure 4-22. These dependencies were obtained from dynamic experiments with the Isooctane (IC8)-water fluid system in the glass beads. Table 4-5 contains the injection rates, the interfacial tensions and the estimations of the displacement regimes for 8 experimental runs.
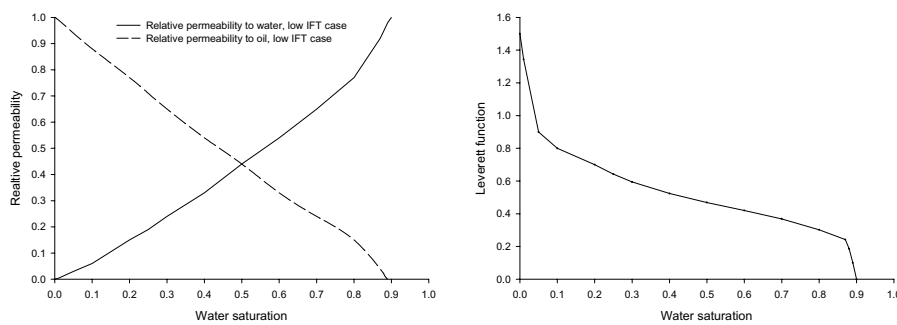
Figure 4-21. The relative permeability curves and the Leverett function for the low IFT model.
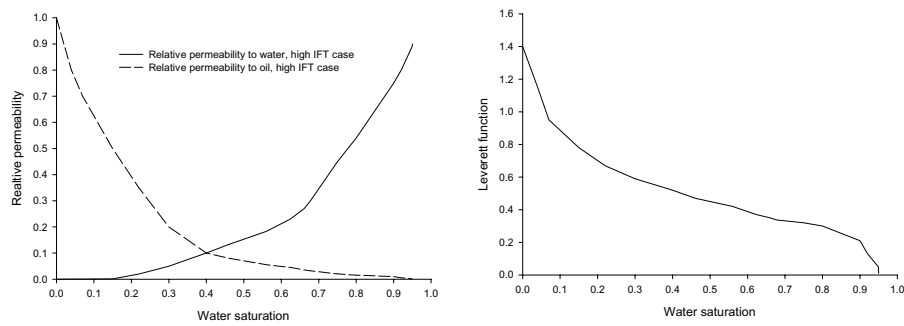
Figure 4-22. The relative permeability curves and the Leverett function for the high IFT model.

Run (layout)	Q, cc/min	IFT mN/m	M	$\dfrac{N_g M}{1+M}$	$\dfrac{N_c M}{1+M}$	R_l^2	flow regime
1 *(4-20a)*	0.6	38.1	0.48	≈ 0.00	170.51	11.48	Capillary-dominated
2 *(4-20a)*	0.6	0.02	0.41	≈ 0.00	0.05	11.48	Viscous-dominated
3 *(4-20c)*	0.6	38.1	0.48	33.95	154.96	13.67	Gravity-Capillary Transition
4 *(4-20c)*	0.6	0.02	0.41	4.52	0.06	11.48	Viscous-Gravity Transition
5 *(4-20a)*	8.5	38.1	0.48	≈ 0.00	11.50	11.48	Capillary-dominated
6 *(4-20a)*	8.5	0.02	0.41	≈ 0.00	0.00	11.48	Viscous-dominated
7 *(4-20c)*	8.5	38.1	0.48	2.39	10.90	13.67	Gravity-Capillary Transition
8 *(4-20c)*	8.5	0.02	0.41	0.29	0.00	11.48	Viscous-Gravity Transition

Table 4-5. The run specific data for experimental runs

The low IFT simulations (runs 2,4,6,8) do not pose any problems for either of the simulators. The saturation profiles are presented in Figures 4-23 to 4-26.
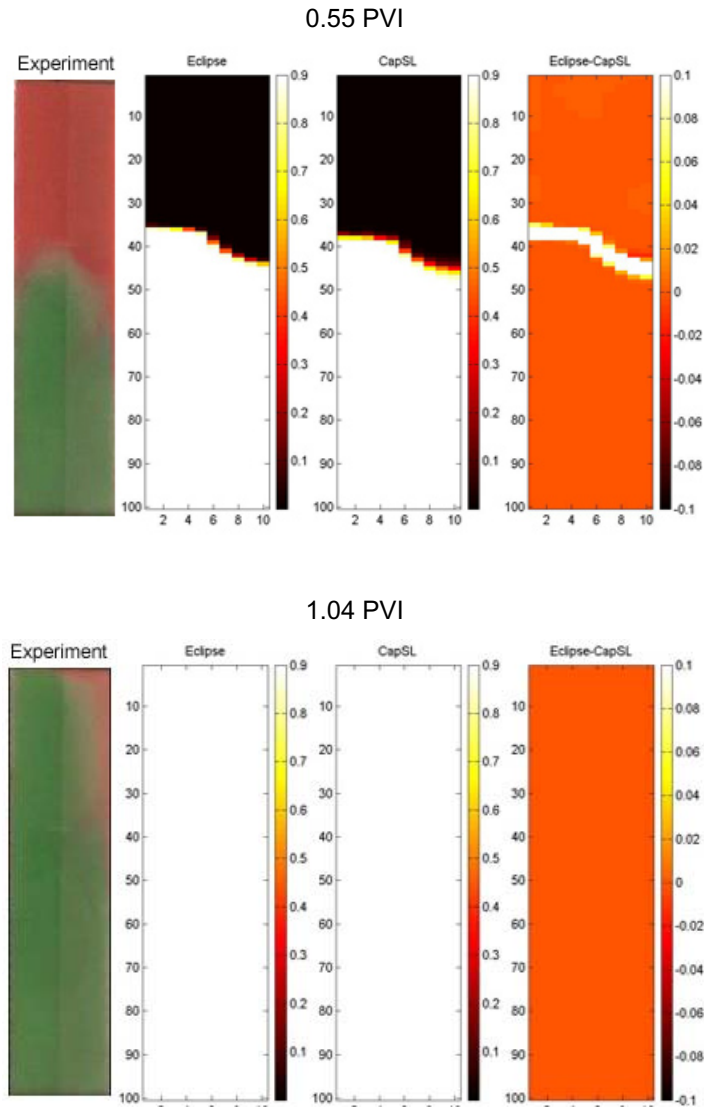

Figure 4- 23. Comparison of the saturation plots for experimental run 2.

0.15 PVI

1.39 PVI

Figure 4-24. Comparison of the saturation plots for experimental run 4.

0.30 PVI

0.60 PVI

Figure 4-25. Comparison of the saturation plots for experimental run 6.

0.40 PVI

0.81 PVI

Figure 4-26. Comparison of the saturation plots for experimental run 8.

Basing on Figures 4-23 to 4-26 it may be concluded that both simulators capture essential features of the displacement profile. The difference between the simulation and the experimental results for the vertical layout of the experimentation setup may be due to the wall effects. The Eclipse saturation front is typically slightly more affected by the numerical dispersion. The oil production curves are presented in Figures 4-27 to 4-30.

Figure 4-27. Oil production curves for experimental run 2.
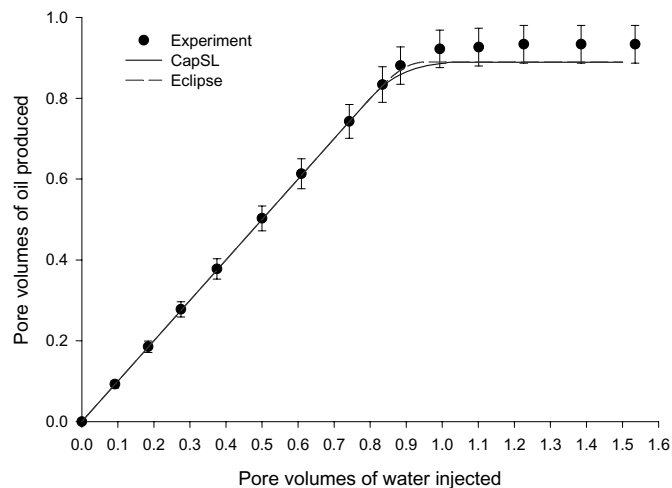
Figure 4-28. Oil production curves for experimental run 4.
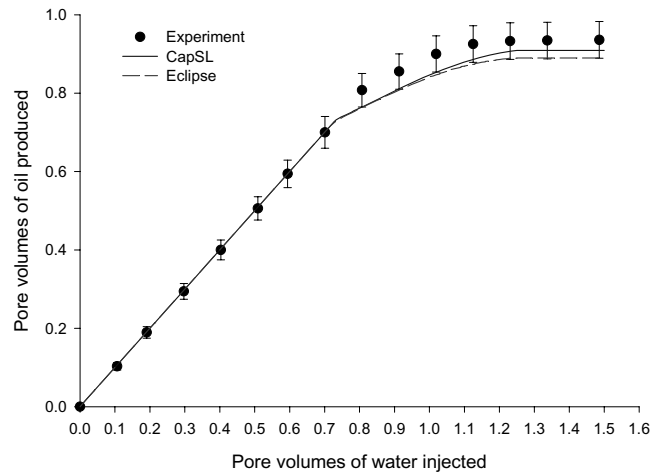
Figure 4-29. Oil production curves for experimental run 6.
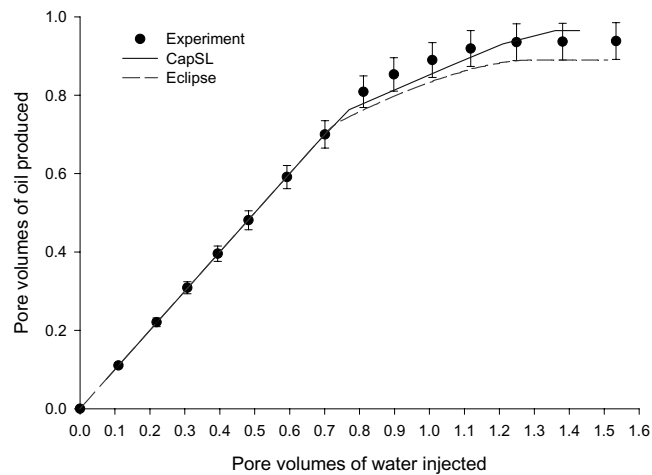
Figure 4-30. Oil production curves for experimental run 8.

It may be concluded that both simulators show excellent match with experimental results. The oil production curves predicted by the CapSL typically lie slightly closer to the experimental points.

The high IFT simulations (runs 1, 3, 5, 7) are more complicated to handle. Moreover, in cases of strong capillary forces small heterogeneities of the glass beads strongly affect the behavior of the saturation front. The saturation profiles are presented in Figures 4-31 to 4-34.
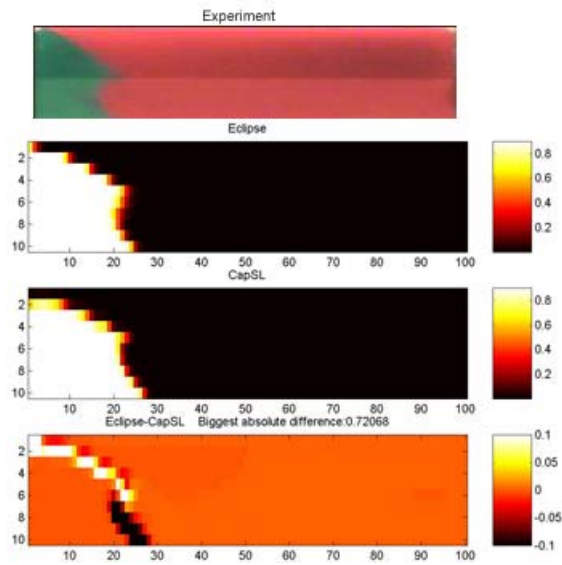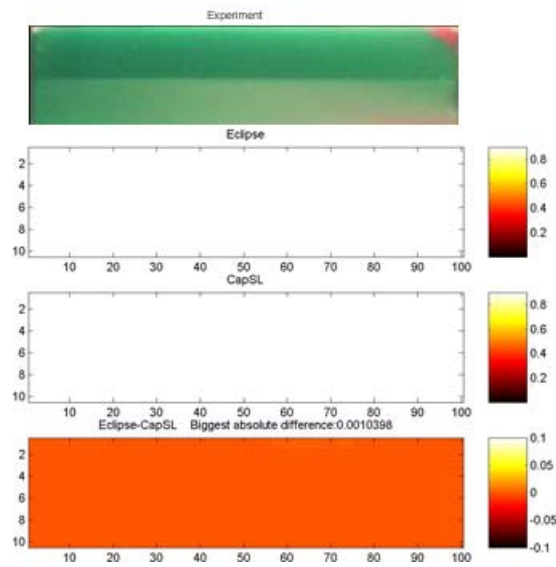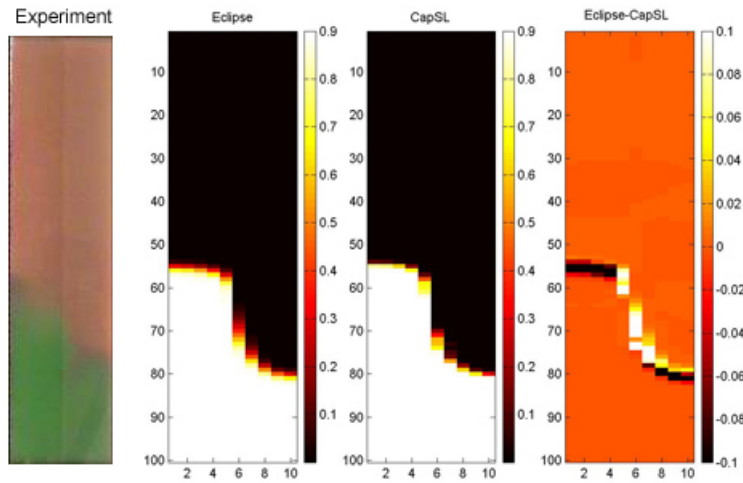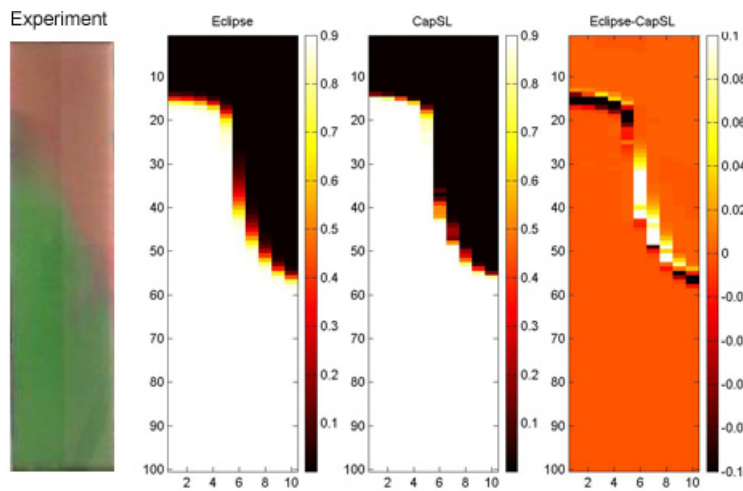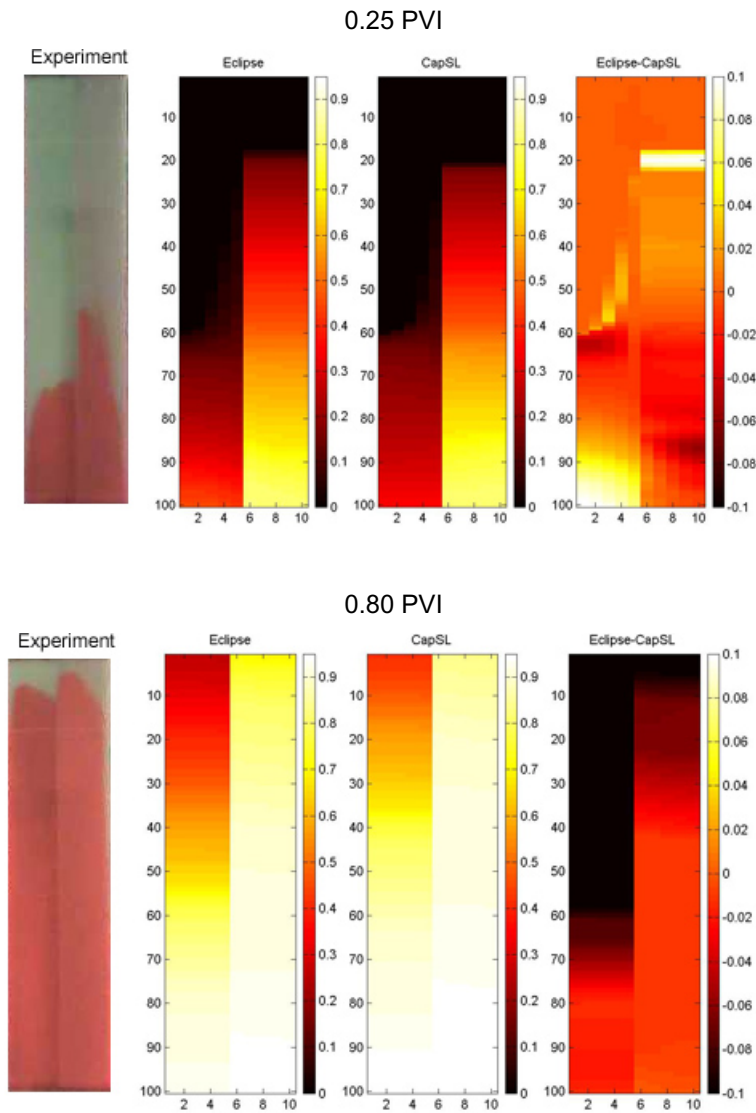

Figure 4-31. Comparison of the saturation plots for experimental run 1.

0.42 PVI

0.80 PVI
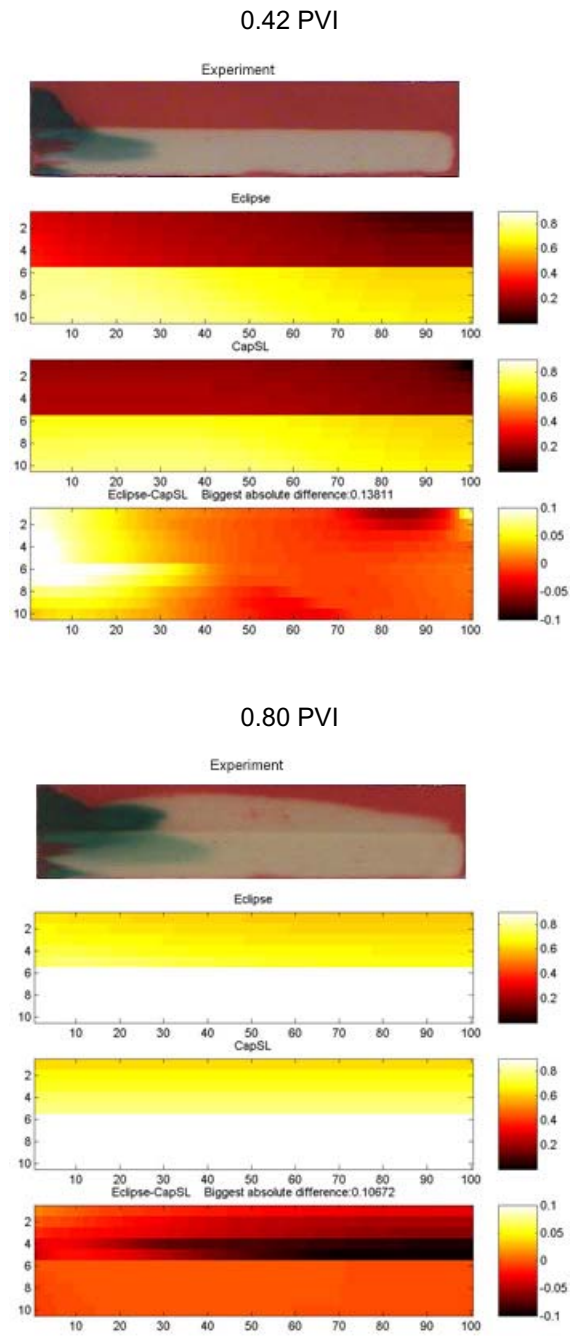
Figure 4-32. Comparison of the saturation plots for experimental run 3.
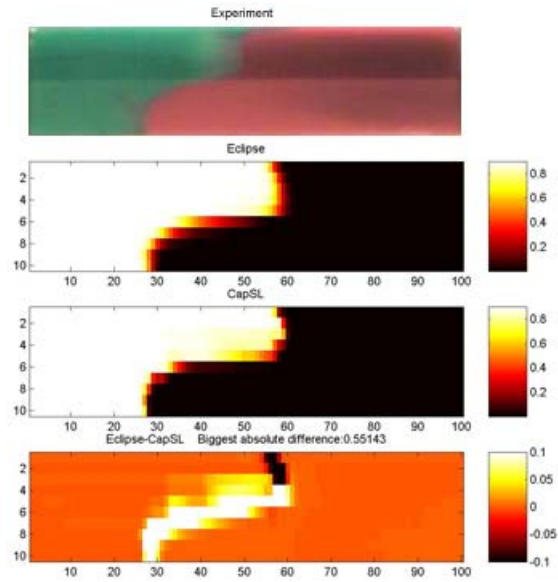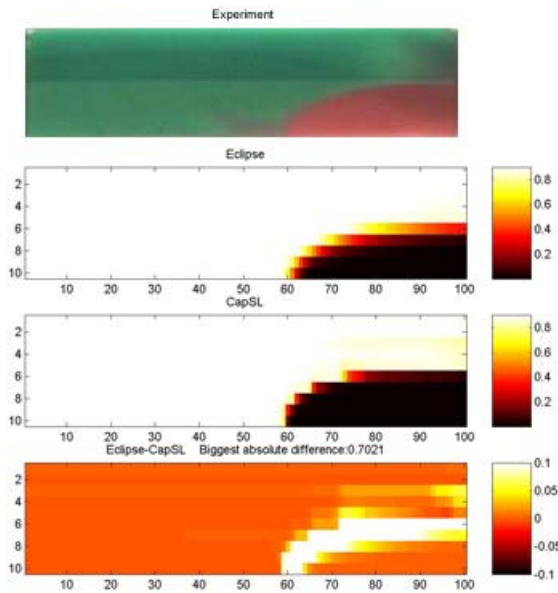
0.28 PVI
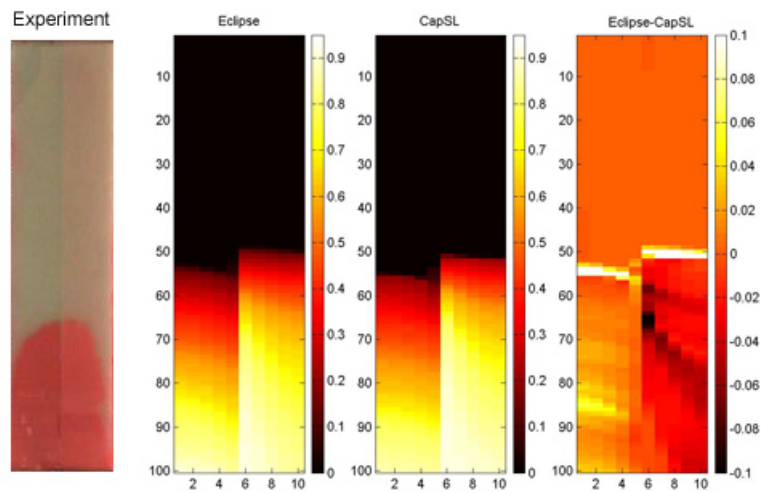
0.75 PVI
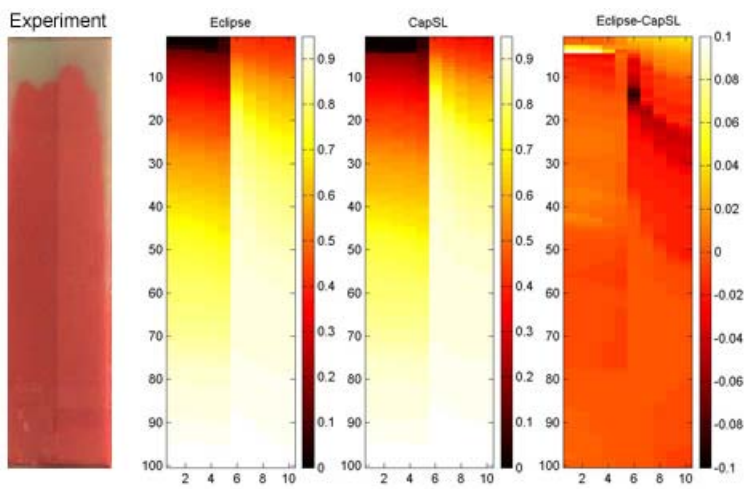
Figure 4-33. Comparison of the saturation plots for experimental run 5.

0.52 PVI

1.05 PVI
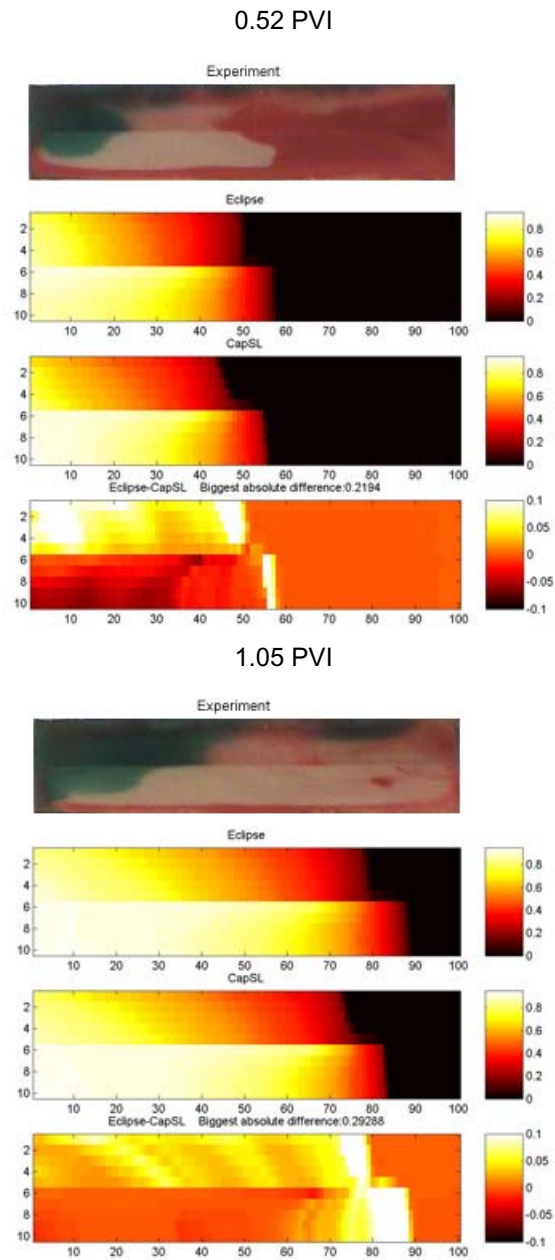
Figure 4-34. Comparison of the saturation plots for experimental run 7.

The oil production curves are presented in Figures 4-35 to 4-38.
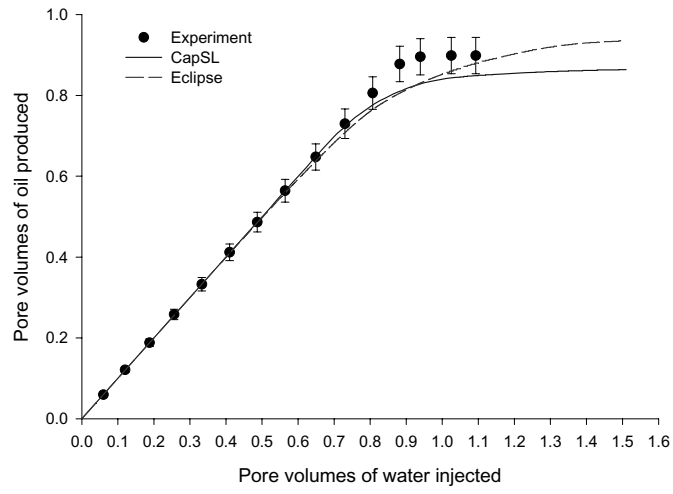
Figure 4-35. Oil production curves for experimental run 1.
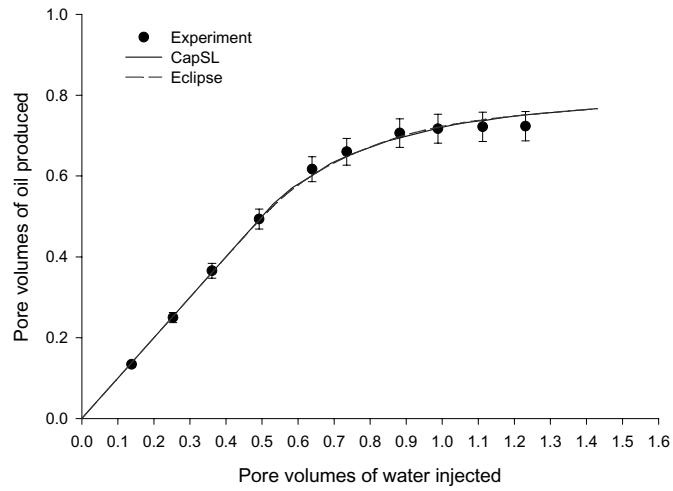
Figure 4-36. Oil production curves for experimental run 3.
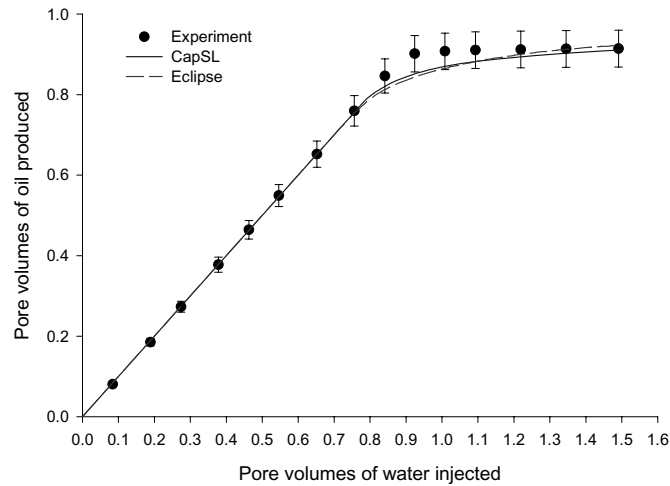
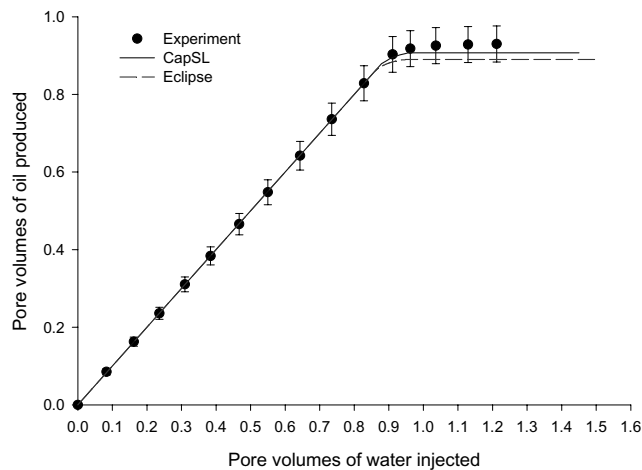*Figure 4-37. Oil production curves for experimental run 5.*
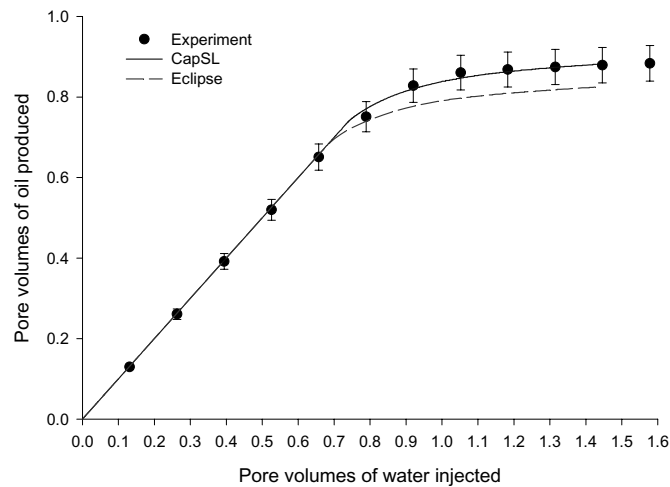
Figure 4-38. Oil production curves for experimental run 7.

For simulations with the low interfacial tension the streamline simulator finishes the simulations with about an order of magnitude less time steps comparing to the Eclipse. Both simulators complete the low IFT runs in less than a minute.

The numbers of time steps taken by the CapSL and the Eclipse to complete the high IFT runs are quite comparable. As a result, the simulation time is about the same as well. The streamline methodology is designed and is advantageous in the cases where the main mass transfer is due to the viscous forces. In the presented high IFT simulations the displacement profile is controlled by the capillary forces. In case of the strongly capillary dominated displacement the CapSL performance is entirely controlled by the stability of the corrector step. Since the corrector step is performed on the finite difference grid, the time step size of the streamline simulator approaches the time step size of the finite-difference method. The streamline simulator may become slower due to the additional, comparing to the finite difference method, streamline tracing procedure. Moreover, the mapping error increases as well, resulting in large mass balance errors of several percent. Run 3 is the most difficult for the streamline simulator and results in the mass balance error of around 7%. Several streamlines actually looped and returned to the injection well. The loop back of the streamlines may happen not only for capillary, but for the gravity simulations as well [18]. Nevertheless, the CapSL and the Eclipse results are in an excellent agreement. Based on the presented simulations, it may be concluded that the streamline simulator in its current realization is applicable to the simulation of the laboratory scale displacements with different displacement regimes. However, in case of high capillary numbers the application of the streamline simulator is not beneficial.

5. Conclusions.

In this work the extension of the streamline method to account for capillary effects is presented. The streamline simulator (CapSL) developed is capable of predicting a displacement performance of the immiscible two phase displacement including heterogeneity effects and the capillary pressure. The main conclusions of this work are:

- The two-phase immiscible incompressible streamline simulator (3DSL0.25 [7]) has been modified to account for capillary effects both in the pressure and the saturation equations. Several methods of introduction of capillary effects are suggested and discussed.

- The CapSL has been tested over a wide range of the simulation cases. Several simple 2D and full-scale 3D simulations are presented. The Eclipse and the CapSL performance is compared based on several laboratory scale displacements as well.

- Both the straightforward method of introduction of capillary effects into the pressure equation (SFD) and the Capillary-Viscous Potential (CVP) method deliver the results which show a good agreement with the Eclipse simulation results. However, the CVP modification method delivers the predictions with lower mass balance error comparing to the SFD method, and is typically faster. The advanced time step selection technique may allow for even larger time steps for the CVP method in a view of higher numerical stability of the method.

- Harmonic averaging of the capillary inter-block transmissibility often leads to underprediction of the capillary cross-flow between the zones with different permeability. The arithmetic averaging of the saturation values for calculation of the capillary inter-block transmissibility results in better prediction of the capillary cross-flow, compared to the Eclipse predictions.

- The CapSL may be applied to the reservoir-scale simulations. The predictions obtained with the CapSL are in a good agreement with the

Eclipse. The CapSL delivers the predictions around 10 times faster compared to the Eclipse. The speed-up factor increases with increase of the simulation grid size.

- For the 3D simulation the CapSL predictions are in accordance with the displacement regime estimated by Bedrikovetsky and Zhou et al. dimensionless groups. The total oil production predicted by the CapSL was not affected by the capillary forces. However, the local displacement profiles for the simulation including and neglecting capillary effects were different. The total oil production predicted by the Eclipse was affected by the capillary forces. The Eclipse simulation without capillary effects resulted in lower oil production due to the higher numerical dispersion.

- The CapSL is less affected by the numerical dispersion in both the small-scale and the reservoir scale simulations. As a result fine features of the displacement front are better captured.

- The effects of alternated wet reservoirs are fully accounted for in the CapSL.

- The zone of application of the streamline simulator has been expanded to the areas of local or global capillary dominated displacements compared to prior art streamline simulation methods.

- Comparison of the CPU time is not entirely fair for neither the CapSL nor the Eclipse. The CapSL is a research code which is not optimised to deliver the ultimate performance. However, the Eclipse 100 is used in the least dispersed, but in a lot of cases, the slowest IMPES formulation. An adaptive implicit solution scheme delivers faster simulation result without loosing too much accuracy.

- For the simulation of those heterogeneous reservoirs with strong capillary domination on the reservoir scale the current streamline methods do no provide serious advantages over the finite difference simulators. Performance of the CapSL is restricted by the performance of the corrector step on the finite difference grid.

- The future research on the streamline methods may include:
  1) Advanced time step selection routines. The currently applied routines are rather simplistic and may result in non-optimal time steps. The

time steps must be chosen in the way to ensure the scheme stability. On the other hand, over-restricting the time step size results in the slower scheme, affected by the numerical dispersion associated with mapping;

2) An application of advanced streamline tracing and mapping routines [48] may facilitate decreasing both simulation time and the numerical error;

3) Handling advanced grids;

4) Advanced well equations;

5) Introduction of capillary effects into two and three phase compositional streamline simulators.

Nomenclature

Symbols

c		Coefficient
C	sm^2kg^{-1}	Capillary inter-block transmissibility for the SFD method
Cn		Courant number
D	m	Depth
E		Error
f		Fractional flow function
F		Function
g	m/c^2	Gravitational constant
H, h	m	Height
J		Leverett function
k	m^2	Permeability
L, l	m	Length
M		Mobility ratio
m, n		Coefficients in the vanGenuchten model
n	m^{-2}	Number of capillaries per unit area (chapter 1)
N	sm^2kg^{-1}	Capillary inter-block transmissibility for the CVP method
		Dimensionless parameter (chapter 3)
P	Pa	Pressure
Q, q	m^3/s	Flow rate
r	m	Radius
R		Shape factor
S		Saturation
t	s	Time
T	sm^2kg^{-1}	Transfer function (chapter 1)
		Inter-block transmissibility (chapter 2)

U	m/s	Velocity
V	m^3	Volume
x, y, z		Axes
		Unknowns (section 1.3.2)

Greek symbols

δ	m	Distance from the block center to the interface
ε		Dimensionless parameters
ϕ		Porosity
Φ	Pa	The porous media dependent term of the capillary pressure
γ		Ratio of the gravity mobility to the total mobility
Υ	Pa	Capillary - viscous potential
λ	Pa·s	Mobility
Λ		Average value
μ	P	Viscosity
θ		Wettability angle
ρ	kg/m^3	Density
σ	N/m	Interfacial tension
τ	s	Time of flight
Ω		Capillary - viscous potential multiplier

Indexes

av		Average
c		Capillary, critical (in formula 1.22)
g		Gravitational, gravity
i,j, k		One of the phases or axes
o		Oil

or	Oil residual
r	Relative
rowi	Relative oil at initial water
rwor	Relative water at oil residual
s	Surface
t	Total
v	Viscous
w	Wetting
wi	Water initial

References

1. Adamson, A.W. Phsyical Chemistry of Surfaces. John Wiles & Sons, New York, USA. 1997.

2. Agarwal, B., and Blunt, M.J. Streamline Based Method With Full-Physics Forward Simulation for History-Matching Performance Data of a North Sea Field. SPE 84952 in SPEJ June, pp. 171-180. 2003.

3. Al-Huthali, A.H., and Datta-Gupta, A. Streamline Simulation of Water Injection in Naturally Fractured Reservoirs. SPE 89443 presented at the 2004 SPE/DOE Symposium on Improved Oil Recovery, Tulsa, USA. 2004.

4. Amyx, J.W., Bass, D.M., and Whiting, R.L. Petroleum Reservoir Engineering. McGraw-Hill, New York, USA. 1960.

5. Aziz, K., and Settari, A. Petroleum reservoir simulation. Elsevier applied science publishers, New York, USA. 1979.

6. Basniev, K.S., Kochina, I.N., and Maksimov, V.M. Underground hydromechanics (Podzemnaja gidromechannica). In Russian. Moscow, Russia. 1993.

7. Barenblatt, G.I., Entov, V.M., Ryzhik, V.M. Theory of fluid flows through natural rocks. Kluwer Academic publisher, Netherlands. 1990.

8. Batycky, R.P. A Three-Dimensional Two-Phase Field Scale Streamline Simulator. Ph.D. Thesis, Department of Petroleum Engineering, School of Earth Science, Stanford University, Stanford, California, USA. 1997.

9. Bedrikovetsky, P.G. Mathematical Theory of Oil and Gas Recovery With Application to ex-USSR Oil and Gas Fields. Kluwer Academic Publishers, Netherlands. 1993.

10. Bedrikovetsky, P.G., Magarshak, T.O., and Shapiro A.A. 3D Analytical Model for Displacement of Oil Using Horizontal Wells. SPE 26996

presented at III Latin American / Caribbean Confernce held in Buenos Areas, Argentina. 1994.

11. Bedrikovetsky, P.G. New Mathematical Model for EOR Displacements Honoring Oil Ganglia. SPE 38892 presented at the SPE Annual Technical Conference and Exhibition, San Antonio, Texas, USA. 1997.

12. Bedrikovetsky, P.G. WAG Displacemetns of Oil-Condensates Accounting for Hydrocarbon Ganglia. Transport in Porous Media, Vol.52, pp. 229-266. 2003.

13. Bedrikovetsky, P.G. Analytical Model for the Waterflood Honoring Capillary Pressure. SPE 36130, presented at the Fourth Latin and Caribbean Petroleum Engineering Conference held in Port-of-Spain, Trinidad and Tobago. 1996.

14. Berenblyum, R.A., Shapiro, A.A., Jessen, K., Stenby, E.H., and Orr, F.M. Jr. Black Oil Streamline Simulator With Capillary Effects. SPE 84037, presented at the SPE Annual Technical Conference and Exhibition held in Denver, Colorado, USA. 2003.

15. Berenblyum, R.A., Shapiro, A.A., Stenby E.H. A Method For Simulating A Multiphase Flow. Patent Application PA 2003 01844, Denmark. 2003.

16. Berre, I., Dahle, H.K., Karlsen, K.H., and Nordhaug, H.F. A Streamline Front Tracking Method for Two- and Three-Phase Flow Including Capillary Forces. Mathematics Subject Classification, pp 1-13. 2000.

17. Blair, P.M., and Weinlaug, C.F. Solution of Two-Phase Flow Problems Using Implicit Difference Equations. SPE 2185, Presented at 43rd Annual Fall Meeting, Houston, USA. 1969.

18. Blunt, M.J., Lui, K., Thiele, M.R. A Generalized Streamline Method to Predict Reservoir Flow. Petroleum Geoscience, vol. 2, pp. 259-269. 1996.

19. Blunt, M.J. Flow in porous media – pore-network models and multiphase flow. Current Opinion in Colloid & Interface Science, vol. 6, pp 197-207. 2001.

20. Bratvedt, F., Bratvedt, K., Buchholz, C.F., Gimse, T., Holden, H., Holden, L., and Risebro, N.H. Frontline and Frontsim: two full scale, two-phase, black oil reservoir simulators based on front tracking. Surveys on Mathematics for Industry, vol. 3, pp. 63-78. 1993.

21. Bratvedt, F., Gimse, T., and Tegnander, C. Streamline Computations for Porous Media Flow Including Gravity. Transport in Porous Media, vol. 25, pp. 63-78. 1996.

22. Buckley, S.E., and Leverett, M.C. Mechanisms of Fluid Displacement in Sands. Petroleum Technology, May, pp107-116. 1941.

23. Cinar, Y., Jessen, K., Juanes, Berenblyum, R., and Orr, F.M. An experimental and Numerical Investigation of Crossflow Effects in Two-Phase Displacements. SPE 90568, to be presented at the SPE Annual Technical Conference and Exhibition, Houston, USA. 2004.

24. Christie, M.A., and Blunt, M.J. Tenth SPE Solution Project: A comparison of Upscaling Techniques. SPE72469 in SPE Reservoir Evaluation and Engineering, August, pp. 308-317. 2001.

25. Coats, K.H. Implicit Compositional Simulation of Single-Porosity and Dual-Porosity Reservoirs. SPE 18427, presented at SPE Symposium On Reservoir Simulation, Huston, USA. 1989.

26. Coats, K.H. A Note on IMPES and Some IMPES-Based Simulation Models. SPE 65092 in SPE Journal, vol. 5, pp. 245-251. 2000.

27. Coats, K.H. IMPES Stability: The CFL Limit. SPE 66345, presented at SPE Reservoir Simulation Symposium, Houston, USA. 2001

28. Coats, K.H. IMPES Stability: The Stable Step. SPE 69225, presented at SPE Reservoir Simulation Symposium, Huston, USA. 2001.

29. Coats, K.H. IMPES Stability: Selection of Stable Timesteps. SPE 84924 in SPEJ, June, pp. 187-187. 2003.

30. Crane, M., Bratvedt, F., Bratvedt, K., Childs, P., and Olufsen, R. A Fully Compositional Streamline Simulator. SPE 63156 presented at SPE Annual Technical Conference and Exhibition, Dallas, Texas, USA. 2000.

31. Darcy, H. The public fountains in the Town of Dijon, V. Dalmont, Paris, France. 1856

32. Datta-Gupta, A., and King, M.J. A Semianalytic Approach to Tracer Flow Modeling in Heterogeneous Permeable Media. Advances in Water Resources, vol. 18, pp. 9-24. 1995.

33. Di Donato, G., Huang, W., and Blunt, M. Streamline-Based Dual Porosity Simulation of Fractured Reservoirs. SPE 84036 presented at SPE Annual Technical Conference and Exhibition, Denver, Colorado, USA. 2003.

34. Dullien, F.A.L. Porous media. Fluid Transport and Pore Structure. Academic Press, New York, USA. 1979.

35. Emanuel, S., and Milliken, W.J. History Matching Finite Difference Models With 3D Streamlines. SPE 49000 presented at SPE Annual Technical Conference and Exhibition, New Orleans, Louisiana, USA. 1998.

36. Farkas, E. Adaptice Implicit Volume Balance Techniques. SPE 25273 presented at 12th SPE Symposium on Reservoir Evaluation, New Orleans, Louisiana, USA. 1993.

37. Higgins, R.V., and Leighton, A.J. Performance of Five-spot Water Floods in Stratified Reservoirs Using Streamlines, SPE 57 in Trans. AIME, pp.1-12. 1961.

38. Higgins, R.V., and Leighton, A.J. A Computer Method to Calculate Two-Phase Flow in Amy Irregular Bounded Porous Medium. SPE 243, presented at SPE Annual California Regional Meeting, USA. 1962.

39. Higgins, R.V., and Leighton, A.J. Computer Prediction of Water Drive of Oil and Gas Mixture Through Irregularly Bounded Porous Media – Three-Phase Flow. SPE 283, presented at SPE production reservoir Symposium, Tulsa, Oklahoma, USA1962.

40. Ichiro, O., Datta-Gupta, A., and King, M.J. Time step selection during streamline simulation via transverse flux correction. SPE 79688,

presented at 2003 SPE reservoir simulation symposium, Huston, USA. 2003.

41. Jessen, K., Wang, Y., Ermakov, P., Zhu, J., and Orr, F.M. Fast, Approxmate Soilutions for 1D Mulitcomponent Gas-Injection Problems. SPE 74700 in SPEJ, December, pp. 442-451. 2001.

42. Jessen, K., and Orr, F.M. Compositional Streamline Simulation. SPE 77379 presented at SPE Annual Technical Conference and Exhibition, San Antonio, Texas, USA. 2002.

43. Jessen, K., and Orr, F.M. Gas Cycling and the Development of Miscibilty in Condensate Reservoirs. SPE 84070 presented at SPE Annual Technical Conference and Exhibition, Denver, Colorado, USA. 2003.

44. Jessen, K., and Orr, F.M. Gravity segregation and Compositional Streamline Simulation. SPE 89448, presented at SPE/DOE symposium on Improved Oil Recovery, Tulsa, Oklahoma, USA. 2004.

45. Killough, J.E. and Kossack, C.A. Fifth Comparative Solution project: Evaluation of Miscible Flood Simulators. SPE 16000 presented at Ninth SPE Symposium on Reservoir Simulation, San Antonio, Texas, USA. 1987.

46. King, M.J., and Datta-Gupta, A. Streamline Simulation: A current perspective. In Situ, vol. 22(1), pp. 91-140. 1998.

47. Leverett, M.C. Capillary behavior in Porous Solids. Trans. AIME. 1941.

48. Mallison, B.T., Gerritsen, M.G, and Matringe S.F. Improved Mappings for Streamline-Based Simulation. SPE 89352 presented at the 2004 SPE/DOE Symposium on Improved Oil Recovery, Tulsa, Oklahoma, USA. 2004.

49. Marcell-De Silva, J., and Dawe, R.A. Effects of Permeability and Wettability Heterogeneities on Flow in Porous Media. SPE 81164 presented at SPE Latin American and Caribbean Petroleum Engineering Conference, Port-of-Spain, Trinidad, West Indies. 2003.

50. Martin, J.C., and Wegner, R.E. Numerical Solution of Multiphase, Two-Dimensional Incompressible Flow Using Stream-Tube Relationships. SPE 7140 in Trans. AIME, October, pp. 313-323. 1979

51. Matanga, G.B. Stream Functions in Three-Dimensional Groundwater Flow. Water resources Research, vol. 29(9), pp 3125-3133. 1993.

52. Mattax, C.C., and Dalton, R.L. Reservoir Simulation. SPE Monogram Series. SPE, Richardson, Texas, USA. 1990.

53. Milliken, W.J., Emanuel, A.S., and Chakravarty, A. Application of 3D Streamline Simulation To Assist History Matching. SPE 74712, presented at SPEREE December, pp. 502-508. 2001.

54. Muskat, M. Flow of Homogeneous Fluids. McGraw-Hill, Boston, USA. 1937.

55. Peaceman, D.W. Fundamentals of numerical reservoir simulation. Elsevier, New York, USA. 1977

56. Peaceman, D.W. Interpretation of Well-Block Properties in Numerical Reservoir Simulation with Nonsquare Grid Blocks and Anisotropic Permeability. SPE 10528 in SPEJ, June, pp. 531-569. 1983

57. Pollock, D.W. Semianalytical Computation of Path Lines for Finite-Difference Models. Ground Water, vol.26(6), pp. 743-750. 1988.

58. Rapoport, L.A., and Leas, W.J. Properties of Linear Waterfloods. Petroleum Transactions AIME, vol.198, pp. 139-148. 1953.

59. Renard, G. A 2D Reservoir Streamtube EOR Model With Periodical Automatic Regeneration of Streamlines. In Situ, vol. 14(2), pp. 175-200. 1990.

60. Rodriguez, P.G., Segura, M.K., and Moreno, F.J.M. Streamline methodology using an efficient operator splitting for accurate modeling of capillary and gravity effects. SPE 79693, presented at SPE Reservoir Simulation Symposium, Houston, USA. 2003.

61. Russell, T.F. Stability Analysis and Switching Criteria for Adaptive Implicit Methods Based on the CFL condition. SPE 18416 presented at SPE Symposium on Reservoir Simulation, Houston, Texas, USA. 1989.

62. Schlumberger GeoQuest. Eclipse 100 Technical Description. 2003.

63. Schlumberger GeoQuest. Eclipse 300 Reference Manual. 2003.

64. Schlumberger GeoQuest. FrontSim Technical Description. 2003.

65. Seto, C.J., Jessen, K., and Orr, F.M. Compositional Streamline Simulation of Field Scale Condensate Vaporization by Gas Injection. SPE 79690 presented at SPE Reservoir Simulation Symposium, Houston, Texas, USA. 2003.

66. Shapiro, A.A, and Stenby, E.H. Factorization of Transport Coefficients in Macroporous Media. Transport in Porous Media, vol. 41, pp. 305-323. 2000.

67. Spivak, A., and Coats, K.H. Numerical Simulation of Coning Using Implicit Production Terms. SPE 2595 in SPEJ, September, pp. 257-267. 1970.

68. Thiele, M.R. Modeling Multiphase Flow in Heterogeneous Media Using Streamtubes. PhD dissertation, Stanford University, Dept. of Petroleum Engineering, Stanford, California, USA. 1994.

69. Thiele, M.R., Batycky, R.P., Blunt, M.J., and Orr, F.M. Jr. Simulating Flow in Heterogeneous Media Using Streamtubes and Streamlines. SPE 27834 in SPE Reservoir Engineering, vol. 10(1), pp. 5-12. 1996.

70. Thiele, M. R., Batycky, R.P., and Blunt, M.J. A Streamline-Based 3D Field-Scale Compositional Reservoir Simulator. SPE 38889 presented at SPE Annual Technical Conference and Exhibition, San Antonio, Texas, USA. 1997.

71. Thiele, M.R. Streamline Simulation. 6th international forum on Reservoir Simulation, Austria. 2001.

72. Thiele, M.R., and Batycky, R.P. Water Injection Optimization Using a Streamline-Based Workflow. SPE 84080 presented at SPE Annual Technical Conference and Exhibition, Denver, Colorado, USA. 2003.

73. Thomas, G.W., and Thurnau, D.H. Reservoir Simulation Using an Adaptive Implicit Method. SPE 10120 presented at the 56th Annual Fall Technical Conference and Exhibition of the SPE of AIME, San Antonio, Texas, USA. 1981.

74. Thomas, G.W., and Thurnau, D.H. The Mathematical Basis of the Adaptive Implicit Method. SPE 10495 presented at the 6th SPE Symposium in Reservoir Simulation, New Orleans, Louisiana, USA. 1982.

75. Toth, J. Adsorption: Theory, Modeling, and Analysis. Marcel Dekker, New York, USA. 2002.

76. Trangenstein, J.A. Numerical Analysis of Reservoir Fluid Flow, Multiphase Flow in Porous Media: Mechanics, Mathematics and Numerics, Lecture notes in Engineering. Springer Verlag (34).

77. van Genuchten, M.Th. A closed-form Equation for Prediciting the Hydraulic Conductivity of Unsaturated Soils. Soil Sci. Soc. Am. J., vol. 44, p. 892. 1980.

78. Yan, W., Michelsen, M.L., Stenby, E.H., Berenblyum, R.A., and Shapiro, A.A. Three-phase Compositional Streamline Simulation and Its Application to WAG. SPE 89440 presented at the 2004 SPE/DOE Symposium on Improved Oil Recovery, Tulsa, USA. 2004.

79. Young, L.C., and Russell, T.F. Implementation of an Adaptive Implicit Method. SPE 25245 presented at 12th SPE Symposium on Reservoir Simulation, New Orleans, Louisiana, USA. 1993.

80. Zhou, D., Fyaers, F.J., and Orr, F.M. Scaling multiphase flow in simple heterogeneous porous media. Multiphase Transport in Porous Media, vol. 265, pp. 25-35. 1993.

Roman A. Berenblyum

**Streamline Simulation with Capillary Effects
Applied to Petroleum Engineering Problems**